SEARCH FOR THE TOP QUARK IN EVENTS WITH A LEPTON AND TWO OR MORE JETS AT THE FERMILAB COLLIDER DETECTOR

A Dissertation

Presented to

The Faculty of the Graduate School of Arts and Sciences

Brandeis University

Department of Physics

In Partial Fulfillment
of the Requirements for the Degree of
Doctor of Philosophy

by
Luc Demortier
September, 1991

This dissertation, directed and approved by the candidate's Committee, has been accepted and approved by the Graduate Faculty of Brandeis University in partial fulfillment of the requirements for the Degree of

DOCTOR OF PHILOSOPHY

Dean, Graduate School of
Arts and Sciences

Dissertation Committee:

James Bensinger, Chairman

Eric Jensen

Hugh Pendleton, III

George Brandenburg (Harvard Univ)

ABSTRACT

SEARCH FOR THE TOP QUARK IN EVENTS WITH A LEPTON AND TWO OR MORE JETS AT THE FERMILAB COLLIDER DETECTOR

(A Dissertation Presented to the Faculty of the Graduate School of Arts and Sciences of Brandeis University, Waltham, Massachussetts)

by Luc Demortier

A search for the top quark in $p\bar{p}$ collisions at a center of mass energy of 1.8 TeV is described. The analysis is based on data collected with the Collider Detector at Fermilab during the 1988–1989 run. Events are selected by requiring an energetic electron or muon, missing transverse energy, and two or more jets. By studying the transverse mass distribution of the lepton and missing energy, the Standard Model production and decay of $t\bar{t}$ pairs is excluded at 95% confidence level if the top quark mass is between 60 and 73 GeV/c^2. The observed lepton + multijet sample is consistent with W boson production.

Acknowledgements

My greatest thanks go to my advisor, Jim Bensinger, for giving me the opportunity to collaborate with CDF, for his continuous encouragement during my graduate student career, for sharing his insights, and for an apparently inexhaustible supply of good will. I am also grateful for his careful reading of the text, and his judicious criticisms. G.P. Yeh suggested the topic of this thesis, provided guidance at crucial points in the analysis, and commented on several sections of the text. His friendliness and constant availability inspired the confidence needed to bring this work to fruition. Milciades Contreras offered an enthusiastic willingness to help think through several subtle points in the interpretation of the data. Conversations with Paul Derwent, Marshall Miller, Aseet Mukherjee, Satoru Ogawa, Yoshihiro Seiya, Pekka Sinervo, David Smith, Fumihiko Ukegawa, and Tom Westhusing proved very beneficial. This thesis would obviously not have been possible without the foundational work of the many people who invented and tested the algorithms needed to reconstruct raw data, understand backgrounds, and identify signals. And beyond them are those who built the detector, and those who built and operated the accelerator, ... It would be quite impossible to try and acknowledge in its entirety the formidable impetus of which this here is but a tiny offshoot, for the debt is evidently too great.

This thesis is dedicated to my first physics teacher, Mrs. Maria-Magdalena Baudry-Beaulieu.

Table of Contents

List of Tables

List of Figures

Chapter 1
Introduction

"Now in my view there are only two things to learn about the top quark and that is the date when it will be discovered and its mass". M. Veltman (1989)

Today we believe in the existence of the top quark for essentially the same reasons that, twenty years ago, it was argued that there must be a charmed quark. Since then, the Standard Model has developed into a theory capable of explaining and predicting the outcome of a remarkable variety of experiments. Hence the current arguments for top seem all the more compelling; they will be reviewed later in this chapter. Unfortunately we have no short answer to a theorist's somewhat blasé comment in the above excerpt. The top quark has not been discovered yet, but information about its mass is already available from several measurements. This thesis describes one such measurement, performed on data taken by the CDF collaboration during the 1988–1989 Tevatron run.

The remainder of Chapter 1 is devoted to an overview of the properties the top quark is anticipated to have. Section 1.5 describes the specific $t\bar{t}$ signature we will attempt to identify. Chapter 2 briefly reviews the CDF detector, with special emphasis on the components relevant to the analysis. The calculation of the integrated luminosity of the CDF data samples is explained in Chapter 3. The fourth chapter presents the criteria used to select leptons and the algorithms to reconstruct jets. In Chapter 5 we discuss the Monte Carlo event samples that were generated to understand the top production process, its topology in the CDF detector, and the competing background processes. The signal region is defined

and studied in Chapter 6, where multijet and $b\bar{b}$ backgrounds are also estimated. For each of the three top masses m_{top} = 60, 70, and 80 GeV/c^2, we obtain an upper limit on the $t\bar{t}$ production cross section in Chapter 7. By comparing these upper limits with the lower limit on a theoretical prediction, we subsequently derive a 95% C.L. lower limit on the mass of the top quark. Our conclusions are contained in Chapter 8.

1.1 Evidence for the existence of the top quark

The most compelling indication of the existence of the top quark comes from measuring the weak isospin eigenvalue T^b_{3L} of the bottom quark. If the SU(2) structure of the Standard Model is valid, and the bottom quark has $T^b_{3L} = -1/2$, then this quark must belong to an SU(2) multiplet of states, one of which has $T_{3L} = +1/2$ and is by definition the top quark. Experimentally one measures combinations of T^b_{3L} and T^b_{3R}, the weak isospin eigenvalues for the left-handed and right-handed bottom quarks. At e^+e^- colliders, the process $e^+e^- \rightarrow b\bar{b}$ exhibits a forward-backward asymmetry, A_{FB}, of the form

$$A_{FB} \propto [T^b_{3L} - T^b_{3R}]\,[T^b_{3L} + T^b_{3R} + \frac{2}{3}\sin^2\theta_W] \tag{1.1}$$

where θ_W is the electroweak mixing angle. Assuming that

$$T^b_{3R} = 0 \tag{1.2}$$

one can use (1.1) to determine T^b_{3L}. This has been done by several collaborations at e^+e^- experiments. A combined fit to all their measurements yields [Mar89a]:

$$T^b_{3L} = -0.54 \pm 0.13 \tag{1.3}$$

The assumption made in (1.2) can be omitted if one measures the decay rate for $Z^0 \rightarrow b\bar{b}$:

$$\Gamma(Z^0 \rightarrow b\bar{b}) \approx 3\,\frac{G_F M_Z^3}{3\sqrt{2}\pi}\left\{\left(T^b_{3L} + \frac{1}{3}\sin^2\theta_W\right)^2 + \left(T^b_{3R} + \frac{1}{3}\sin^2\theta_W\right)^2\right\} \tag{1.4}$$

where G_F is the Fermi constant and M_Z the mass of the Z^0 boson. Equation (1.4) is valid in the approximation of a massless b quark. Together, (1.1) and

(1.4) would allow a simultaneous determination of T^b_{3L} and T^b_{3R} [Kan90]. To our knowledge, this has never been attempted.

Another way of verifying that the left-handed b quark is not an SU(2) singlet consists in comparing possible flavour-changing neutral current decays of B mesons with the corresponding charged current decays. If the b quark is a weak SU(2) singlet decaying via emission of W and Z bosons, then theory predicts that [Kan82]:

$$\mathrm{Br}(B \to l^+l^-X) > 0.013 \tag{1.5}$$

where l^+ and l^- are leptons from the direct decay of the B. The lower limit (1.5) is independent of the number of additional weak-singlet quarks heavier than the b. It is also insensitive to variations in the weak mixing angles within present experimental constraints. The CLEO collaboration has obtained the following result [Bea87]:

$$\mathrm{Br}(B \to l^+l^-X) = \frac{\mathrm{Br}(B \to \mu^+\mu^-X) + \mathrm{Br}(B \to e^+e^-X)}{2} < 0.0012 \tag{1.6}$$

at the 90% confidence level, thus strongly constraining topless quark models.

The incompleteness of an $\mathrm{SU(2)_L} \times \mathrm{U(1)}$ model in which the b_L quark is an $\mathrm{SU(2)_L}$ singlet can also be demonstrated by studying oscillations between the B^0_d and $\overline{B}^0_d$ mesons. Such oscillations are typically described in terms of the parameter $x_d \stackrel{\mathrm{def}}{=} \Delta m/\Gamma$, where Δm is the $B^0_d - \overline{B}^0_d$ mass difference and Γ the mean decay width. Measurements made by the ARGUS collaboration yield $x_d = 0.73 \pm 0.18$ [Alb87]. In the absence of a top quark, flavour-changing neutral currents would increase this value of x_d by at least an order of magnitude [Roy90].

From a purely theoretical standpoint, the main advantage of the existence of the top quark is the cancellation of the so-called triangle anomalies. Such anomalies occur because the gauge bosons couple differently to left-handed and right-handed fermions. It is not yet clear however, whether these anomalies would have any measurable experimental impact. Neither is it established that the top quark is the only way of eliminating anomalies [Kan90].

1.2 Constraints on $\mathrm{m_{top}}$

Searches for direct production of $t\bar{t}$ pairs at e^+e^- colliders have excluded several mass ranges for the top. At TRISTAN, the TOPAZ collaboration looked for multi-hadron events with an isolated muon originating from a virtual W decay in the process chain

$$e^+e^- \to t\bar{t}X, \quad t\bar{t} \to bW^+\bar{b}W^- \tag{1.7}$$

Their analysis resulted in the limit: $\mathrm{m_{top}} > 29.9\ \mathrm{GeV/c^2}$, at 95% C.L. [Ada89]. Similar studies were performed at the LEP collider. For process (1.7), ALEPH reported the result: $\mathrm{m_{top}} \notin [26.0, 45.8]\ \mathrm{GeV/c^2}$, at 95% C.L., from a search for spherical events containing an isolated charged particle [Dec90]. The OPAL collaboration made no isolated particle requirement and based their analysis on the acoplanarity event shape parameter. They tested the sensitivity of their method to a non-Minimal Standard Model decay of the top:

$$t \to bH^+ \tag{1.8}$$

where H^+ is a charged Higgs boson. Assuming that the top decays with a 100% branching fraction into the charged Higgs channel, and that subsequently the Higgs always decays into hadrons, OPAL excludes with 95% confidence the top mass from the interval $[m_{H^+} + 5.2,\ 45.2]\ \mathrm{GeV/c^2}$, where $m_{H^+} = 23$, 28, 33 or 38 $\mathrm{GeV/c^2}$ [Akr90]. A more complex search strategy was devised by DELPHI to avoid restrictions on the charged Higgs decay mode. They determine, also with 95% confidence, that $\mathrm{m_{top}} \notin [33, 44]\ \mathrm{GeV/c^2}$ if the charged Higgs boson is heavier than 30 $\mathrm{GeV/c^2}$ but at least 6 $\mathrm{GeV/c^2}$ lighter than the top [Abr90]. A measurement by ALEPH of the total hadronic cross section at the Z^0 peak provides a limit which is independent of the top decay mode [Dec90]:

$$\mathrm{m_{top}} > 45.8\ \mathrm{GeV/c^2} \tag{1.9}$$

with 95% confidence.

At $p\bar{p}$ colliders, top quarks can be produced through the strong interaction process:

$$p\bar{p} \to t\bar{t}X \tag{1.10}$$

and, if kinematically allowed, through the weak decay of W bosons:

$$p\bar{p} \rightarrow WX \rightarrow tbX \tag{1.11}$$

Process (1.11) dominates over (1.10) for top masses between 35 and 70 GeV/c^2 at the center of mass energy $\sqrt{S}$ = 630 GeV of the CERN SPS [Ake90]. At the Fermilab Tevatron however ($\sqrt{S}$ = 1800 GeV), process (1.10) dominates for all top masses. The UA2 collaboration has performed an analysis of events containing a high energy electron and neutrino. Assuming charged current decay of the top, they exclude the top mass range 30–69 GeV/c^2 at the 95% C.L. [Ake90]. CDF has already obtained several limits within the framework of the minimal Standard Model (no charged Higgs). In process (1.10), both top quarks can decay semileptonically. By searching for events containing a high P_T electron and a muon, CDF has excluded top masses between 28 and 72 GeV/c^2 [Abe90a]. After enlarging this search to several other dilepton decay channels, the upper limit of the excluded range has been pushed up to 89 GeV/c^2 (95% C.L.) [Abe90b]. CDF has also measured the cross section for production of a W boson followed by decay into the electron channel, divided by the corresponding quantity for a Z boson:

$$R \stackrel{\text{def}}{=} \frac{\sigma(W \rightarrow e\nu)}{\sigma(Z^0 \rightarrow e^+e^-)} = 10.2 \pm 0.8(\text{stat}) \pm 0.4(\text{sys}) \tag{1.12}$$

This ratio can be rewritten as:

$$R = \frac{\sigma(p\bar{p} \rightarrow WX)}{\sigma(p\bar{p} \rightarrow Z^0X)} \frac{\Gamma(W \rightarrow e\nu)}{\Gamma(Z^0 \rightarrow e^+e^-)} \frac{\Gamma(Z^0)}{\Gamma(W)} \tag{1.13}$$

Using LEP data for the Z^0 width and a theoretical prediction for the ratio of production cross sections, CDF obtains [Abe91c]

$$\frac{\Gamma(W)}{\Gamma(W \rightarrow e\nu)} = 9.47 \pm 0.86 \tag{1.14}$$

from which a 95% C.L. lower limit can be set on the top mass:

$$\mathrm{m_{top}} > 43 \text{ GeV/c}^2 \tag{1.15}$$

This limit is independent of the decay modes of the top. Sufficient statistics from future runs should improve this important $p\bar{p}$ measurement, and supersede the corresponding e^+e^- result (1.9).

The mass of the top quark enters into radiative corrections to the W and Z boson masses (figure 1.1,a), the Z decay width (figure 1.1,b), and several weak neutral current observables. The requirement of consistency between measurements of these quantities and theoretical calculations places an upper limit on the top mass [Ken91,Lan91]. Within the Minimal Standard Model, one has:

$$\mathrm{m_{top}} < 182 \text{ GeV/c}^2 \tag{1.16}$$

with 95% confidence and if the mass of the neutral Higgs boson does not exceed 1 TeV/c^2. If the Standard Model is extended to include additional particles which couple to the W and Z bosons (such as higher-dimensional representations of the Higgs field), the above limit may no longer be valid. This is an important restriction, as there are many reasons to believe that the minimal version of the Standard Model is incomplete. However, with sufficiently accurate measurements of $\mathrm{M_W}$, $\mathrm{M_Z}$, and $\Gamma(Z^0 \rightarrow b\bar{b})$, it is possible to disentangle the effect of the top mass on these observables, from the effect of Standard Model extensions. Present data allow to set a 95% C.L. upper limit of 310 GeV/c^2 on the top mass, independently of the theoretical assumptions concerning the Higgs sector.

1.3 Theoretical calculation of top quark production

In the previous section, we mentioned that at the Tevatron collider, direct production of $t\bar{t}$ pairs (1.10) dominates over top production via weak W decay (1.11) for all values of the top mass. Henceforth we will concentrate on the direct production process.

The theoretical calculation of $t\bar{t}$ production is based on the QCD improved parton model. According to this model, the cross section for process (1.10) can be factored as follows:

$$\sigma(S, \mathrm{m_{top}}, \mu_R, \mu_F) = \sum_{i,j} \int_{\tau_0}^{1.0} dx_1 \int_{\frac{\tau_0}{x_1}}^{1.0} dx_2 \, f_i^p(x_1, \mu_F)\, f_j^{\bar{p}}(x_2, \mu_F)\, \hat{\sigma}_{ij}(x_1 x_2 S, \mathrm{m_{top}}, \mu_R, \mu_F) \tag{1.17}$$

where $\sqrt{S}$ is the $p\bar{p}$ center of mass energy, and $\tau_0 = 4\mathrm{m}_{top}^2/S$. The functions $f_i^p(x, \mu_F)$ are parton distributions inside the proton. In a frame where the proton momentum is very large, they represent the number density of partons of type i sharing a fraction between x and $x + dx$ of the proton's momentum, and with a transverse size greater than $1/\mu_F$. Currently, deep inelastic scattering experiments determine the form of the light quark distributions in the range $x \geq 0.01$ and $\mu_F < 15\,\mathrm{GeV/c^2}$. Because the gluon does not couple to an electroweak probe, these experiments only indirectly constrain the gluon distribution. The parton cross section $\hat{\sigma}_{ij}$, for the process $ij \to t\bar{t}X$, is evaluated by expanding in powers of the running strong coupling constant $\alpha_S(\mu_R)$, where μ_R is the renormalization scale used to subtract ultraviolet divergences. Although μ_R is a priori arbitrary, it should be of the order of the largest momentum transfer in the hard scattering studied, for the expansion to be meaningful. Divergences arising from the emission of collinear gluons are factored from the parton cross section and inserted into a redefinition of the parton distributions. This factorization procedure makes the f_i^p functions dependent on a (a priori arbitrary) scale μ_F. Usually μ_R and μ_F are chosen equal. The boundaries of the integration region in (1.17) reflect the kinematical threshold $x_1 x_2 S \geq (2\,\mathrm{m_{top}})^2$, where we neglect incoming hadron masses. That the x_i be bounded away from zero is necessary for the factorization formula to be valid [Ell79]. Processes in which arbitrarily soft partons contribute (such as the total hadron–hadron cross section) cannot be properly described in the parton model. The sum on i, j runs over the gluon and the quarks lighter than the top [Nas89]. Indeed, flavour excitation graphs (figure 1.2) are not included: diagrams which appear to correspond to this process are genuinely higher order corrections in this approach [Ell89,Col86].

The factorization equation given above neglects interactions involving more than one parton per hadron. Such interactions require the transfer of a large momentum from one parton to another, and are suppressed by powers of this large momentum. Final state interactions, which cause the decay or hadronization of the produced top quarks, are assumed to be independent of the hard scattering described by $\hat{\sigma}_{ij}$.

The short distance cross section $\hat{\sigma}_{ij}$ has been completely calculated to order α_S^3 [Nas88,Nas89]. Leading and next-to-leading order diagrams are shown in

figure 1.3. The momentum scale describing heavy quark production is of the order of the heavy quark mass. Thus a natural choice for the renormalization and factorization scale is $\mu_R = \mu_F = \mathrm{m_{top}}$. Since $\mathrm{m_{top}} \gg \Lambda_{\mathrm{QCD}}$, this justifies the use of perturbation theory to calculate the $\hat{\sigma}_{ij}$. At the Tevatron, gluon fusion processes dominate $t\bar{t}$ production for top masses below $\sim 100\,\mathrm{GeV/c^2}$ (figure 1.4). Above $100\,\mathrm{GeV/c^2}$, quark fusion processes take over. As mentioned before, gluon-quark processes (flavour excitation) only contribute at order α_S^3 (figure 1.2).

The top and antitop are produced predominantly centrally (with rapidity $y \stackrel{\mathrm{def}}{=} \frac{1}{2}\ln[(E+p_z)/(E-p_z)]$ near 0.0), close to each other in rapidity ($\Delta y \lesssim 1.0$), and with a transverse momentum of the order of their mass. Moreover, the shape of the differential cross section $d\sigma/dy\,dp_T^2$ in $\mathcal{O}(\alpha_S^3)$ is essentially the same as in $\mathcal{O}(\alpha_S^2)$, see figure 1.5. From this, one is tempted to conclude that the shape of this distribution is unlikely to be modified by higher order corrections in kinematic regions in which the cross section is large [Nas89].

The uncertainty on the theoretical prediction for $\sigma_{t\bar{t}}(S, \mathrm{m_{top}}) \equiv \sigma(p\bar{p} \to t\bar{t})$ comes from our lack of precise knowledge about Λ_{QCD}, the structure functions, and the effect of uncalculated higher order corrections. For each of these components, a reasonable range of uncertainty can be found, and propagated to $\sigma_{t\bar{t}}$. The envelope of all such induced variations of $\sigma_{t\bar{t}}(S, \mathrm{m_{top}})$ yields an estimate of the uncertainty on its theoretical evaluation. In [Ell89], the following details are provided. Data from several deep inelastic scattering experiments are interpreted to restrict Λ_{QCD} to the range:

$$100\,\mathrm{MeV} < \Lambda^{(5)} < 250\,\mathrm{MeV} \tag{1.18}$$

where $\Lambda^{(5)}$ is the QCD parameter in the $\overline{MS}$ renormalization scheme with five active flavours. Of all the parton distribution functions, the gluon one is the most difficult to measure, and hence contributes the largest uncertainty to the top production cross section calculation. The form of the gluon distribution function is correlated with the value of $\Lambda^{(5)}$ used to fit the data. Therefore, three sets of distribution functions due to Diemoz, Ferroni, Longo and Martinelli [Die88] are considered. These distributions have $\Lambda^{(5)} = 101, 173, 250\,\mathrm{MeV}$, and appropriately correlated gluon densities. Finally, the effect of uncalculated higher order contributions to $\sigma_{t\bar{t}}$ is gauged by varying the assumed equal factorization and renormalization scales in the range $\mathrm{m_{top}}/2 < \mu < 2\,\mathrm{m_{top}}$, with $\mu \equiv \mu_R = \mu_F$. This procedure can be understood by considering that the exact, physical cross section is independent of μ. Hence the residual μ dependence of a finite order perturbative calculation is an estimate of the magnitude of higher order effects. It can be seen from figure 1.6 that the order α_S^3 cross section is less sensitive to a change in μ around $\mathrm{m_{top}}$ than the leading order result. This is a sign of a healthy perturbative expansion. The logic behind the choice of range for μ is as follows. For a given top mass, the next-to-leading order cross section calculation reaches a maximum at the so-called "optimization scale" $\mu = \mu_{\mathrm{opt}}$. To a good approximation it is found that [Mar91]:

$$\mu_{\mathrm{opt}} = \frac{\mathrm{m_{top}}}{5}\left(1 + \frac{\mathrm{m_{top}}\,\mathrm{c}^2}{100\,\mathrm{GeV}}\right) \tag{1.19}$$

As $\mathrm{m_{top}}$ varies from 40 to 200 GeV/c^2, the ratio $\mu_{\mathrm{opt}}/\mathrm{m_{top}}$ varies from 0.3 to 0.6. Hence the scale choice $\mu = \mathrm{m_{top}}/2$ provides a reasonable upper bound on the theoretical cross section. The cross section decreases for $\mu > \mu_{\mathrm{opt}}$, and the choice $\mu = 2\,\mathrm{m_{top}}$ gives a cross section roughly as far below $\mu = \mathrm{m_{top}}$ as $\mu = \mathrm{m_{top}}/2$ is above.

Figure 1.7 shows the top quark production cross section at the Tevatron as a function of top mass. The band indicates the uncertainty on the theoretical calculation. As the top mass increases, the uncertainty on the cross section decreases because of the diminishing contribution from gluon fusion processes. For $\mathrm{m_{top}} = 40\,\mathrm{GeV/c^2}$ ($200\,\mathrm{GeV/c^2}$), the width of the uncertainty band is about 50% (15%). It is perhaps worth noting that the corresponding uncertainty on $\mathrm{m_{top}}$ for a given cross section stays roughly constant (± 3.5 GeV/c^2). This is because the cross section becomes less steep as $\mathrm{m_{top}}$ increases.

1.4 Top quark hadronization and decay

After its creation, a top quark dresses itself up as a hadron, and decays. Heavy quark hadronization and decay characteristics significantly affect the way an event with top will appear to a real detector. There is currently no fundamental understanding of hadronization: this is a soft process, not calculable within the framework of perturbative QCD. A heuristic, and empirically successful picture of hadronization is as follows. A quark is always created in a colour singlet state with respect to some recoiling system of quarks and/or gluons. As the two move apart, the colour field between them creates quark-antiquark pairs from the vacuum. The initial singlet partners then separately combine with one or two of these quarks to form colourless hadrons. Similarly to the treatment of the parton structure of hadrons, hadronization is described by a set of functions $D_q^h(z)$ whose parameterization is based on phenomenological arguments and comparison with data. The q-to-h fragmentation function $D_q^h(z)$ is defined as the probability density for finding a hadron of type h sharing a fraction between z and $z + dz$ of the energy of its parent parton, where this parton is of type q. In this definition we have assumed that D_q^h depends only on z. This is not necessarily true, but is plausible if the parton energy is large compared to all participating masses and transverse momenta. For the case of heavy quark fragmentation, Peterson *et al.* have provided an explicit model which is in good agreement with data on charm and bottom quarks [Pet83]. This model is based on the observation that a heavy quark does not have to give up much energy to pick up a light quark travelling at the same velocity. Hence heavy quarks should fragment into heavy hadrons with large z; the heavier the fragmenting quark, the larger the z value of the formed hadron. This feature is embodied in the Peterson heavy quark fragmentation function:

$$D_Q^H(z) = \frac{K}{z\left(1 - \frac{1}{z} - \frac{\epsilon_Q}{1-z}\right)^2} \tag{1.20}$$

where K is a normalization constant and ϵ_Q is a parameter expected to be proportional to $1/m_Q^2$.

In the minimal Standard Model, the top quark decays predominantly into a bottom quark and a charged intermediate vector boson:

$$t \to b + W^+ \tag{1.21}$$

Decays into quarks of a different generation:

$$t \to s + W^+ \tag{1.22}$$
$$t \to d + W^+ \tag{1.23}$$

are strongly suppressed due to the smallness of the Kobayashi-Maskawa matrix elements V_{ts} and V_{td} compared to V_{tb}. A tree-level calculation of the width of top quark decay into channel (1.21) is shown in figure 1.8.

When trying to identify final states with a top quark, the presence of light leptons coming from the decay of the W in (1.21) is a powerful tag. This tag is unfortunately not available in some extensions of the Standard Model which include charged Higgs bosons. If the mass of the Higgs allows it, the decay:

$$t \to b + H^+ \tag{1.24}$$

will be dominant for top masses smaller than the W mass plus the bottom quark mass. The Higgs then decays preferentially into the heaviest fermion-antifermion pair that is kinematically accessible: $c\bar{s}, \tau\nu_\tau, \ldots$, so that decays into the electron and muon channels are suppressed. If the top mass is larger than $M_W + m_b$, then process (1.21) becomes a real two-body decay and will no longer be negligible compared to (1.24).

Figure 1.8 shows how the decay width of the top quark increases with its mass. The heavier the top quark, the faster its weak decay. If its mass is large enough, the top may decay before hadronizing into a heavy meson. This may affect the signature of top events. If the top has time to form a meson with a lighter quark, this lighter quark may have sufficient energy to form an observable jet after the top has decayed. In addition, the top decay products will have a softer spectrum since the top gave up some of its energy to the lighter quark. However, since heavy quarks have hard fragmentation functions, these effects are not expected to be

significant. On the other hand, some interesting QCD polarization predictions can be tested if the top quark decays before hadronizing [Kan90]. The weak lifetime of the top and the time needed for hadronization effects to appear are compared in references [Orr90,Orr91]. After its creation from a $p\bar{p}$ collision, a top quark will be in a colour singlet state with respect to one of the beam remnants (in contrast with the $e^+e^- \to t\bar{t}$ case, where the t is always in a colour singlet state with respect to its $\bar{t}$ partner). Hadronization effects are likely to occur when the distance between the top and its remnant partner reaches 1 fm ($\approx 1/\Lambda_{\mathrm{QCD}}$) in their center of mass frame. A study of the colour structure of the leading order diagrams for top production leads to a prediction of the percentage of cross section for which hadronization effects can appear before the top quark decays, at the Tevatron. This is shown in figure 1.9, as a function of top mass. Below a mass of 110 GeV/c^2, the fraction is 100%. Above 165 GeV/c^2, hadronization is negligible.

If the top mass is in the vicinity of the W mass, some special effects could occur. If $\mathrm{m_{top}} \approx \mathrm{m_{bottom}} + m_W$, top mesons will decay in such a way as to give as much energy to the W as possible, keeping the W as far above threshold for real W production as possible. Hence the invariant mass of the hadronic system containing the bottom quark will be small. This favors top mesons decaying into a few exclusive channels: a real W plus a bottom meson [Gil88]. If, on the other hand, $\mathrm{m_{top}} + \mathrm{m_{bottom}} \approx m_W$, there should be some interference between the W and the $T_b \stackrel{\mathrm{def}}{=} t\bar{b}$ meson. Mixing between T_b and W causes some shift in the W mass (at most 2 MeV/c^2) and width (about .3%) [Dob88].

1.5 Lepton+jets signature at the Tevatron

The $t\bar{t}$ production process (1.10) gives rise to quite a variety of event topologies, as each W can decay either into leptons or into quark jets. By counting the allowed W decay modes we can estimate the branching fractions for each $t\bar{t}$ topology. This is shown in table (1.1), along with the most significant source of background for the range of top masses considered in this work (60–80 GeV/c^2). Note that the

$t\bar{t}$ decay mode	Branching %	Background
$e\nu b + e\nu b$	1.2	$Z^0 \to e^+e^-$
$\mu\nu b + \mu\nu b$	1.2	$Z^0 \to \mu^+\mu^-$
$\tau\nu b + \tau\nu b$	1.2	
$e\nu b + \mu\nu b$	2.5	$Z^0 \to \tau^+\tau^- \to e\mu$
$e\nu b + \tau\nu b$	2.5	
$\mu\nu b + \tau\nu b$	2.5	
$e\nu b + q\bar{q}b$	14.8	W+jets
$\mu\nu b + q\bar{q}b$	14.8	W+jets
$\tau\nu b + q\bar{q}b$	14.8	
$q\bar{q}b + q\bar{q}b$	44.4	QCD jets

Table 1.1: $t\bar{t}$ topologies, their branching ratios and some sources of background.

decay modes with the highest branching ratio suffer from the highest background rate. Topologies involving the τ-lepton are difficult to identify, and have not been explicitly investigated at $p\bar{p}$ colliders. The products of leptonic τ decays may however contribute a minor enhancement to other topologies.

Leptons originating from the semi-leptonic decays of heavy quarks will have a hard momentum spectrum: the heavier the quark, the harder the lepton momentum spectrum. On the other hand, if its momentum is very high, the lepton will be less isolated from the other decay products of the heavy quark, provided the quark is not too heavy. This can be seen by a simple kinematical calculation applied to the three-body decay $Q \to ql\nu$, where Q is a heavy quark, q a light quark, l a lepton, and ν a neutrino. One finds:

$$\sin\theta_{lq} \leq \frac{m_Q^2 - m_q^2}{2\, m_q\, |\vec{p}_l|/c} \tag{1.25}$$

where θ_{lq} is the opening angle between the lepton and the light quark, $\vec{p}_l$ is the lepton three-momentum, and m_Q, m_q are the quark masses. The above relation yields essentially no constraint on a 60 GeV/c^2 top quark decaying into a 20 GeV lepton. However, for the semileptonic decay of a b quark ($m_b \approx 5$ GeV/c^2) into a c quark ($m_c \approx 1$ GeV/c^2), the requirement $|\vec{p}_l| > 20$ GeV/c yields $\theta_{lq} \leq 37°$. This point will be of great help for separating $t\bar{t}$ from $b\bar{b}$ production.

In this thesis we will study $t\bar{t}$ topologies where one of the W's decays into an electron or a muon, whereas the other W decays hadronically:

$$p\bar{p} \;\to\; t\bar{t}X \to (e\nu b) + (q\bar{q}\bar{b}) + X \tag{1.26}$$
$$p\bar{p} \;\to\; t\bar{t}X \to (\mu\nu b) + (q\bar{q}\bar{b}) + X \tag{1.27}$$

In principle this gives at least four jets in the final state. However, for the top masses we will consider (60 GeV/c^2 $\leq$ m$_{top}$ $\leq$ 80 GeV/c^2), the b jets are rather soft and difficult to resolve. Hence the event characteristics we will be looking for are *an isolated high energy electron or muon, a neutrino* (observable as missing momentum in a sufficiently hermetic detector), *and at least two high energy jets.* The principal background for such a topology is the production of a W accompanied by two or more jets. When m$_{top}$ $< m_W + m_b$, the W's produced in (1.26) and (1.27) are virtual, so that the (lepton,neutrino) invariant mass is smaller than the W mass and can be used to separate top from W events. Unfortunately we can not measure the neutrino momentum component which is parallel to the incoming beams (since there can be no detector coverage in that direction). Hence, instead of the invariant mass, one has to use the transverse mass of the lepton and neutrino:

$$m_T(l,\nu) \stackrel{\text{def}}{=} \sqrt{2\,(p_T^l\, p_T^\nu - \vec{p}_T^{\,l} \cdot \vec{p}_T^{\,\nu})} \tag{1.28}$$
$$= \sqrt{2\, p_T^l\, p_T^\nu\, (1 - \cos\Delta\phi_{l\nu})} \tag{1.29}$$

where $\Delta\phi_{l\nu}$ is the opening angle between the lepton and the neutrino in the plane transverse to the incoming beams. When m$_{top}$ $> m_W + m_b$, the W produced is real, and the (lepton,neutrino) transverse mass distribution for top events no longer differs from that for W events.

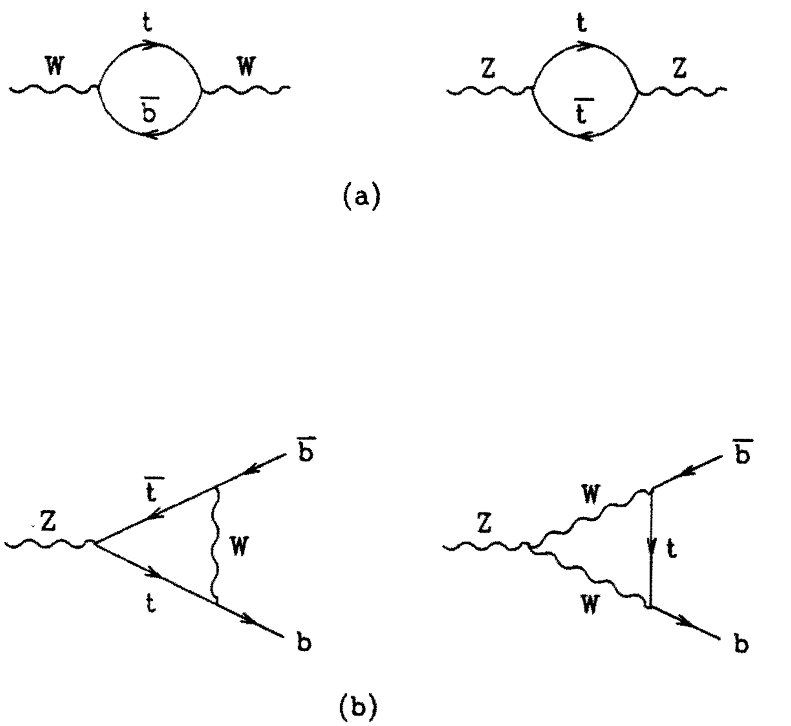

Figure 1.1: Radiative effects involving the top quark: (a) W and Z boson masses; (b) Vertex correction to the partial width $\Gamma(Z \to b\bar{b})$.

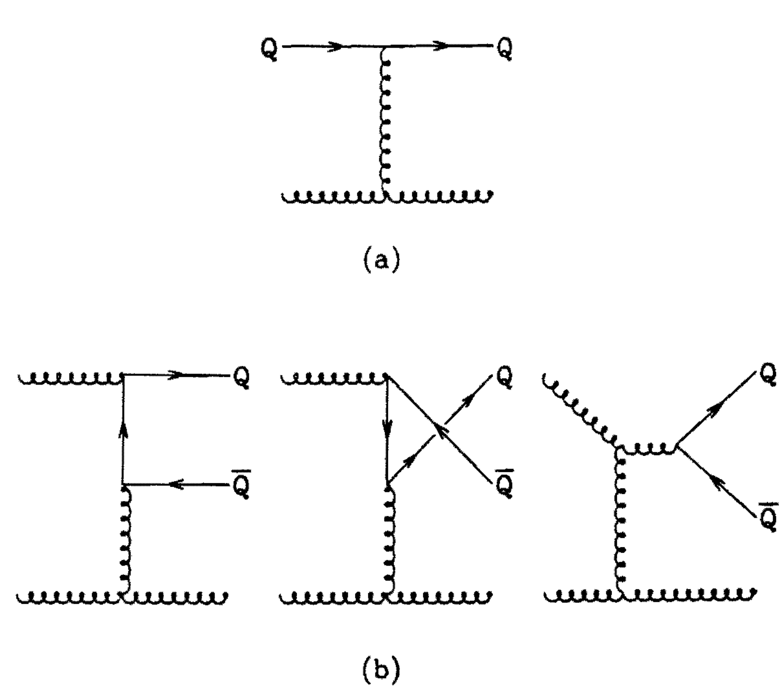

Figure 1.2: Flavour excitation graphs for $t\bar{t}$ production: (a) Leading order process; (b) Next-to-leading order processes. In the fragmentation region of the upper incoming hadron, the sum of the three diagrams in (b) cancels, thus showing that flavour excitation does not contribute in leading order. From [El189].

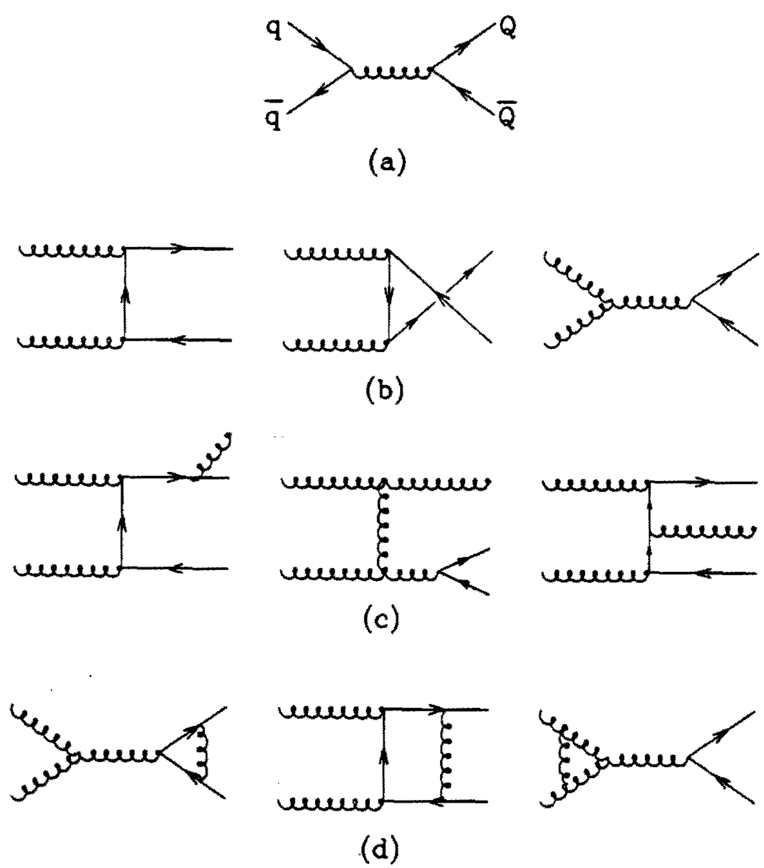

Figure 1.3: $t\bar{t}$ production diagrams: (a) Leading order quark fusion; (b) Leading order gluon fusion; (c) Some next-to-leading order real emission processes; (d) Some next-to-leading order loop diagrams.

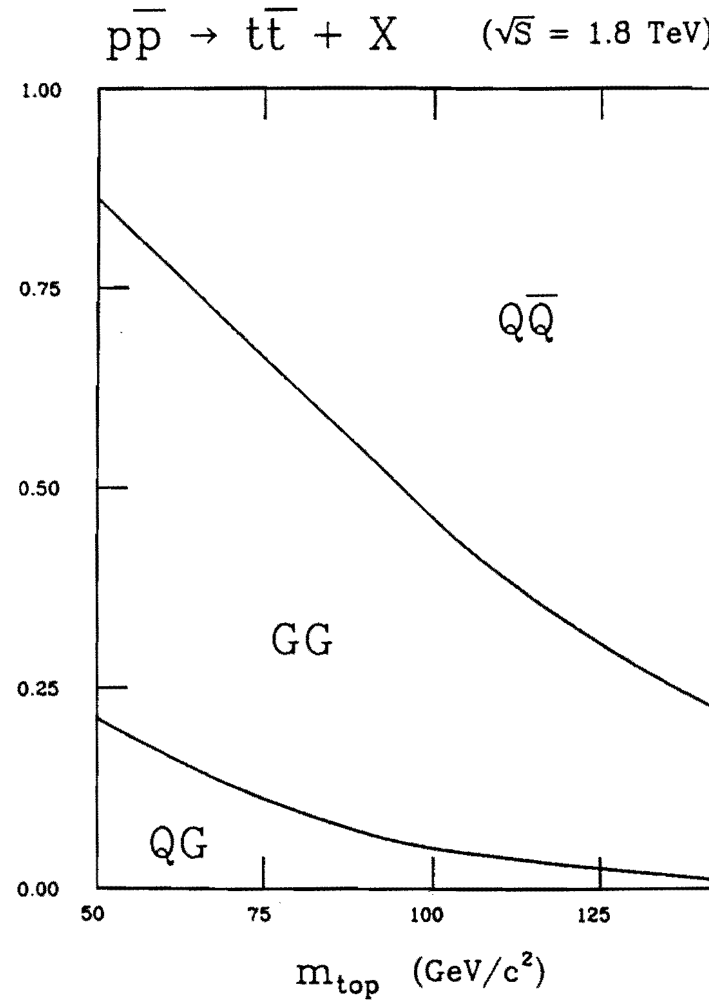

Figure 1.4: Subprocess contributions to $t\bar{t}$ production at the Tevatron. From [Mar89b].

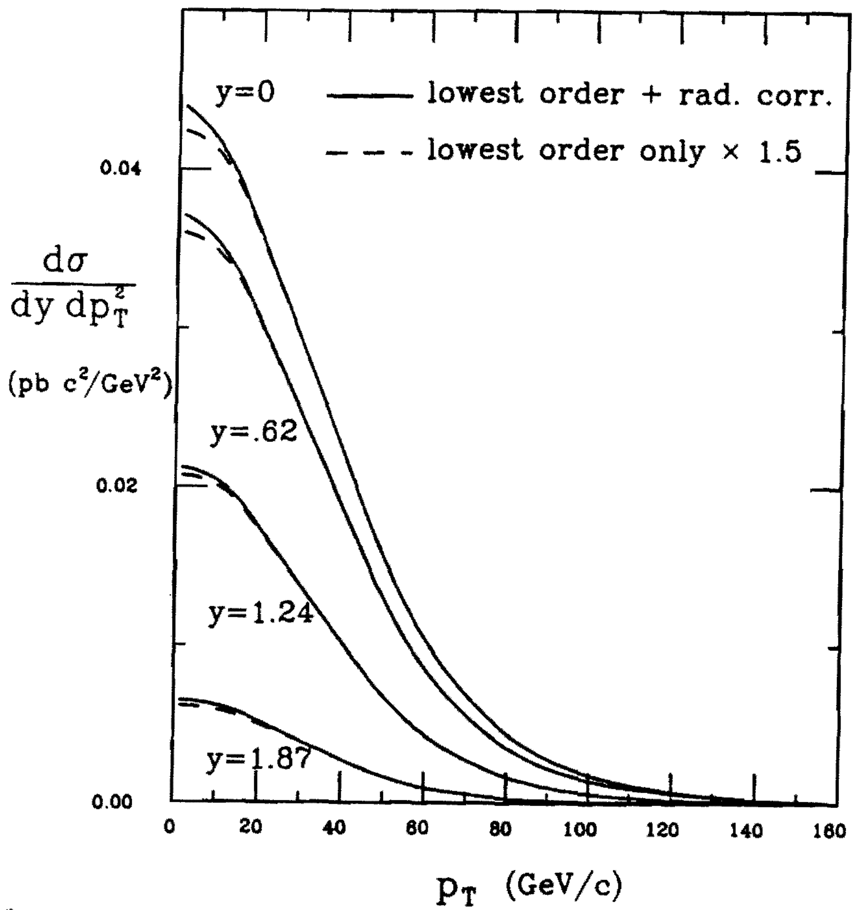

Figure 1.5: Differential cross section for the hadronic production of a heavy quark with a mass of 80 GeV/c^2 at $\sqrt{S} = 1.8$TeV. The cross section is plotted versus the transverse momentum for different values of the rapidity. The dashed lines represent the lowest order contribution scaled by an arbitrary factor. The structure functions of DFLM with $\Lambda^{(5)} = 173$ MeV are used. From [Nas89].

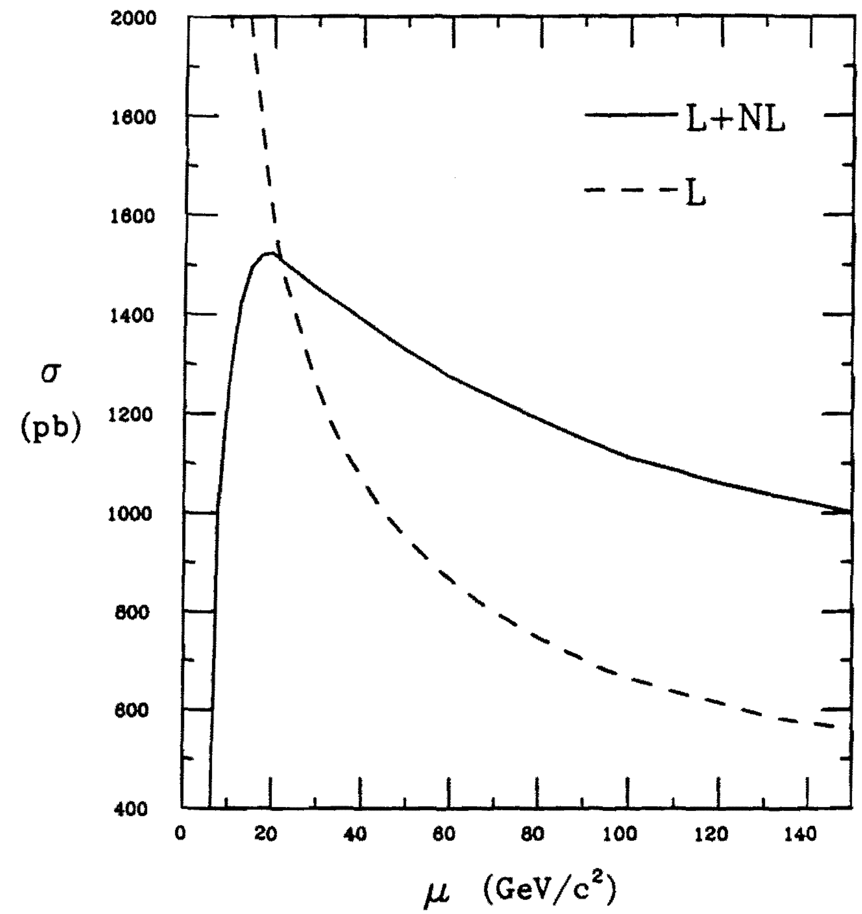

Figure 1.6: Dependence of the $t\bar{t}$ production cross section on the renormalisation and factorization scale μ. The DFLM structure functions were used. $\Lambda^{(5)} = 0.170$ GeV, $\sqrt{S} = 1.8$ TeV, and $m_{top} = 60$ GeV/c^2. From [Ell88].

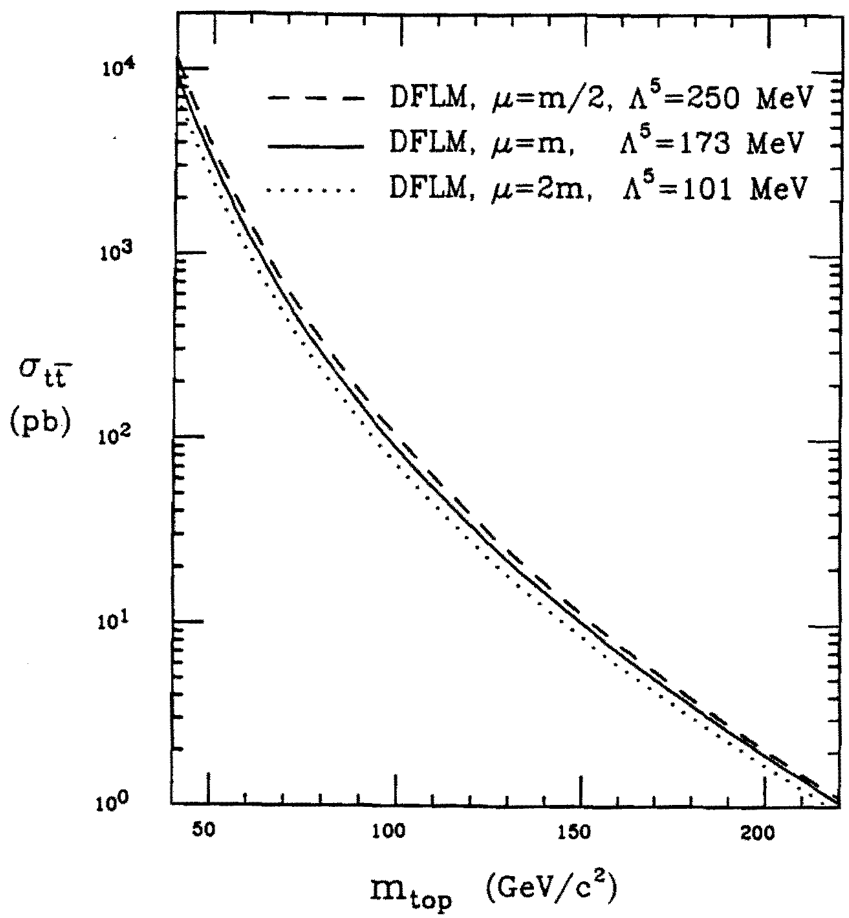

Figure 1.7: Cross section for $p\bar{p} \to t\bar{t}$ at $\sqrt{S} = 1.8$ TeV, to order α_S^3. From [Ell91].

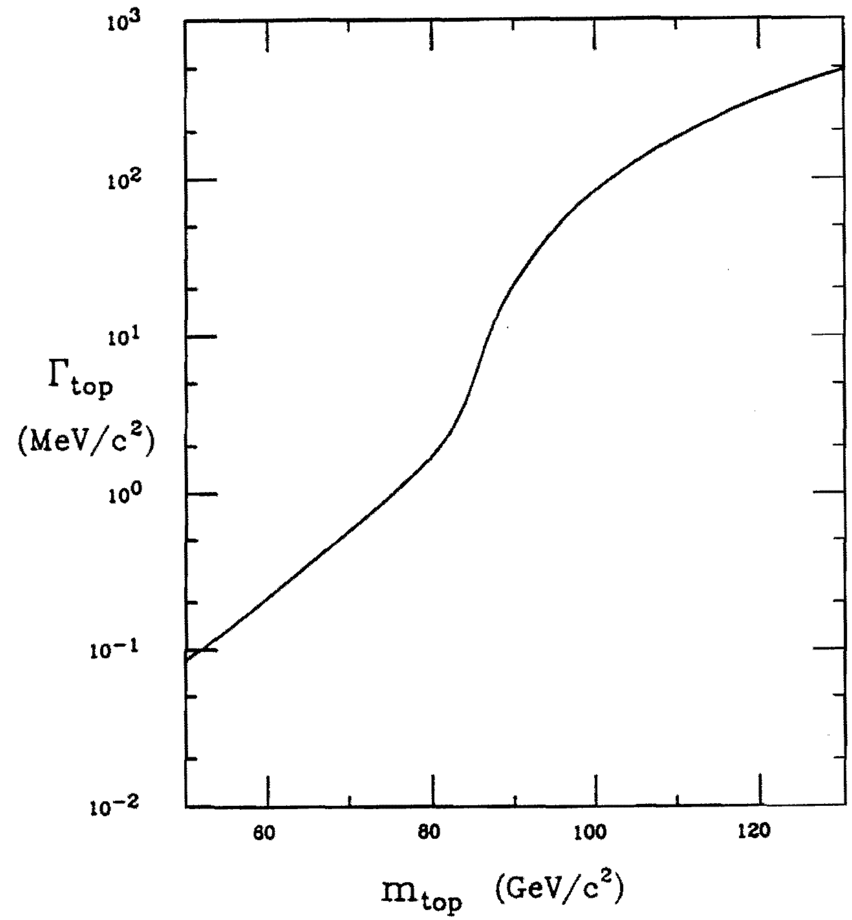

Figure 1.8: Tree-level calculation of the free top decay width versus its mass. From [Ros88].

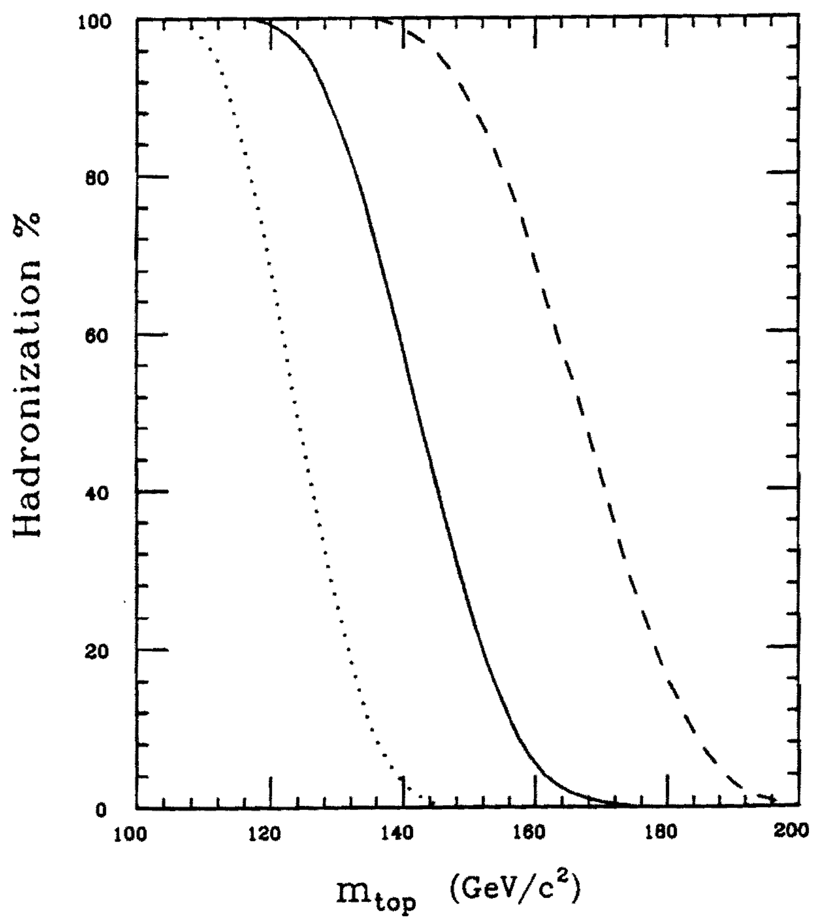

Figure 1.9: Percentage of the $t\bar{t}$ production cross section for which long distance effects due to hadronization occur before the top quark decays, as a function of top quark mass, for $p\bar{p}$ collisions at $\sqrt{S} = 1.8$ TeV. Solid line: Hadronization scale $\Lambda^{-1} = 1$ fm. Dashed line: $\Lambda^{-1} = 0.5$ fm. Dotted line: $\Lambda^{-1} = 2$ fm. From [Orr91].

Chapter 2

Apparatus

The Collider Detector at Fermilab (CDF) is the first general purpose detector built to exploit the Tevatron, a ring of superconducting magnets in which protons and antiprotons are made to collide at a center of mass energy of 1800 GeV. The detector is azimuthally and forward-backward symmetric. Perspective and cutaway views of CDF are shown in figures 2.1 and 2.2. CDF attempts to measure the energy, the momentum and in some cases the identity of particles produced by $p\bar{p}$ collisions over as large a fraction of solid angle as practical. Particles leaving the $p\bar{p}$ interaction region encounter successively the thin beryllium wall of the beam pipe, charged particle tracking chambers, sampling electromagnetic and hadronic calorimeters, and muon detectors. A superconducting solenoid in the central region provides a 1.4 T magnetic field used to analyze charged particle momenta. In this chapter we describe the CDF subsystems pertinent to our analysis. A complete description can be found in [Abe88] and references therein.

2.1 The CDF coordinate system

The CDF coordinate system is shown in figure 2.1. Its origin is at the center of the detector. The z-axis points in the direction of motion of the proton beam, from West to East. The y-axis points vertically upward, and the x-axis points radially out of the Tevatron ring, so as to make a right-handed coordinate system. The azimuthal angle ϕ is 0° on the positive x-axis and increases from positive x to positive y. The polar angle θ is measured from the proton beam direction. Instead of θ, one often uses the pseudo-rapidity $\eta \stackrel{\text{def}}{=} -\ln(\tan \frac{\theta}{2})$.

2.2 Beam-Beam Counters

The beam-beam counter system (BBC) consists of two planes of scintillation counters placed at a distance of 5.91 m on each side of the detector center. A beam's eye view of one of the BBC planes is shown in figure 2.3. The angular coverage of each plane is from 0.32° to 4.47° along either horizontal or vertical axes, or equivalently, $3.24 < |\eta| < 5.90$. The two principal functions of the BBC are to provide a minimum bias trigger and to monitor the accelerator luminosity. The minimum bias trigger is defined by the requirement that at least one counter fire in each BBC plane within a 15 ns window centered on 20 ns after the beam crossing time. The timing resolution of the counters is less than 200 ps. Luminosity monitoring will be described in section 3.2.

2.3 Tracking

2.3.1 Vertex Time Projection Chamber

The VTPC is a system of eight vertex time projection chamber modules mounted end to end along the beam line, and extending 1.4 m on each side of the center of the detector [Sni88]. The modules have an octagonal cross section with a diameter of 55.4 cm. A central high voltage grid partitions each module in two 15.25 cm long drift regions which terminate into proportional chamber endcaps (figure 2.4). As they move away from the central grid, electrons enter the endcap through a cathode grid. They then successively encounter a plane of field shaping wires, a plane of sense wires, and a cathode board coated with resistive ink. The other side of this cathode is clad with copper pads arranged in three concentric rows. The endcaps are subdivided in octants. Each octant contains 24 pads, and 24 sense wires strung perpendicularly to the octant's bisector. By measuring the drift times of electrons hitting the sense wires, a primary particle track can be reconstructed in the $R-z$ plane. The azimuth of a track is obtained by reading out the charge induced on the cathode pads. The VTPC provides three-dimensional track reconstruction for tracks with $|\eta| < 3.25$.

The main function of the VTPC system is to determine the location of the $p\bar{p}$ interaction point, by finding the point of convergence of all the reconstructed tracks in the event. The resolution on the z-coordinate of this measurement is about 1 or 2 mm, depending on the track multiplicity. Collision points have a gaussian distribution along the beam line, with $\sigma_z \approx 35$ cm, thus well within the coverage of the VTPC. The VTPC determination of the event vertex is used to compute the transverse component of the energy deposited in calorimeter elements. Approximately 15% of all the events recorded during the 1988-1989 run consist of more than one $p\bar{p}$ collision. Such events can be identified with the VTPC.

Materials used in constructing the VTPC were chosen to have low mass and long radiation length. This minimizes photon conversions and multiple Coulomb scattering which degrade track reconstruction efficiency and momentum resolution in the tracking chambers surrounding the VTPC. For tracks with $|\eta| < 1.5$, the VTPC presents less than 2% of a radiation length of material. In section 4.1.7, we will describe how the VTPC is used to identify photon conversions occurring between the VTPC and CTC active volumes.

Other uses of the VTPC include the measurement of the inefficiency of the beam-beam counters due to radiation damage. This measurement contributes to the calculation of the integrated luminosity of the CDF data samples.

2.3.2 Central Tracking Chamber

The Central Tracking Chamber (CTC) is a 3.20 m long cylindrical drift chamber surrounding the VTPC system [Bed88]. It has an inner diameter of 0.55 m, an outer diameter of 2.76 m, and fits inside a superconducting solenoid which provides a 1.4 T axial field. The chamber contains 84 layers of sense wires, arranged in 9 superlayers. In five of these superlayers, the wires are parallel to the beam line. These axial superlayers allow track reconstruction in the $R-\phi$ plane. They are interleaved with four stereo superlayers, in which the sense wires make a $\pm 3°$ angle with the beam axis to permit track reconstruction in the $R-z$ plane.

The maximum drift distance in the CTC is less than 40 mm, which corresponds to a maximum drift time of about 800 ns, well below the beam-beam crossing time of 3.5 μs. This maximum drift time is achieved by subdividing each superlayer into drift cells. Cells in an axial superlayer contain 12 sense wires; in a stereo superlayer they contain 6 sense wires. The cells are tilted by 45° with respect to the radial direction (figure 2.5). This large tilt angle has several advantages. It considerably simplifies resolution of the left-right ambiguity, which arises from the a priori impossibility to decide on which side of a sense wire a given track has passed. Combined with the large number of wires per cell, and of cells per superlayer, the large tilt angle also insures that tracks will come very close to at least one sense wire in each superlayer they cross. This condition can be exploited to separate closely spaced tracks in offline reconstruction. It can also be used to generate a fast trigger signal when one or more high transverse momentum (i.e. radial) tracks are present.

The transverse momentum resolution of the CTC is $\delta(1/p_T) = 0.0017$ (GeV/c)$^{-1}$ for tracks with $|\eta| < 1$, or $40° < \theta < 140°$ (these are tracks which cross all nine superlayers). This resolution can be improved to $\delta(1/p_T) = 0.0011$ (GeV/c)$^{-1}$ by adding the beam position to the $R - \phi$ fit of a track ("beam constrained fitting"). The resolution of the measurement of the azimuthal position in each layer is better than 200 μm, and the z-coordinate resolution of a stereo wire is less than 4 mm. The excellent position resolution of the CTC allows tracks to be matched with shower centroids measured in the calorimetry, or with hits observed in the muon chambers. This helps in the identification of high momentum electrons and muons. The CTC is also used to identify secondary vertices due to the decay of long-lived primary particles, to study calorimetry response as a function of momentum and position in the calorimeter, and to identify energy directed at cracks and holes in the calorimetry.

2.4 Calorimetry

The tracking chambers are surrounded by sampling calorimetry, which covers the full azimuthal range, and the pseudo-rapidity range $|\eta| < 4.2$. Calorimeters are segmented into approximately uniform (η, ϕ) bins called towers. All towers consist of an electromagnetic compartment in front of a hadronic one, and point to the center of the detector (the nominal $p\bar{p}$ interaction vertex). Different types of calorimetry instrument the central ($|\eta| < 1.1$), plug ($1.1 < |\eta| < 2.4$), and forward ($2.2 < |\eta| < 4.2$) regions.

For this analysis, the central electromagnetic calorimeter is used to detect isolated high transverse momentum electrons. Calorimeters in the central and plug regions are used to identify jets with a pseudo-rapidity less than 2.0. The transverse momentum of neutrino's from heavy flavour quark and W boson decays is reconstructed by measuring the transverse energy imbalance in calorimeter cells with $|\eta|$ up to 3.6.

2.4.1 Central region

The central calorimeter is azimuthally segmented into 15° wedges mounted around the solenoid. There are 48 wedges in all, 24 on each side of the $z = 0$ plane. Each wedge is subdivided along the z-axis into ten independently read out towers numbered from 0 to 9, where tower 0 is at 90° polar angle (figure 2.6). One wedge, called the chimney, is notched to allow access to the superconducting coil, and has only eight towers. The size of a central tower is approximately $\Delta\phi \times \Delta\eta = 15° \times 0.11$.

The electromagnetic section of each wedge [Bal88] is a stack of 31 layers of 0.5 cm thick polystyrene scintillator (the sampling medium) interspersed with 30 sheets of 0.32 cm thick lead absorber. The total thickness of the central electromagnetic calorimeter (CEM) is approximately eighteen radiation lengths; this includes one radiation length from the solenoid. At a depth of six radiation lengths, near the location of shower maximum, a proportional chamber allows an accurate determination of the centroid position and of the transverse extent of electromagnetic showers (figure 2.7). This is used to separate multiple showers in the same tower. This proportional chamber is referred to as the Central Electromagnetic Strip chamber (CES). It has wires strung along the beam direction for azimuth measurement, and cathode strips perpendicular to it for z-coordinate measurement.

The CEM was calibrated in a 50 GeV electron testbeam. Cesium sources are used to monitor long term gain variations with an accuracy of better than 2%. The CEM electron energy resolution is [Abe89]:

$$\left(\frac{\sigma(E)}{E}\right)^2 = \left(\frac{13.5\%}{\sqrt{E\sin\theta}}\right)^2 + (1.7\%)^2 \tag{2.1}$$

where the $\sin\theta$ factor reflects the increased sampling thickness seen by electrons entering the calorimeter at an angle. The position resolution of the CES is typically 2 mm for 50 GeV/c electrons.

The hadronic section of the central calorimeter wedges (CHA) has the same (η,ϕ) segmentation as the CEM, but only covers the range $|\eta| < 0.9$. A set of endwall hadron calorimeter modules (WHA) extends this coverage to $|\eta| = 1.3$ (figure 2.8) [Ber88]. The CHA modules are made up of 32 layers of 1 cm thick scintillator interleaved with layers of 2.5 cm thick steel. The endwall modules contain 15 layers of 5 cm thick steel followed by 1 cm thick scintillator. The energy resolution is approximately $\sigma(E)/E = 80\%/\sqrt{E\sin\theta}$. The arrival time of signals from the CHA and WHA phototubes is also measured. This information is used to reject out-of-time backgrounds such as cosmic rays.

2.4.2 Plug and Forward regions

The Plug and Forward calorimeters consist of layers of proportional chambers using a mixture of 50% Argon - 50% Ethane as sampling medium [Fuk88,Bra88,Cih88]. The radiator is lead in the case of electromagnetic calorimeters and steel in the hadronic detectors. A system of cathode pads ganged across layers provides the tower geometry. The tower size is $\Delta\phi \times \Delta\eta = 5° \times 0.09$ in the plug region, and $5° \times 0.1$ in the forward region. The energy resolution is approximately $\sigma(E)/E = 30\%/\sqrt{E\sin\theta}$ for electrons and $\sigma(E)/E = 120\%/\sqrt{E\sin\theta}$ for jets.

2.5 Central Muon chambers

Muons which have penetrated the 4.9 absorption lengths of the central calorimeter can be detected in the central muon chambers (CMU), 3.47 m away from the beam line [Asc88a]. These chambers are located behind the hadron calorimeter in each wedge (figure 2.9). They cover the region $|\eta| < 0.63$, and subtend 12.6° in azimuth, leaving 2.4° gaps between central wedges. Muon chambers are divided into three modules, each of which consists of four layers of four rectangular drift cells parallel to the beam axis (figure 2.10). A sense wire is located at the center of each cell. A particle entering a muon chamber along a radial direction will traverse four cells. The sense wires in the outer two cells are offset by 2 mm with respect to the two inner sense wires. This resolves the left-right ambiguity in the track azimuth measurement. Sense wires in alternate cells of the same layer are connected at the $\theta = 90°$ end of the chamber, and are read out separately at the other end. The z-coordinate of tracks is obtained by charge division along such paired sense wires. The angle α between a trajectory in a muon chamber and a reference plane containing the beam axis, is related to the curvature the track underwent in the magnetic field of the solenoid, and hence to its transverse momentum p_T:

$$\sin\alpha = \frac{qBL^2}{2D\,p_T} \tag{2.2}$$

with $B = 1.4116$ T the magnitude of the magnetic field, $L = 1.440$ m the radius of the solenoid, $D = 3.470$ m the distance from the beam line to the bottom of the CMU chambers, and q the charge of the detected particle. For small α, equation (2.2) gives:

$$\alpha \approx \frac{126\ \text{mrad}\cdot\text{GeV/c}}{p_T} \tag{2.3}$$

By measuring the difference in arrival times of drift electrons at the four sense wires crossed by a given muon, α can be calculated, and the muon transverse momentum subsequently derived. This information is used in the trigger. The resolution on the momentum measurement is dominated by the effect of multiple scattering of the muon in the calorimeter steel. The average scattering angle is:

$$\sigma(\alpha) \approx \frac{85 \text{ mrad} \cdot \text{GeV/c}}{p_T} \tag{2.4}$$

so that:

$$\frac{\sigma(p_T)}{p_T} = \frac{\sigma(\alpha)}{\alpha} \approx 67\% \tag{2.5}$$

2.6 Trigger system

At a luminosity of 10^{30} cm^{-2}s^{-1}, the total $p\bar{p}$ interaction rate is (71.5 ± 3.0) kHz [Apo91]. On the other hand, the rate at which events can be written to tape is around 1 Hz. The task of selecting interesting events for physics analysis is performed by a four-level trigger system. This staging of trigger decisions minimizes deadtime, while at the same time providing sufficient flexibility to exploit the strengths of CDF.

The lowest trigger level (level 0) selects inelastic $p\bar{p}$ collisions by a coincidence between the East and West beam-beam counters. This is the minimum bias trigger described in section 2.2. It is a prerequisite for subsequent levels. If the level 0 trigger accepts an event, data taking is inhibited during the next beam crossing, 3.5 μs later.

The level 1 trigger has 7 μs to reach its decision, which is based on information sent by the calorimeters, the central tracking chamber, and the muon chambers [Ami88]. The level 1 calorimetry trigger computes separate electromagnetic and (electromagnetic + hadronic) transverse energy sums over trigger cells which are above a programmable threshold. A trigger cell is 15° in ϕ by 0.2 in η; it groups two towers in the central, and six towers in the plug and forward calorimeters. A hardware track processor [Fos88], the Central Fast Tracker (CFT), identifies prompt axial hits in the CTC and compares them with predetermined hit patterns in a look-up table to evaluate the corresponding track transverse momentum. The CFT covers the range 2.5 GeV/c $\leq p_T \leq$ 15 GeV/c with a resolution $\delta(1/p_T) = 0.035$ (GeV/c)$^{-1}$. At level 1, it signals the presence of a track with transverse momentum above a programmable threshold. The level 1 muon trigger

identifies track "stubs" in the muon chambers, and estimates their transverse momentum as explained in section 2.5 [Asc88b].

The output rate of level 1 into level 2 is of the order of 1 kHz. The level 2 trigger reaches a decision in about 10 μs [Ami88]. During this time, clusters of calorimeter energy are identified. For each cluster, the electromagnetic and total transverse energy, the centroid position , the width, and the p_T of tracks pointing to it are computed. A list of "golden muons", consisting of CMU stubs matched to CTC tracks, is also formed. This information is subsequently analyzed by dedicated level 2 processors which attempt a coarse identification of physical objects such as electrons, muons, tau leptons, photons, neutrino's and jets. Electrons for instance, are selected on the basis of their calorimeter cluster width, the ratio of electromagnetic to hadronic energy deposition, and the presence of a high p_T track pointing to the cluster. The muon selection is based on the presence of a track in the muon chambers and, optionally, on the amount of energy deposited in the associated calorimeter cell. If the level 2 trigger accepts an event, the entire detector is read out. This takes about 1 ms.

The output rate of level 2 into level 3 is a few Hz. At level 3, all of the data for a given event is available. The level 3 trigger system is a farm of parallel processors capable of executing filter algorithms written in FORTRAN [Bar88]. The level 2 event selection is refined by the use of more sophisticated clustering algorithms, a larger set of thresholds, matching parameters, etc. The level 3 system rejects approximately 50% of the events it processes.

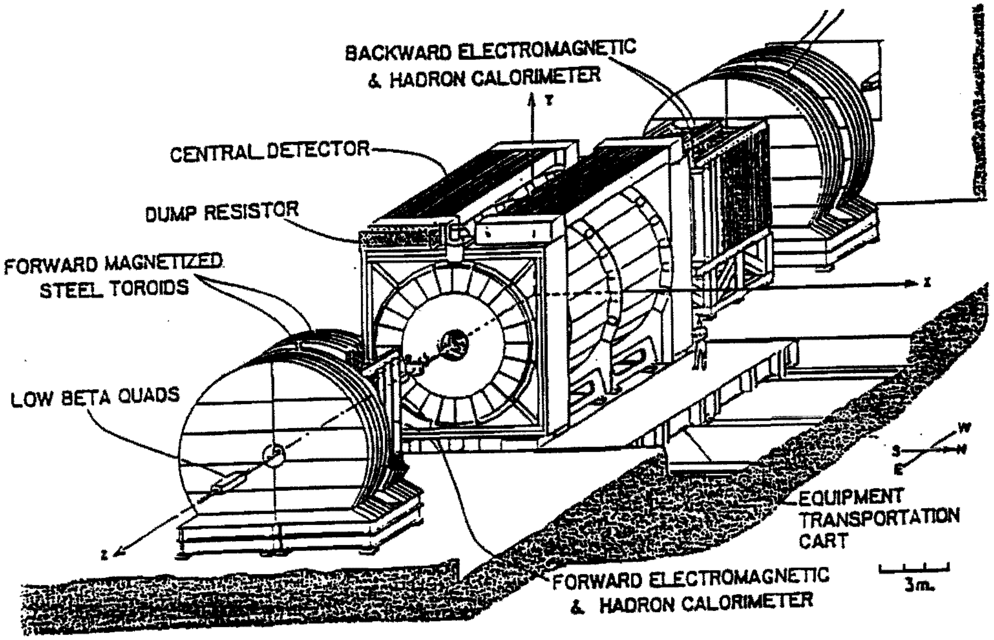

Figure 2.1: A perspective view of CDF showing the forward, central and backward detectors

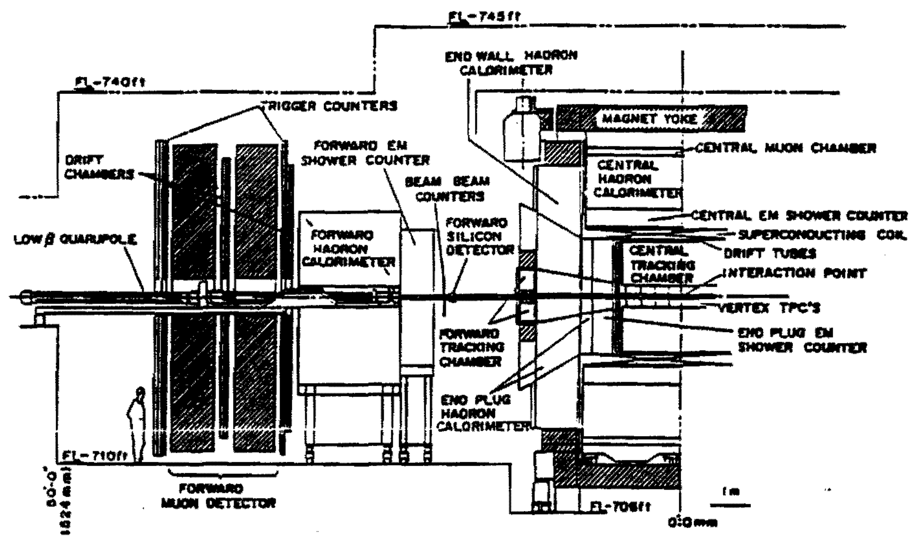

Figure 2.2: A cutaway view of the forward half of CDF. The detector is forward-backward symmetric about the interaction point

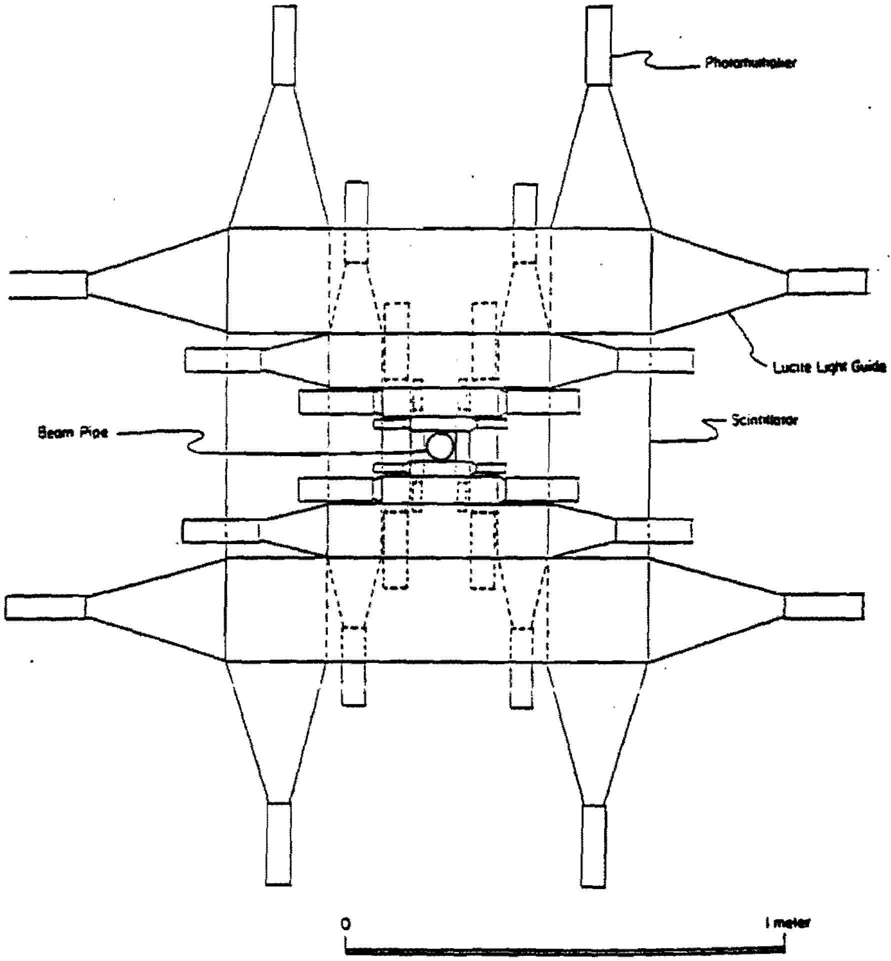

Figure 2.3: A beam's eye view of one of the beam-beam counter planes

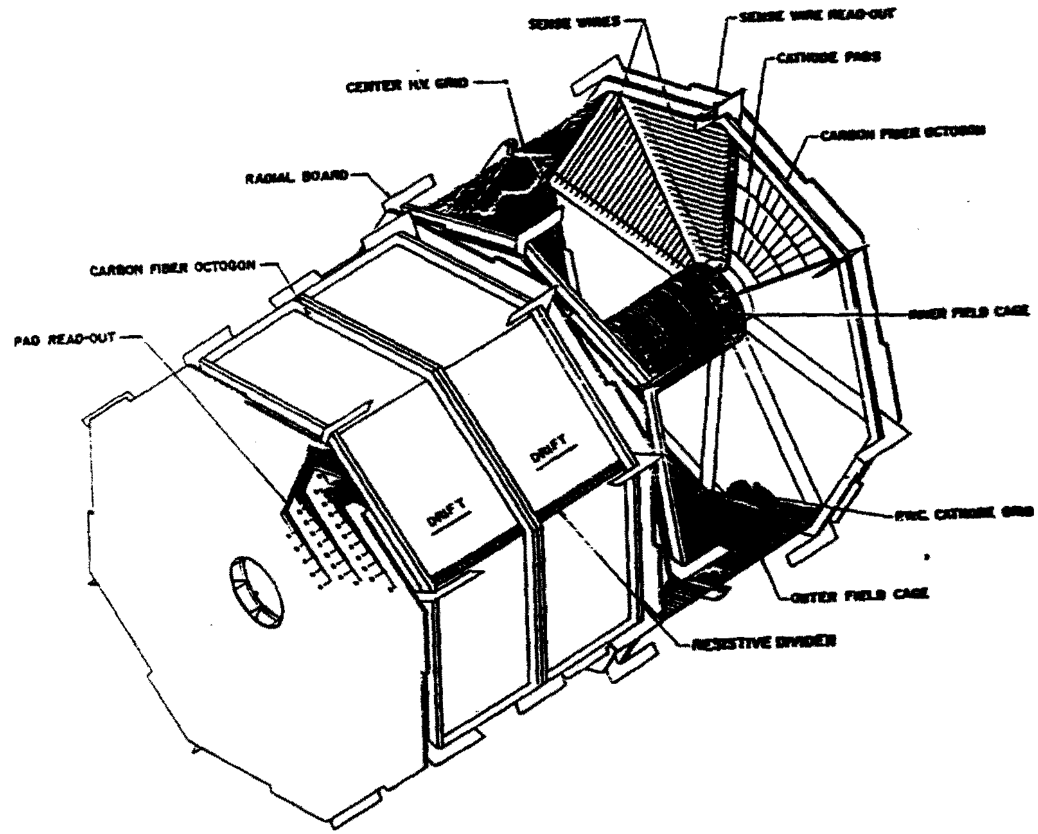

Figure 2.4: An isometric view of two VTPC modules. They are rotated by 11.3° with respect to each other.

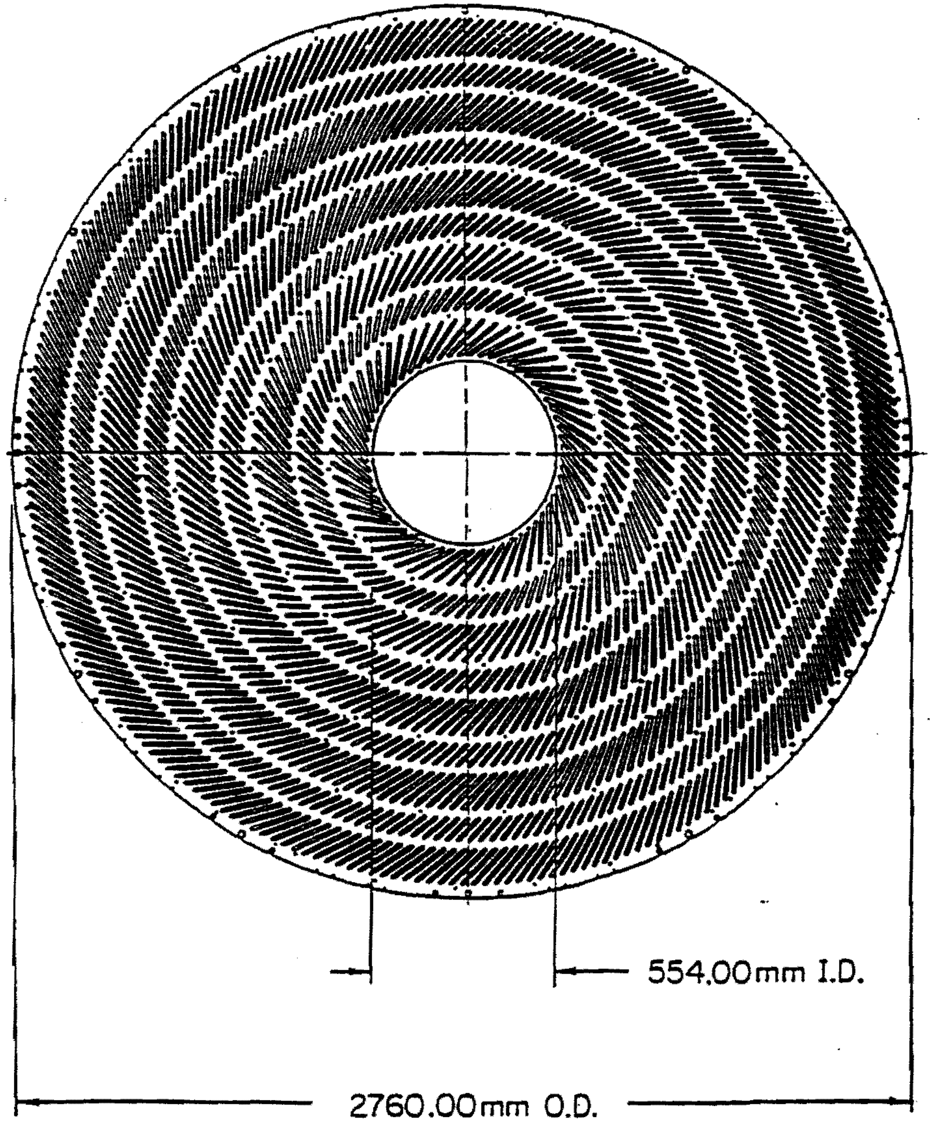

Figure 2.5: End view of the central tracking chamber, showing the disposition of the nine superlayers and drift cells within them

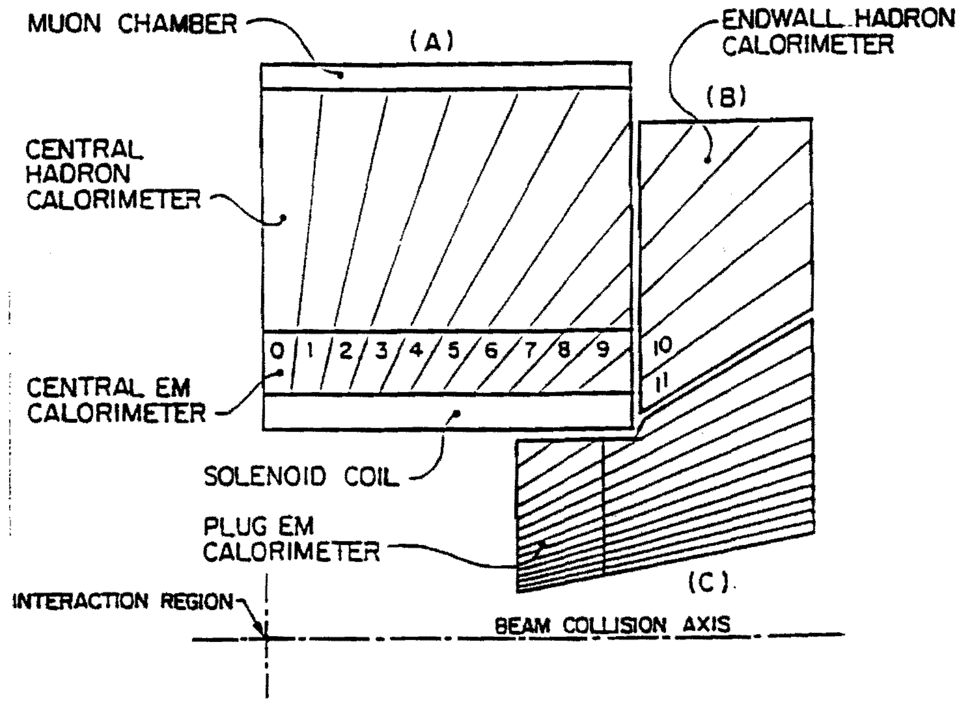

Figure 2.6: Cutaway view of a quadrant of the central (A), endwall (B), and plug (C) calorimeters; the tower numbering in the central and endwall calorimeters is indicated.

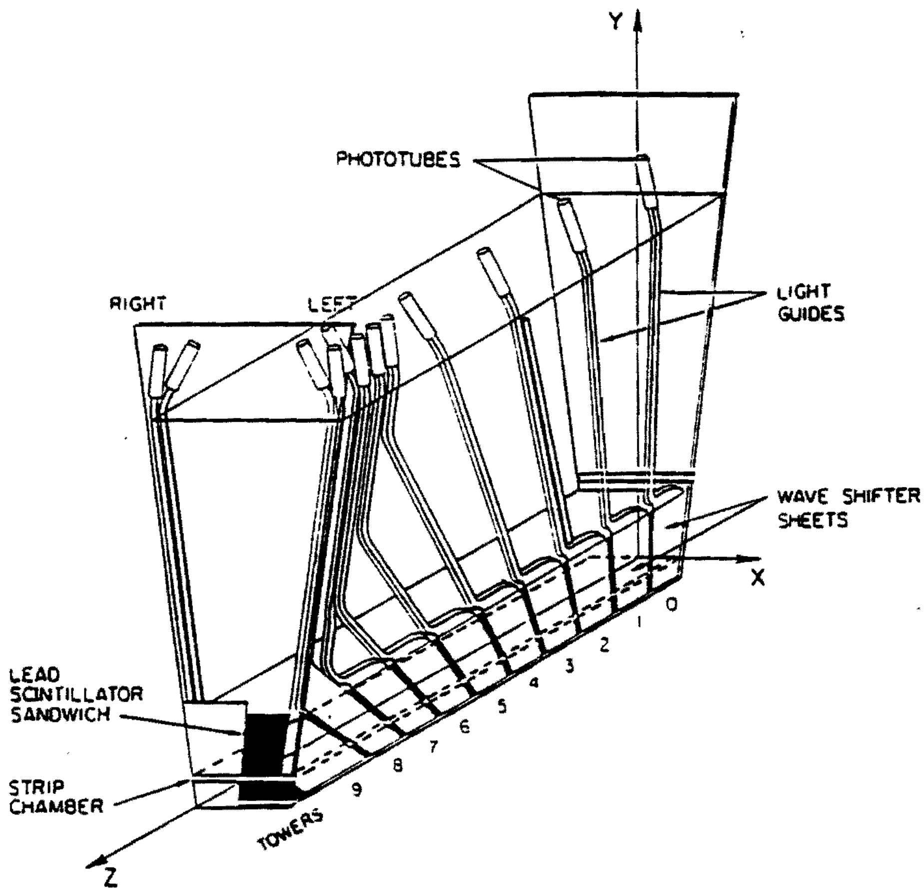

Figure 2.7: A central calorimeter wedge, showing the layout of the light-gathering system and the location of the strip chamber.

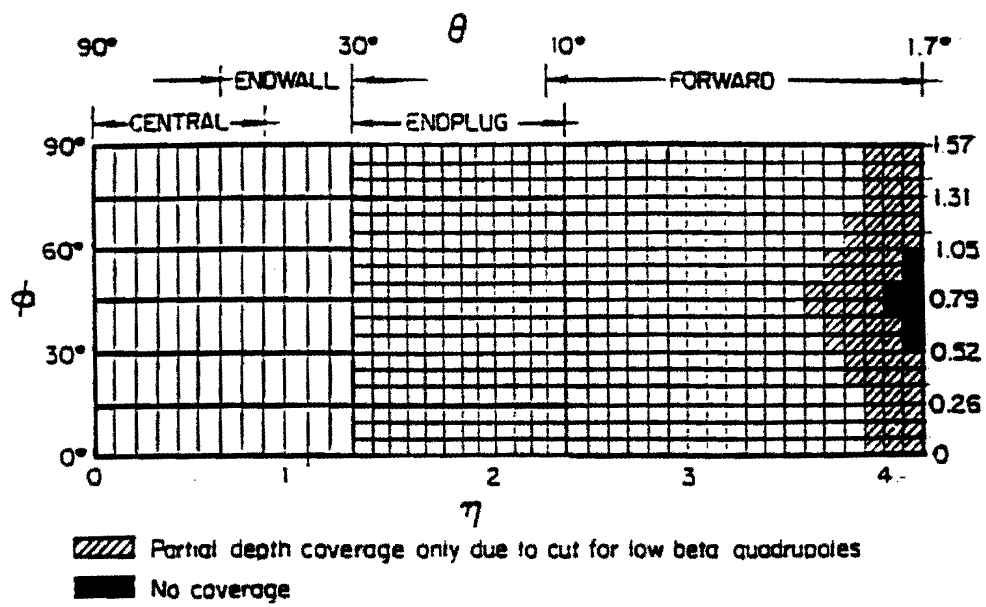

Figure 2.8: Tower segmentation in one of eight identical calorimeter quadrants ($\Delta\phi = 90°, \eta > 0$); heavy lines demarcate module or chamber boundaries.

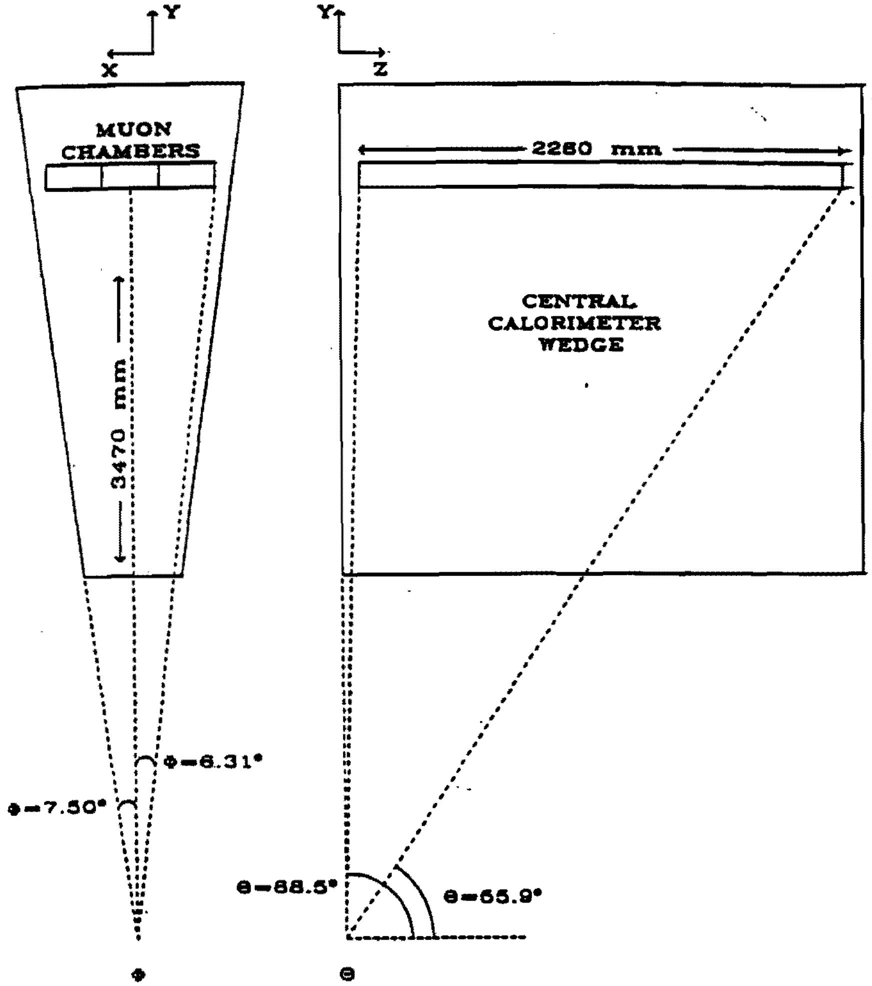

Figure 2.9: Central muon chamber location inside a central calorimeter wedge.

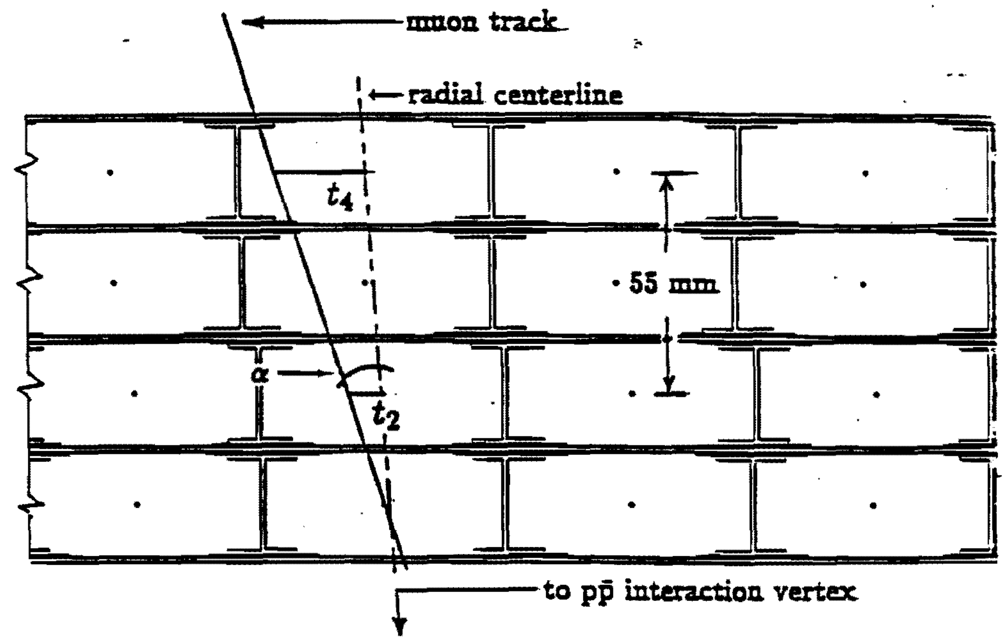

Figure 2.10: Cross section of a central muon module in the (R,ϕ) plane, showing the location of the sense wires.

Chapter 3

Luminosity Measurement

The first section of this chapter recapitulates the terminology used to discuss event rates and event selection at collider experiments. Subsequent sections describe how CDF measured its integrated luminosity for the 1988-1989 run.

3.1 Collider physics terminology

The purpose of a colliding beams experiment is to identify specific collision final states and quantify comparison with theory by measuring the rate R_c^{prod} at which they are produced. Event rates depend not only on the type of process studied, but also on the characteristics of the colliding beams. In order to relate the results of experiments operating at different colliders, one uses cross sections rather than event rates. The cross section σ_c is defined as the rate of events of type c, per target particle in the interaction region and per unit flux of incident beam relative to the target beam. Here, the distinction between incident and target beam is arbitrary. It follows from this definition that a given event rate is proportional to the corresponding cross section. The proportionality factor is the luminosity $\mathcal{L}$:

$$R_c^{prod} = \mathcal{L} \cdot \sigma_c \tag{3.1}$$

The luminosity depends only on beam properties, being the product of the area density in the target beam by the incident particle rate. In general, the cross section σ_c calculated by theory is for two body scattering: $a+b \rightarrow c$. Hence the above equation only holds under the assumption that the particles in each beam are sufficiently well separated that interactions within each beam and coherence effects can be neglected.

On the right hand side of equation (3.1), the rate R_c^{prod} is the number of events of type c *produced*. This is usually different from the *observed* event rate R_c^{obs}, since a physical detector can not possibly cover the entire solid angle around the interaction point, nor can it be fully efficient in identifying specific final states. It is therefore necessary to introduce the following concepts. The geometrical acceptance of a detector for a given final state, A_{geom}, is the fraction of produced events whose final state constituents fall within the fiducial, or sensitive region of the detector. In order to identify a final state constituent (determining whether it is an electron, muon, photon, jet, or neutrino), the responses from various parts of the detector are subjected to several tests. The probability that an object of type x passes all the tests that were set up for its identification is called the selection efficiency ϵ_x. This selection efficiency sometimes depends on the kinematical properties of the object under study. An electron for instance, to be successfully identified, must be somewhat isolated from the rest of the event, and must have a minimum amount of energy. Also, the ability to distinguish between two final states ('signal' and 'background') often rests on a difference in their kinematical configuration. Hence one is interested in the kinematical acceptance A_{kin}, which is the fraction of produced events whose constituents satisfy some simple kinematical requirements. Generally, A_{geom} and A_{kin} are correlated. It is therefore more convenient to talk about the acceptance A, defined as the combined kinematical and geometrical acceptance. We now have the relation:

$$R_c^{obs} = \mathcal{L} \cdot \sigma_c \cdot A \cdot \epsilon \tag{3.2}$$

where we wrote ϵ for the product of the individual efficiencies for identifying each final state constituent after the acceptance cuts. To summarize, measuring a cross section, or establishing an upper limit on a cross section, requires that one measure the accelerator luminosity at the interaction point, the event rate, the acceptance and the identification efficiencies.

3.2 Luminosity measurement and error

At CDF the luminosity is monitored by measuring the rate R_{BBC} of events for which at least one hit is recorded in both the East and West beam-beam counters (BBC). The absolute scale of the luminosity is obtained by introducing an effective BBC cross section σ_{BBC}^{eff}:

$$\sigma_{BBC}^{eff} \cdot \int \mathcal{L}\, dt = N_{BBC} \tag{3.3}$$

where $\mathcal{L}$ is the instantaneous luminosity and $N_{BBC} = \int R_{BBC}\, dt$. In this discussion, R_{BBC} is assumed to have been corrected for the occasional occurrence of multiple $p\bar{p}$ collisions per beam crossing. This is an upward correction, typically of order 8% when $\mathcal{L} = 10^{30}\,\mathrm{cm}^{-2}\mathrm{s}^{-1}$ [Gro90]. As a consequence of equation (3.3), the cross section σ_c for a given process can easily be calculated from the number N_c of events of class c observed:

$$\sigma_c = N_c \cdot \frac{\sigma_{BBC}^{eff}}{N_{BBC}} \tag{3.4}$$

To evaluate σ_{BBC}^{eff}, CDF combines measurements that were made at two different center of mass energies (546 GeV and 1800 GeV) with results obtained by the UA4 collaboration at the lower energy [Boz84]. The reason for using UA4 results is that the absolute scale of their luminosity is better understood than the one at CDF. In addition, the geometry of the UA4 double arm trigger counters is very similar to that of the BBC. We decompose the calculation of $\sigma_{BBC}^{eff}(1800\,\mathrm{GeV})$ into three steps:

1. Calculation of $\sigma_{BBC}^{eff}(546, \mathrm{UA4})$, the effective BBC cross section at 546 GeV, obtained by extrapolating UA4 results.

2. Calculation of $\sigma_{BBC}^{eff}(546, \mathrm{Tev})$, the effective BBC cross section at 546 GeV, obtained by combining measurements of Tevatron parameters with the BBC coincidence rate.

3. Calculation of the cross section ratio $r_\sigma \stackrel{\mathrm{def}}{=} \sigma_{BBC}^{eff}(1800\,\mathrm{GeV})/\sigma_{BBC}^{eff}(546\,\mathrm{GeV})$, from Tevatron parameters and BBC counting rates.

We have then:

$$\sigma_{BBC}^{eff}(1800\,\mathrm{GeV}) = r_\sigma \cdot \overline{\sigma_{BBC}^{eff}(546\,\mathrm{GeV})} \tag{3.5}$$

where we wrote $\overline{\sigma_{BBC}^{eff}(546\,\mathrm{GeV})}$ for the weighted average of $\sigma_{BBC}^{eff}(546, \mathrm{UA4})$ and $\sigma_{BBC}^{eff}(546, \mathrm{Tev})$. The following subsections describe in greater detail each component of the calculation. All the results quoted were extracted from reference [Gro90].

3.2.1 Calculation of $\sigma_{BBC}^{eff}(546, \mathrm{UA4})$

We use the following UA4 measurements [Boz84,Ber87]: the fraction f_{DA} of inelastic events that cause a double arm coincidence, the ratio of the elastic over the total cross section σ_{el}/σ_{tot}, and the total cross section σ_{tot}. The UA4 double arm effective cross section is then:

$$\sigma_{DA} = \left(1 - \frac{\sigma_{el}}{\sigma_{tot}}\right) \cdot \sigma_{tot} \cdot f_{DA} = (38.9 \pm 1.8)\,\mathrm{mb} \tag{3.6}$$

To extrapolate from σ_{DA} to $\sigma_{BBC}^{eff}(546, \mathrm{UA4})$, two effects must be considered. The first effect is the difference in geometrical coverage between the UA4 trigger counters and the CDF BBC. The corresponding ratio of acceptances, calculated using the MBR Monte Carlo [Bel84], is found to be 0.975 ± 0.025. The second effect is the BBC inefficiency due to radiation damage suffered during data taking. At 1800 GeV the BBC efficiency is measured from data triggered solely on beam crossings. The MBR Monte Carlo is used to extrapolate this efficiency to 546 GeV, giving a value of 0.978 ± 0.022. Combining both corrections independently yields:

$$\sigma_{BBC}^{eff}(546, \mathrm{UA4}) = \frac{Acc_\eta^{BBC}}{Acc_\eta^{UA4}} \cdot \epsilon^{BBC} \cdot \sigma_{DA} = (37.1 \pm 2.1)\,\mathrm{mb} \tag{3.7}$$

3.2.2 Calculation of $\sigma_{BBC}^{eff}(546, \mathrm{Tev})$

For bunched beams whose transverse density profile is bi-gaussian, the luminosity at the crossing point is:

$$\mathcal{L} = B\,\frac{N_p\, N_{\bar{p}}}{4\pi\, \sigma_x\, \sigma_y}\, f \tag{3.8}$$

with f bunch revolutions per second, B bunches per beam, N_p ($N_{\bar{p}}$) particles per bunch in the proton (antiproton) beam, and transverse bunch widths σ_x, σ_y at the interaction point. In fact, equation (3.8) is only an approximation, and must be modified to take into account the variation of beam parameters from bunch to bunch, the gaussian shape of the longitudinal bunch profile, and the effect of the momentum dispersion of the beams. In addition, some bunch parameters evolve with time during a store. The transverse profile of the beams is calculated from the accelerator lattice function and from measurements made with flying wires (wires moved through the beams [Gan89]). A resistive wall current monitor ('sampled bunch display' [Moo89]) measures bunch intensities and longitudinal profiles. After dividing the observed BBC rate by this luminosity measurement one finds $\sigma_{BBC}^{eff}(546, \mathrm{Tev}) = (32.8 \pm 3.6)$ mb. The 11% error comes mainly from the uncertainty on the absolute calibration of the sampled bunch display (10%), and from the uncertainty on the accelerator lattice function (5%).

3.2.3 Calculation of $\sigma_{BBC}^{eff}(1800\,\mathrm{GeV})/\sigma_{BBC}^{eff}(546\,\mathrm{GeV})$

The cross section ratio is calculated according to the following equation:

$$r_\sigma \stackrel{\mathrm{def}}{=} \frac{\sigma_{BBC}^{eff}(1800\,\mathrm{GeV})}{\sigma_{BBC}^{eff}(546\,\mathrm{GeV})} = \frac{R_{BBC}(1800\,\mathrm{GeV})/\mathcal{L}_{accel}(1800\,\mathrm{GeV})}{R_{BBC}(546\,\mathrm{GeV})/\mathcal{L}_{accel}(546\,\mathrm{GeV})} \tag{3.9}$$

where the subscript *accel* indicates a luminosity measurement based on Tevatron accelerator parameters only. The numerator and denominator on the right-hand side of equation (3.9) are measured separately using the method of section 3.2.2. Both uncertainties on the absolute luminosity mentioned at the end of that section are independent of energy and cancel out of the ratio. Other effects however, should not be ignored. Dynamic beam-beam interactions cause the ratio $R_{BBC}/\mathcal{L}_{accel}$ to depend on R_{BBC} at the higher energy. This effect is seen in the data and is corrected for. Since the same accelerator lattice was used at 546 GeV and 1800 GeV, one would expect calculations based on lattice parameters to be energy independent. However, the actual parameter values are different at the two energies so that their relative contribution to the luminosity will also be different. Systematic uncertainties on the ratio result from this effect and have been

estimated. We find $r_\sigma = 1.30 \pm 0.06$.

3.2.4 Result

A weighted average of $\sigma_{BBC}^{eff}(546, \mathrm{UA4})$ and $\sigma_{BBC}^{eff}(546, \mathrm{Tev})$ produces $\overline{\sigma_{BBC}^{eff}(546\,\mathrm{GeV})} = (36.0 \pm 1.81)$ mb. Combining this result with the ratio r_σ described in the previous section yields finally: $\sigma_{BBC}^{eff}(1800\,\mathrm{GeV}) = (46.8 \pm 3.2)$ mb.

Chapter 4

Event Selection Tools

Our top search is based on a signature comprising a high transverse momentum lepton, missing transverse energy, and several jets. Event selection starts with the preparation of inclusive lepton samples. The electron sample is described in section 4.1, the muon sample in section 4.2. Each description starts with the relevant triggers. Next, parameters which are used offline to refine the trigger selection are defined, and a set of lepton identification cuts is presented. The efficiency of the offline lepton selection is then calculated using samples of Z^0 events (sections 4.1.6 and 4.2.6). In the last two sections of the chapter, a discussion is given of jet reconstruction in CDF, and the calculation and meaning of the missing transverse energy of an event are explained.

4.1 Inclusive electron selection

4.1.1 Inclusive electron trigger

The level 1 central electron trigger requires that a trigger cell (cfr. section 2.6) in the central electromagnetic calorimeter contain at least 6 GeV of transverse energy. The level 1 and level 2 triggers compute the transverse energy using the center of the detector rather than the true event vertex.

At level 2, a hardware processor seeds electromagnetic (EM) clusters with trigger cells having at least 4 GeV of EM transverse energy. The four cells adjacent on a side are added to the cluster if they have $E_T^{EM} > 3.6$ GeV. Each cluster cell becomes a seed to which neighbouring cells are attached if they pass the same E_T^{EM} cut. This process is continued until no more cells can be added. The total cluster E_T is computed by summing the hadronic and electromagnetic E_T over

all the cells in the cluster. Central EM clusters are matched in azimuth with stiff tracks found by the Central Fast Tracker. The level 2 electron trigger requires the existence of an electromagnetic cluster with $E_T > 12$ GeV, with a ratio of total E_T to electromagnetic E_T less than 1.125, and matched to a CTC track with transverse momentum greater than 6 GeV/c.

The level 3 electron trigger executes the same clustering algorithm as the one run offline (see section 4.1.2). This algorithm uses a finer cell segmentation than the level 2 trigger. Tracks are reconstructed with a resolution $\delta(1/p_T) = 0.007\,(\mathrm{GeV/c})^{-1}$. Level 3 electron clusters are required to have $E_T^{EM} > 12$ GeV, a ratio of hadronic to electromagnetic E_T less than 0.125, and a track with transverse momentum greater than 6 GeV/c. Electron candidates with 12 GeV $< E_T^{EM} <$ 20 GeV must satisfy the additional cut $L_{shr} < 0.5$, where L_{shr} is defined by equation (4.6).

The efficiency of the 12 GeV electron trigger has been measured by comparing with a lower threshold (7 GeV) electron trigger, and by studying W and Z events selected with an independent trigger [Abe90a,Abe91a]. For isolated electrons with $E_T > 15$ GeV, this efficiency was found to be $(98.0 \pm 0.5)\%$.

4.1.2 Electron candidates

Offline identification of electrons begins by searching for clusters of electromagnetic energy in the calorimeters. A clustering algorithm first looks for seed towers containing at least 3 GeV of transverse energy. For clustering purposes, the transverse energy of a tower is defined as $E \sin\theta$, where E is the energy deposited in the tower and θ is the polar angle of the line joining the true event vertex to the center of the tower. This center is located at the depth of shower maximum, and halfway in detector polar angle between the tower boundaries. Towers adjacent to a seed are added to the corresponding cluster if their transverse energy exceeds 0.1 GeV. Since electron showers are small compared to the size of a CEM tower, most central electron clusters consist of one or two towers. In the azimuthal direction, CEM towers are separated by approximately 1 cm of inactive dense material. Hence, showers which are sufficiently far from azimuthal boundaries to guarantee full calorimeter response will not leak across these boundaries. For these reasons, central electron clusters are restricted to three or fewer towers in the same wedge.

For an electromagnetic cluster to be considered as an electron candidate, the total EM E_T of the cluster must be greater than 5.0 GeV, and the ratio of hadronic E_T to electromagnetic E_T in the cluster must be less than 0.125. Additional requirements must be made to reject hadronic backgrounds and to separate electron from photon clusters. Parameters that help in this task are defined in the following section.

4.1.3 Central electron parameters

We describe the parameters which characterize central electrons offline.

Energy

The electron energy E is evaluated by summing the energies measured in each tower belonging to the electron cluster. Three successive corrections are applied to this measured electron energy [Abe91b]. Within a single tower, the response is corrected as a function of the shower center's location, which is measured in the strip chamber (see below). This response map is based on electron testbeam data. Next, variations in tower-to-tower response are normalized by comparing energy E and track momentum p in a sample of inclusive electrons with $E_T > 15$ GeV. Finally, an overall scale is determined by comparing the E/p distribution of a sample of W electrons with that of a radiative W Monte Carlo simulation.

Track momentum

Both the central electromagnetic calorimeter and the central tracking chamber cover the range $-1.1 < \eta < 1.1$. To distinguish them from photons, central electrons are required to have a three-dimensional track pointing to their calorimetry cluster. This track is used to determine the electron's three-momentum vector $\vec{p}$.

For high energy electrons, the momentum resolution of the CTC is worse than the energy resolution of the CEM. However, the electron direction is more accurately measured from the track than from calorimetry variables.

Transverse energy

The transverse energy of an electron is calculated as $E_T \stackrel{\text{def}}{=} E \sin\theta$, where E is the corrected calorimeter cluster energy and θ is the polar angle of the beam constrained electron track (cfr. section 2.3.2). This definition implies that $E/p = E_T/p_T$.

Strip chamber variables

As described in section 2.4.1, a gas proportional chamber (CES) is located close to shower maximum in the central electromagnetic calorimeter. This chamber is used to determine the shower center and to quantify the cleanliness of the electron signal. The shower profiles across the strips and across the wires are separately fitted to parameterizations derived from 50 GeV/c testbeam electron data [Har91]. In the strip view for instance, the fitting procedure obtains the z-coordinate of the shower center, Z_{CES}, and the strip cluster energy E_s by minimizing the function:

$$X^2(z,E) \stackrel{\text{def}}{=} \sum_{i=1}^{n} \frac{(E_i^{meas} - E\, q_i^{pred}(z))^2}{\sigma_i^2(z)} \tag{4.1}$$

where the sum extends over $n = 11$ channels. The E_i^{meas} represent measured channel energies, whereas the $q_i^{pred}(z)$ are predicted energies normalized to 1 and corresponding to a given z-coordinate of the shower center. Fluctuations in a single channel response are taken as

$$\sigma_i^2(z) = (0.026)^2 + (0.096)^2\, q_i^{pred}(z) \tag{4.2}$$

Equation 4.2 has been obtained from 10 GeV/c testbeam electron data. Since shower fluctuations and the location of shower maximum both vary with energy, the variance of a channel response can also be expected to depend on energy.

However, this dependence is common to all channels and hence does not affect the fitting.

To test a single electron or single photon hypothesis, one introduces the variable:

$$\chi^2_{Strips} \stackrel{\text{def}}{=} \frac{1}{4}\left(\frac{E_{CEM}}{10}\right)^{0.747} \sum_{i=1}^{n} \frac{(q_i^{meas} - q_i^{pred}(Z_{CES}))^2}{\sigma_i^2(Z_{CES})} \tag{4.3}$$

where $\{q_i^{meas}\}_{i=1}^{n}$ is the measured strip profile normalized to 1. The E_{CEM}-dependent factor in front of the sum sign compensates for the aforementioned energy dependence of σ_i^2 (E_{CEM} is the electron energy measured from the CEM cluster, which has better resolution than the CES measurement E_s).

The treatment of the wire view is entirely analogous to that of the strip view and consists in calculating the local x-coordinate X_{CES} of the shower center and the corresponding goodness of fit variable χ^2_{Wires}. A plot of the average CES chisquare $(\chi^2_{Strips} + \chi^2_{Wires})/2$ is shown in figure 4.1 for 50 GeV testbeam electrons and pions, and for electrons from $W \to e\nu$.

Finally, to verify that the electron track points to a region reasonably close to the shower center, two matching variables are used:

$$\Delta X = X_{extrap} - X_{CES} \tag{4.4}$$

$$\Delta Z = Z_{extrap} - Z_{CES} \tag{4.5}$$

where X_{extrap} and Z_{extrap} are the coordinates of the electron track extrapolated to the radius of the strip chamber. These variables help reject fake electron signals caused by a charged pion track which overlaps with a neutral pion showering in the electromagnetic calorimeter.

Relative hadron calorimeter response

The energy deposited in the hadron calorimeter behind the electron cluster is also measured. Its ratio to the uncorrected electron cluster energy, Had/EM, provides a criterion to distinguish electrons from hadrons. This can be seen from figure 4.2, where the ratio $Had/(Had + EM)$ is shown for 50 GeV testbeam electrons and pions.

Transverse shower development

The lateral sharing of energy between towers in an electromagnetic cluster is described by the variable L_{shr}:

$$L_{shr} \stackrel{\text{def}}{=} 0.14 \sum_i \frac{E_i^{dep} - E_i^{exp}}{\sqrt{(\Delta E)^2 + (\Delta E_i^{exp})^2}}\,, \tag{4.6}$$

where the sum runs over the two towers adjacent to the seed tower in the same azimuthal wedge. E_i^{dep} is the energy deposited in tower i, whereas E_i^{exp} is the energy expected in that tower. This expected energy is calculated from testbeam measurements of lateral shower development; it depends on the seed energy of the cluster and the direction of the shower impact point in the strip chamber relative to the event vertex. The denominator represents a normalization that takes into account the finite resolution of the energy measurement: $\Delta E = 0.14\sqrt{E}$ is the uncertainty on the cluster energy E, and ΔE_i^{exp} is the error in E_i^{exp} associated with a 1 cm error in shower impact point measurement.

Energy-momentum ratio

The ratio of the corrected electron energy to the beam constrained electron track momentum, $E/p \equiv E_T/p_T$, is used to verify matching between the CEM and CTC measurements of the electron energy. Since high energy electrons tend to radiate in the detector, and since the CTC only measures charged track momenta whereas the calorimetry captures most of the radiated energy, we expect the mean of the E/p distribution to be slightly above 1.

Electron isolation

The presence of energetic particles near an electron can be quantified by measuring the quantity:

$$Iso(R) \stackrel{\text{def}}{=} E_T^R - E_T^{cluster} \tag{4.7}$$

where E_T^R is the total electromagnetic plus hadronic transverse energy in a cone centered on the electron cluster and with radius $R \stackrel{\text{def}}{=} \sqrt{(\Delta\phi)^2 + (\Delta\eta)^2}$; $E_T^{cluster}$ is the uncorrected electron cluster transverse energy. Two radii are commonly used at CDF: $R = 0.4$ and $R = 0.7$.

The border tower transverse energy, BE, is also a measure of the non-isolation of an electron. It is defined as the total electromagnetic plus hadronic transverse energy, summed over all the towers adjacent, at a corner or on a side, to an electron cluster. Figure 4.3 shows the distribution of BE for an inclusive electron sample that passes the electron identification cuts listed in section 4.1.4.

4.1.4 Central electron identification

Electrons in the central detector are identified by the following cuts:

1. $Had/EM < 0.055 + 0.045 \times E/(100\ \text{GeV})$, where E is the uncorrected electron cluster energy.
2. $L_{shr} < 0.2$
3. $\chi^2_{Strips} < 15$. No cut is made on χ^2_{Wires}, because the wire profile is more easily distorted than the strip profile by Bremsstrahlung photons emitted by high energy electrons.
4. $|\Delta X| < 1.5$ cm
5. $|\Delta Z| < 3.0$ cm. The ΔX cut is tighter than the ΔZ cut because of the better CTC resolution in the plane transverse to the beam axis.
6. $E/p < 1.5$
7. Track quality cuts: the electron track is required to be fully reconstructed in three dimensions, and its point of closest approach to the beam axis is required to be no more than 5 cm away from the event vertex along the z-axis.

The parameters used for electron identification are histogrammed in figures 4.4 to 4.10. These distributions are for electrons which pass all the identification cuts in addition to the isolation requirement BE < 2 GeV. Arrows indicate where the cuts are made.

4.1.5 Central electron fiducial region

Fiducial cuts are applied on electrons to avoid cracks in the detector and insure the shower containment necessary for a reliable energy measurement. The central electron fiducial region is defined as follows:

1. The seed tower of the electron cluster must not be one of the outermost (large $|\eta|$) towers of the calorimeter.
2. When extrapolated to the strip chamber radius ($R_{CES} = 184$ cm), the electron track must be at least 2.5 cm away from azimuthal boundaries between central calorimeter wedges.
3. The shower position in the strip chamber must be at least 9 cm away from the $Z = 0$ plane (90° crack).

4.1.6 Electron identification efficiency

The method

The identification efficiency for high P_T electrons is measured on a sample of $Z^0 \to e^+e^-$ decays. The method consists in selecting events with two electron candidates, one of which passes all the identification cuts and combines with the second electron candidate to form an invariant mass close to the Z^0 mass. The mass requirement insures that the second electron candidate is in fact a true electron. This way, a sample of unbiased electrons is obtained to determine the efficiency of the identification cuts.

Let N be the total number of $Z^0 \to e^+e^-$ events produced. N can not be directly measured, since the efficiency ϵ for identifying an electron is a priori unknown. Call N_1 the number of Z^0's for which at least one leg passes the identification cuts, and N_2 the number of Z^0's for which both legs pass these cuts. We write ϵ_c for the efficiency of a single cut c, and call N_c the number of Z^0 events where one leg passes all the cuts and the other leg cut c. N_1, N_2 and N_c can be measured, and are easily seen to be related as follows to the unknowns

N, ϵ and ϵ_c:

$$\begin{aligned} N_1 &= \epsilon(2-\epsilon)\,N \\ N_2 &= \epsilon^2 N \\ N_c &= \epsilon(2\epsilon_c-\epsilon)\,N \end{aligned}$$

From this we derive:

$$N = \frac{(N_1+N_2)^2}{4N_2} \tag{4.8}$$

$$\epsilon = \frac{2N_2}{N_1+N_2} \tag{4.9}$$

$$\epsilon_c = \frac{N_2+N_c}{N_1+N_2} \tag{4.10}$$

The uncertainty on ϵ is computed by considering N_1 and N_2 as binomial variables with respective efficiencies $\epsilon_1 \stackrel{\text{def}}{=} \epsilon(2-\epsilon)$ and $\epsilon_2 \stackrel{\text{def}}{=} \epsilon^2$, on a sample space of size N. One finds:

$$\begin{aligned} \sigma^2_{N_1} &= N\,\epsilon_1(1-\epsilon_1) = N\,\epsilon(2-\epsilon)(1-\epsilon)^2 \\ \sigma^2_{N_2} &= N\,\epsilon_2(1-\epsilon_2) = N\,\epsilon^2(1-\epsilon^2) \\ \sigma^2_{N_1N_2} &= \sum_{n_1=0}^{N}\sum_{n_2=0}^{n_1}(n_1-\epsilon_1 N)(n_2-\epsilon_2 N)\,B(n_1;N,\epsilon_1)\,B(n_2;n_1,\epsilon_2) \\ &= N\,\epsilon^2(1-\epsilon)^2 \end{aligned}$$

where:

$$B(n;N,\epsilon) \stackrel{\text{def}}{=} \frac{N!}{n!\,(N-n)!}\,\epsilon^n(1-\epsilon)^{N-n} \tag{4.11}$$

Propagating to ϵ the uncertainties on N_1 and N_2 yields:

$$\sigma_\epsilon = \sqrt{\frac{\epsilon\cdot(1-\epsilon)\cdot(2-\epsilon)}{N_1+N_2}} \tag{4.12}$$

A similar calculation involving N_c leads to:

$$\sigma_{\epsilon_c} = \sqrt{\frac{\epsilon_c\cdot(1-\epsilon_c)\cdot(1+\epsilon/\epsilon_c-\epsilon)}{N_1+N_2}} \tag{4.13}$$

Selection of the $Z^0 \to e^+e^-$ sample

The sample of $Z^0 \to e^+e^-$ events is selected by requiring two central electron candidates with an invariant mass between 81 GeV/c^2 and 101 GeV/c^2. The first electron must pass all the electron identification and fiducial cuts, and satisfy $E_T > 20$ GeV. The second electron must pass the fiducial cuts and also have $E_T >$ 20 GeV. A loose isolation cut is placed on both electrons to reduce background from jets: $Iso(0.7) < 12$ GeV. There are 111 events satisfying these requirements. The dielectron invariant mass distribution for these events is shown in figure 4.11.

Results

The results of the efficiency study are summarized in Table 4.1

Cut	N_c	ϵ_c
$Had/EM < 0.055 + 0.045 \times E/(100\text{ GeV})$	110	.995 ± .005
$L_{shr} < 0.2$	109	.990 ± .007
$\chi^2_{Strips} < 15$	108	.985 ± .009
$\lvert\Delta X\rvert < 1.5$ cm	104	.965 ± .013
$\lvert\Delta Z\rvert < 3.0$ cm	107	.980 ± .010
$E/p < 1.5$	95	.920 ± .020
Track quality	106	.975 ± .011
All Cuts	88	.884 ± .024

Table 4.1: Electron selection cuts and their efficiencies as calculated from 111 $Z^0 \to e^+e^-$ events.

4.1.7 Removal of conversion electrons

A significant number of electrons that pass the identification and fiducial cuts come from photon conversions ($\gamma \to e^+e^-$) or Dalitz decays of π^0's ($\pi^0 \to \gamma e^+e^-$). We loosely refer to both processes as 'conversions'. The algorithm used to remove conversion electrons is described in detail in reference [Abe91a]. Photons may convert before entering the VTPC, in which case they are called inner conversions. When a photon converts in the material separating the VTPC from the CTC, it is called an outer conversion. Outer conversions do not leave a track in the VTPC. They can therefore be identified by measuring the parameter f_{VTPC}, defined as the number of VTPC hits found along the track path, divided by the number of hits expected. Another useful variable, m_{ee}, is the lowest invariant mass formed with the electron candidate track and any oppositely charged track within 30° in azimuth in the CTC. Distributions of the quantities f_{VTPC} and m_{ee} are shown in figures 4.12 and 4.13 for electrons which passed the identification cuts, the isolation cut BE < 2 GeV, and which have E_T > 20 GeV. Electrons are flagged as conversions if they fail at least one of the following cuts:

$$f_{VTPC} \geq 0.2 \tag{4.14}$$

$$m_{ee} \geq 0.5\,\mathrm{GeV/c^2} \tag{4.15}$$

Since inner conversions leave a track in the VTPC, they can only be identified if they fail the m_{ee} cut.

By studying a sample of electrons from Z^0 decays, it was verified that the VTPC has a very high track finding efficiency. Hence, electrons with $f_{VTPC} < 0.2$ constitute a pure sample of outer conversions which can be used to estimate the efficiency ϵ_{mass} of the mass cut. On the other hand, the fraction f_{prompt} of prompt electrons wrongly flagged as conversions can be evaluated by applying the mass cut using like sign tracks instead of opposite sign tracks in the definition of m_{ee}.

We would like to determine the overall conversion detection efficiency ϵ_{conv}, and the fraction f_{bg} of the final sample which is attributable to unidentified conversions. For this purpose, we introduce the notations n_f, $n_{\overline{f}}$, for the numbers of electron candidates which pass, respectively fail, cut (4.14), and n_{fm}, $n_{f\overline{m}}$, for the numbers of electron candidates which pass cut (4.14) and pass, respectively fail, cut (4.15). The numbers n_{prompt} of prompt electrons, and n_{inner} of inner conversions, can then be solved from the equations:

$$n_{f\overline{m}} = f_{prompt}\, n_{prompt} + \epsilon_{mass}\, n_{inner} \tag{4.16}$$

$$n_f = n_{prompt} + n_{inner} \tag{4.17}$$

The fraction of conversion background in the final electron sample is given by:

$$f_{bg} = \frac{(1-\epsilon_{mass})\, n_{inner}}{n_{fm}} \tag{4.18}$$

and the overall conversion detection efficiency by:

$$\epsilon_{conv} = \frac{n_{\overline{f}} + \epsilon_{mass}\, n_{inner}}{n_{\overline{f}} + n_{inner}} \tag{4.19}$$

The quantities f_{prompt}, f_{bg} and ϵ_{conv} depend on the transverse energy and isolation of the selected electron candidates. For electrons which satisfy all the requirements for identification, and which pass the cuts BE < 2 GeV and E_T > 20 GeV, we find $\epsilon_{conv} = 0.87 \pm 0.07$, $f_{prompt} = 0.027 \pm 0.003$, and $f_{bg} = 0.036 \pm 0.009$. A summary of the conversion analysis is provided in table 4.2.

Number of electron candidates:	$n_e = 4132$
with $f_{VTPC} \geq 0.2$:	$n_f = 3691$
with $f_{VTPC} \geq 0.2$ and $m_{ee} \geq 0.5$ GeV/c²:	$n_{fm} = 3236$
with $f_{VTPC} \geq 0.2$ and $m_{ee} < 0.5$ GeV/c²:	$n_{f\overline{m}} = 455$
with $f_{VTPC} < 0.2$:	$n_{\overline{f}} = 441$
Fraction of prompt electrons removed:	$f_{prompt} = (2.7 \pm 0.3)$ %
Efficiency of mass cut:	$\epsilon_{mass} = (76.0 \pm 5.5)$ %
Number of prompt electrons in sample:	$n_{prompt} = 3204 \pm 78$
Number if inner conversions in sample:	$n_{inner} = 487 \pm 49$
Conversions as fraction of final sample:	$f_{bg} = (3.6 \pm 0.9)$ %
Conversion removal efficiency:	$\epsilon_{conv} = (87.4 \pm 7.4)$ %

Table 4.2: Summary of conversion analysis for inclusive electrons with $BE < 2$ GeV and $E_T > 20$ GeV.

4.2 Inclusive muon selection

4.2.1 Inclusive muon trigger

The level 1 central muon trigger looks for a track crossing a central muon (CMU) chamber. It requires that the time difference between hits in two alternate layers of the chamber be lower than a given threshold. As explained in section 2.5, this corresponds to applying a minimum transverse momentum (p_T) cut to the track. During the 1988-1989 CDF run, two p_T cuts were used: a 5 GeV/c cut during approximately the first third of the run, and a 3 GeV/c cut later on. The efficiency of the level 1 central muon trigger has been studied using cosmic ray data [Gau89]. It is found to be $(92.3 \pm 0.5)\%$ for muons with $p_T > 15$ GeV/c. Most of the inefficiency is due to delta rays which confuse the time difference measurement in the CMU.

At level 2, the central muon trigger requires that a track with $p_T > 9.2$ GeV/c be found by the Central Fast Tracker, and that this track azimuthally match a stub in the muon chambers. The matching is done after extending the CTC track to the central muon chamber, taking into account multiple scattering and the error in the CFT determination of the track azimuth. The level 2 efficiency, determined from a sample of unbiased isolated muons, is $97.2^{+0.015}_{-0.027}$ %, for muons with $p_T > 15$ GeV/c [Gau90a].

The level 3 central muon trigger requires that a track with p_T above 11 GeV/c match central muon hits within ± 10 cm in the azimuthal direction. The efficiency of this trigger is $100.0^{+0.0}_{-2.8}$ % for muons with $p_T > 15$ GeV/c [Gau90b].

4.2.2 Central muon parameters

We now define the parameters used for identifying and analyzing central muons offline.

Track momentum and impact

The momentum of a muon is determined from the CTC track which matches best with the CMU segment. Parameters describing the quality of such a match will be defined below. To reduce contamination of the prompt muon sample by cosmic rays and by muons coming from decays in flight of kaons and pions, the CTC track can be required to pass close to the event vertex. Two variables are used for this. Let $\mathcal{P}$ be the point of closest approach of the muon track to the

beam axis. We define the impact parameter d as the distance between $\mathcal{P}$ and the beam axis, and z_{track} as the z-coordinate of $\mathcal{P}$.

Energy deposited in the calorimeters

By extrapolating the muon track from the CTC into the central calorimeter, one can find which tower the muon went through. Since muons are minimum ionizing particles, the energies EM_μ and Had_μ deposited in the electromagnetic and hadronic compartments of the muon tower will generally be small relative to the muon momentum. This allows to separate the muon signal from the background of interacting punch-through hadrons. Measurements made with 57 GeV/c testbeam muons give a mean EM_μ of 0.3 GeV, and a mean Had_μ of 2 GeV, as shown in figures 4.14 and 4.15. Figure 4.16 shows the total electromagnetic plus hadronic energy deposited by 57 GeV testbeam pions in the central calorimeters.

Track matching

To match a CTC track with a muon segment, a local wedge coordinate system is introduced, which has the y-axis pointing radially outward, the z-axis parallel to the global CDF z-axis, and the x-axis defined so as to make (x, y, z) right-handed. The bottom plane of the chambers is at $y = 0$, whereas $x = 0$ cuts through the azimuthal middle of the chambers, and $z = 0$ is the same as for standard CDF coordinates.

The muon track in the CTC is extrapolated to the muon chambers, where it is transformed to local wedge coordinates and undergoes survey corrections. The CTC track and CMU segment are then separately fit to straight lines in the xy and zy planes. In each plane, the differences in fitted intercept and slope between track and segment are used as matching parameters. Because of the better CTC resolution in the transverse plane, only the difference in intercept in the xy plane, ΔI_x, will be used in our analysis.

Muon isolation

Just as for electrons, we measure the isolation of a muon with the quantity:

$$Iso(R) \stackrel{\text{def}}{\equiv} E_T^R - E_T^{\mu-tower} \tag{4.20}$$

where E_T^R is the total electromagnetic plus hadronic transverse energy collected by the calorimeters in a cone of (η,ϕ) radius R centered about the muon track, and $E_T^{\mu-tower}$ is the total transverse energy measured in the calorimeter tower traversed by the muon.

The border tower transverse energy, BE, is also used in the muon case. It is the total electromagnetic plus hadronic transverse energy summed over all the towers adjacent, at a corner or on a side, to the tower penetrated by the muon. Note that in the case where an electron cluster contains more than one tower, the electron BE will be calculated somewhat differently than the muon BE. The BE distribution of muons which pass the identification cuts listed in section 4.2.3 is shown in figure 4.17.

4.2.3 Central muon identification

Muons in the central detector are identified by the following cuts:

1. $EM_\mu < 2$ GeV
2. $Had_\mu < 6$ GeV
3. $EM_\mu + Had_\mu > 0.1$ GeV
4. $|\Delta I_x| < 10$ cm
5. $|z_{track} - z_{event}| < 5$ cm, where z_{event} is the z-coordinate of the true event vertex.
6. $d < 0.15$ cm

Histograms of the parameters used to identify central muons, with arrows marking the cut values, are shown in figures 4.18 to 4.23. In addition to all the muon

identification cuts, the isolation cut BE < 2 GeV has been applied to the events histogrammed.

4.2.4 Central muon fiducial region

The detection efficiency of the central muon chambers (CMU) falls off near the edges because of field distortions. In order to avoid CMU regions where the detection efficiency is not well known, fiducial requirements are applied on each muon candidate. The muon track in the CTC is extrapolated to the radius of the muon chambers, where the following cuts are applied:

1. The track must be at least 1.5° away from the azimuthal boundaries of the central wedge it hits. Using the local wedge azimuth ϕ_{wedge}, this requirement translates to $1.5° < \phi_{wedge} < 13.5°$.
2. In the local wedge pseudo-rapidity η_{wedge}, the extrapolated track must satisfy $0.040 < \eta_{wedge} < 0.61$.
3. One of the central detector wedges is notched to allow a 'chimney' for access to the CDF superconducting solenoid. The muon fiducial region in that wedge has a smaller η range: $0.040 < \eta_{wedge} < 0.50$.

4.2.5 Removal of cosmic ray muons

Cosmic ray muons which cross the central detector in time with a beam crossing could easily be confused with the products of a real $p\bar{p}$ collision. Such muons however, have broader impact parameter and $|z_{track} - z_{event}|$ distributions than prompt muons. Also, the incoming leg of a cosmic ray track is usually more difficult to reconstruct since it has the wrong timing compared to an outgoing prompt track. Based on these characteristics, a cosmic ray filter has been developed [Byo90]. It rejects muons which are not attached to an event vertex within 60 cm of the center of the detector, or which have $d > 0.5$ cm or $|z_{track} - z_{event}| > 5$ cm. Muons which are within 2° of back to back in azimuth with a "bad" track with $p_T > 10$ GeV are also rejected. Here, a track is considered "bad" if it is not reconstructed in three dimensions, has too few hits or track segments in the CTC, has $d > 0.5$ cm, or has $|z_{track} - z_{event}| > 5$ cm. Finally, if a muon is back to back with a good track, it is treated as a cosmic ray if $|\eta_\mu + \eta_{track}| < 0.2$ and V/c > 0.5, where η is the pseudo-rapidity and V is the particle velocity obtained by fitting the two back to back tracks as a single track. For a cosmic ray, both tracks are created by a single muon moving in an approximately constant direction, so that V/c ≈ 1. In $Z^0 \rightarrow \mu^+\mu^-$ events on the other hand, the two muons move in opposite directions, and a combined fit to their velocities will yield V/c ≈ 0.

A scan of high p_T central muon candidates satisfying a loose isolation requirement indicates that the cosmic ray filter just described is more than 99.8% efficient for W and Z events, whereas the filtered sample contains less than 0.37% cosmic background.

4.2.6 Muon identification efficiency

The efficiency of the muon identification cuts is determined by the same method as for electrons (see section 4.1.6).

Selection of the $Z^0 \rightarrow \mu^+\mu^-$ sample

A clean sample of $Z^0 \rightarrow \mu^+\mu^-$ decays is obtained by selecting events with two central muon candidates, both of which pass the fiducial cuts, the cosmic ray filter, have a transverse momentum greater than 20 GeV, and satisfy the loose isolation requirement: $Iso(0.4) < 5$ GeV. In addition, one of the muons must pass all the identification cuts and the invariant mass of both muons must be between 65 and 115 GeV/c². There are 38 events satisfying these requirements. Their dimuon invariant mass distribution is shown in figure 4.24.

Results

The results of the efficiency study are summarized in Table 4.3

Cut	N_c	ϵ_c
$EM_\mu < 2$ GeV	37	0.986 ± .014
$Had_\mu < 6$ GeV	36	0.973 ± .019
$EM_\mu + Had_\mu > 0.1$ GeV	38	1.000 ± .000
$\lvert\Delta I_x\rvert < 10$ cm	38	1.000 ± .000
$\lvert z_{track} - z_{event}\rvert < 5$ cm	38	1.000 ± .000
$d < 0.15$ cm	38	1.000 ± .000
All Cuts	35	0.959 ± .024

Table 4.3: Muon selection cuts and their efficiencies from 38 $Z^0 \rightarrow \mu^+\mu^-$ decays observed in the CMU fiducial region.

4.3 Jets

Due to the confining properties of the strong interaction, quarks and gluons do not manifest themselves as isolated free particles. Rather, they fragment into jets of hadrons. When analyzed in (η, ϕ) space, a jet has the shape of a circular cone which covers several towers in the CDF calorimeters. In order to reconstruct the original parton energy from the final state jet, two tools are needed: a clustering algorithm capable of identifying the towers most likely to belong to a given jet, and a jet energy scale, which maps a given jet energy and (η, ϕ) location onto the corresponding parton energy. In this work however, we will not attempt to reconstruct parton energies from the measured jet energies. Instead, jets will be selected on the basis of their observed properties. For our Monte Carlo studies, we will use a detector model which is tuned on CDF electron and pion testbeam data [Abe91a].

4.3.1 Jet clustering algorithm

For clustering purposes, towers in the Plug and Forward calorimeters are combined to have the same size as in the Central calorimeter: $\Delta\phi \times \Delta\eta = 15° \times 0.1$. The transverse energy E_T of a tower is defined as the sum of the electromagnetic and hadronic transverse energies in that tower. The electromagnetic transverse energy of a tower is $E_{em}\sin\theta_{em}$, with E_{em} the energy deposited in the electromagnetic compartment of the tower, and θ_{em} the polar angle of a line connecting the true event vertex to a point ten radiation lengths away, at the η center of the tower. The hadronic transverse energy is defined similarly, using a line connecting the event vertex to a point three absorption lengths away. Jets are identified by finding seed towers, forming preclusters, extending preclusters into clusters, and finally arbitrating overlap regions between clusters.

The clustering algorithm starts by listing all the towers having more than 1 GeV of transverse energy. These are called seed towers. Seed towers which are adjacent to each other, either at a corner or on a side, are grouped into preclusters. This is done in such a way that in any precluster, tower E_T's are monotonically decreasing as one moves from the highest E_T tower to the edge of the precluster.

Preclusters are expanded into clusters by a fixed cone iterative algorithm. First, the E_T weighted (η,ϕ) centroid of the precluster is computed. Next, a cluster is defined as the set of towers containing more than 100 MeV of E_T, and within an (η,ϕ) radius of 0.7 from the centroid. The cluster centroid is then recomputed, and its set of towers redefined accordingly. This process is repeated until the set of towers no longer changes. The initial precluster towers are always kept in the cluster, regardless of their distance to the centroid. This prevents the centroid from shifting too far away in pathological situations.

If a cluster is completely contained in another cluster, the smaller one is dropped. If two clusters share a subset of towers, they are merged if the total E_T in the common towers is more than 75% of the E_T in the smaller cluster. Otherwise, the towers in the overlap region are divided between the two clusters according to their proximity to the cluster centroids. The centroids are subsequently recomputed, and the disputed towers reassigned, until a stable configuration is reached.

4.3.2 Jet parameters

The momentum vector of a jet cluster is calculated as the vector sum of the momenta of its towers. More precisely, let E^i_{em} and E^i_{had} be the electromagnetic and hadronic energies deposited in tower i, θ^i_{em} and θ^i_{had} the associated polar angles as defined at the beginning of the previous section, and ϕ^i the azimuth of the tower. The cluster momentum components are:

$$\begin{aligned}
P_x &= \sum_i (E^i_{em}\sin\theta^i_{em} + E^i_{had}\sin\theta^i_{had})\cos\phi^i \\
P_y &= \sum_i (E^i_{em}\sin\theta^i_{em} + E^i_{had}\sin\theta^i_{had})\sin\phi^i \\
P_z &= \sum_i (E^i_{em}\cos\theta^i_{em} + E^i_{had}\cos\theta^i_{had}) \\
E &= \sum_i (E^i_{em} + E^i_{had})
\end{aligned}$$

Thus the cluster momentum is approximately equal to the corresponding fragmenting parton momentum, in the limit where the particles forming the jet have a small mass compared to their energy. With the above components one can form the combinations:

$$\begin{aligned}
P_T &= \sqrt{P_x^2 + P_y^2} \\
P &= \sqrt{P_x^2 + P_y^2 + P_z^2}
\end{aligned}$$

and introduce the cluster pseudo-rapidity η and transverse energy E_T:

$$\begin{aligned}
\eta &\stackrel{\text{def}}{=} \frac{1}{2}\ln\left(\frac{P+P_z}{P-P_z}\right) \\
E_T &\stackrel{\text{def}}{=} E\,\frac{P_T}{P}
\end{aligned}$$

It is sometimes useful to define the detector pseudo-rapidity η_d, which is the pseudo-rapidity calculated with respect to the center of the detector instead of the primary event vertex. Our final jet selection (chapter 6) will be based on the E_T and η_d parameters.

4.4 Missing transverse energy

The missing transverse energy vector ($\vec{\not{E}}_T$) is defined as minus the vector sum of the transverse energies deposited in calorimetry towers over the pseudo-rapidity range $|\eta| < 3.6$:

$$\vec{\not{E}}_T \stackrel{\text{def}}{=} - \sum_{|\eta|<3.6} \vec{E}_T^{tower} \tag{4.21}$$

where $\vec{E}_T^{tower}$ is a two-dimensional vector pointing from the event vertex to the tower center. For a tower to be included in the sum, its energy content must be above a given threshold. This threshold is 0.1 GeV in the central electromagnetic and hadron calorimeters, 0.3 GeV in the plug electromagnetic calorimeter, 0.5 GeV in the plug hadron and forward electromagnetic calorimeters, and 0.8 GeV in the forward hadron calorimeter. Note that these are thresholds in energy, not transverse energy. A restricted pseudo-rapidity range is used in the definition of $\vec{\not{E}}_T$ because low-β quadrupoles from the Tevatron obscure part of the forward hadron calorimeters.

In the inclusive electron sample, the missing transverse energy as defined in equation (4.21) is used as an estimate of the total transverse momentum of the neutrino's in an event. Such an estimate is however inadequate for the inclusive muon sample, since muons leave very little energy in the calorimeters and hence contribute disproportionately to the sum in (4.21). To correct for this, the total neutrino transverse momentum for events in the inclusive muon sample is defined as:

$$\vec{E}_T^{\nu} \stackrel{\text{def}}{=} \vec{\not{E}}_T + \sum(\vec{E}_T^{\mu-tower} - \vec{p}_T^{\mu}) \tag{4.22}$$

where the sum runs over all the CTC tracks with $p_T^{\mu} > 15$ GeV and which satisfy the muon identification requirements of section 4.2.3, with the exception of the ΔI_s cut. This cut is dropped because of the limited fiducial coverage of the central muon chambers. The vector $\vec{E}_T^{\mu-tower}$ is calculated from the track direction and the electromagnetic plus hadronic energy deposited in the calorimeter tower pointed to by this track.

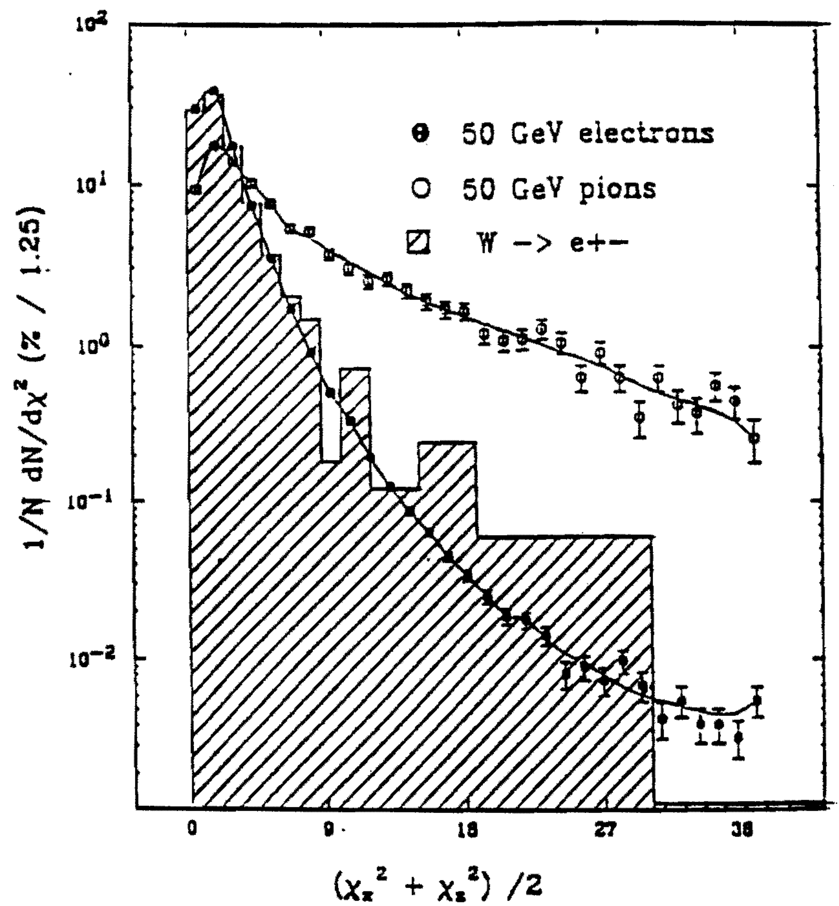

Figure 4.1: The average CES chisquare distribution for 50 GeV testbeam electrons and charged pions, and for electrons from W decays. From [Pro89a].

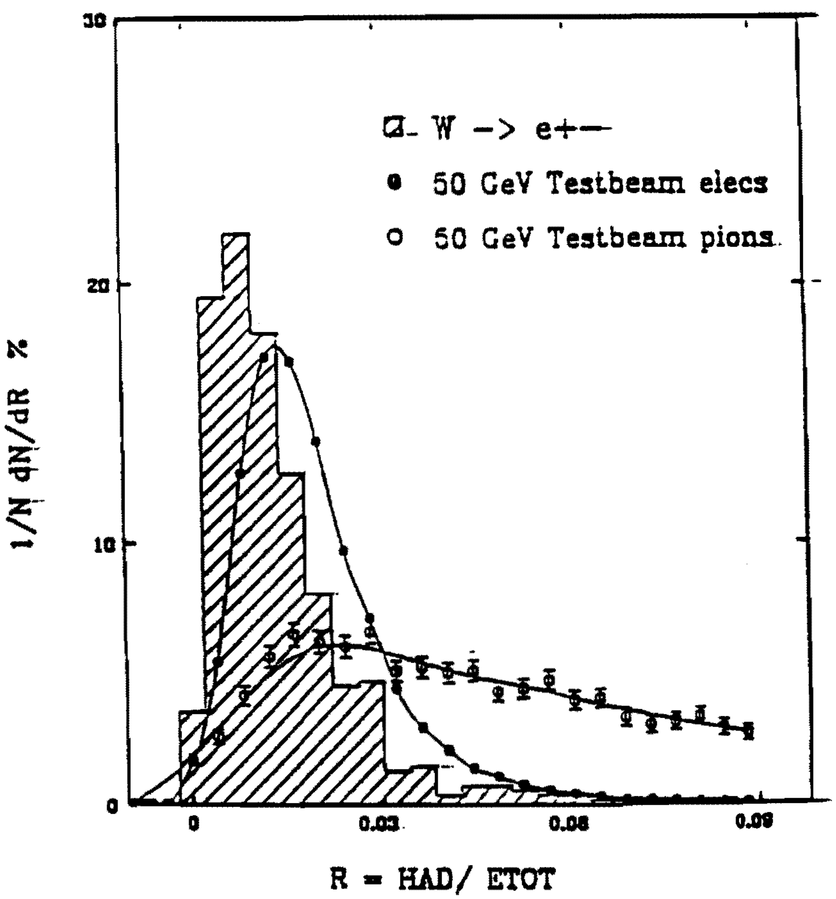

Figure 4.2: The $Had/(Had + EM)$ distribution for 50 GeV testbeam electrons and charged pions, and for electrons from W decays. From [Pro89a].

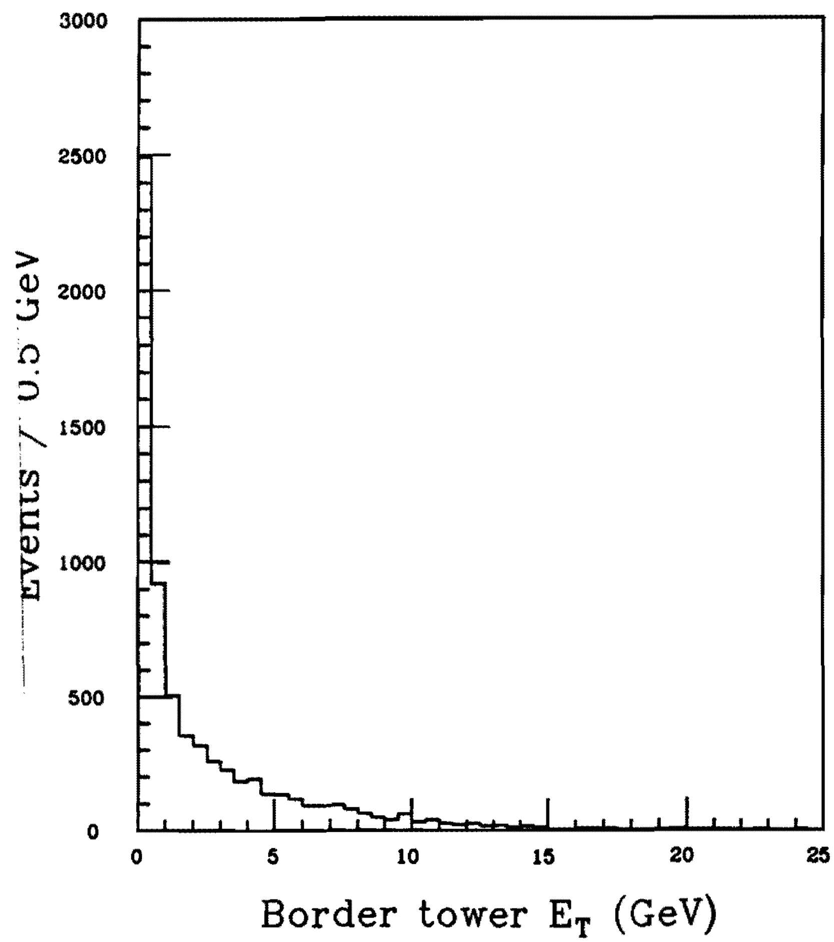

Figure 4.3: Border tower transverse energy distribution for electrons passing the identification cuts listed in section 4.1.4.

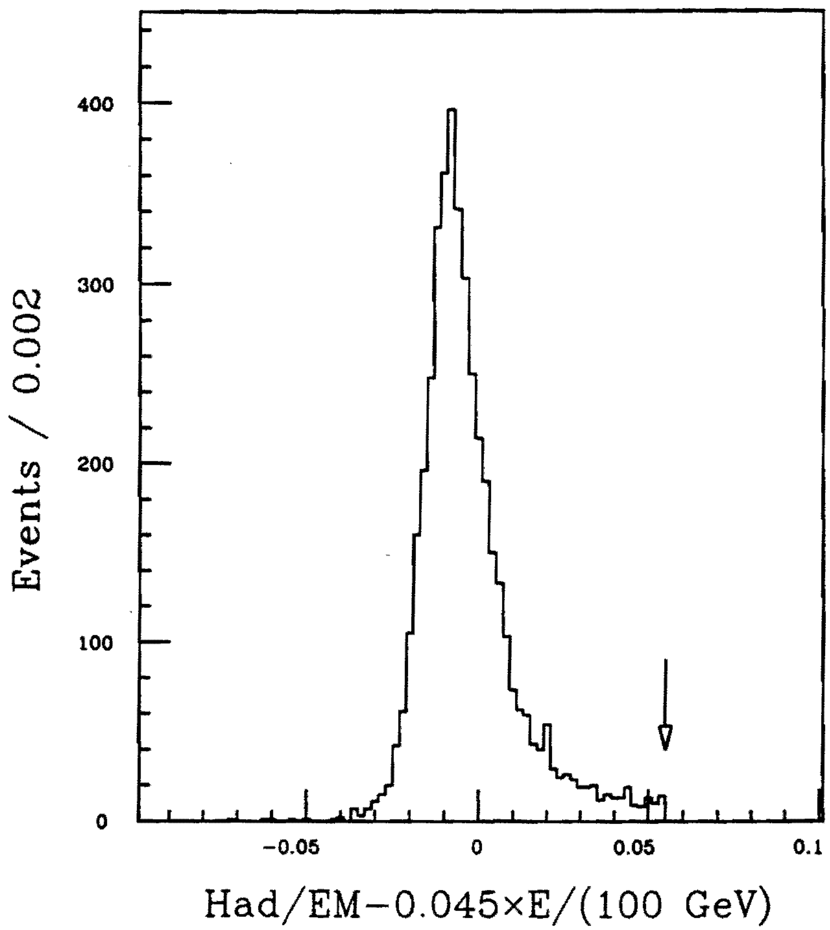

Figure 4.4: Distribution of the quantity $Had/EM - 0.045 \times E/(100\,\mathrm{GeV})$ for isolated electrons passing the identification cuts listed in section 4.1.4.

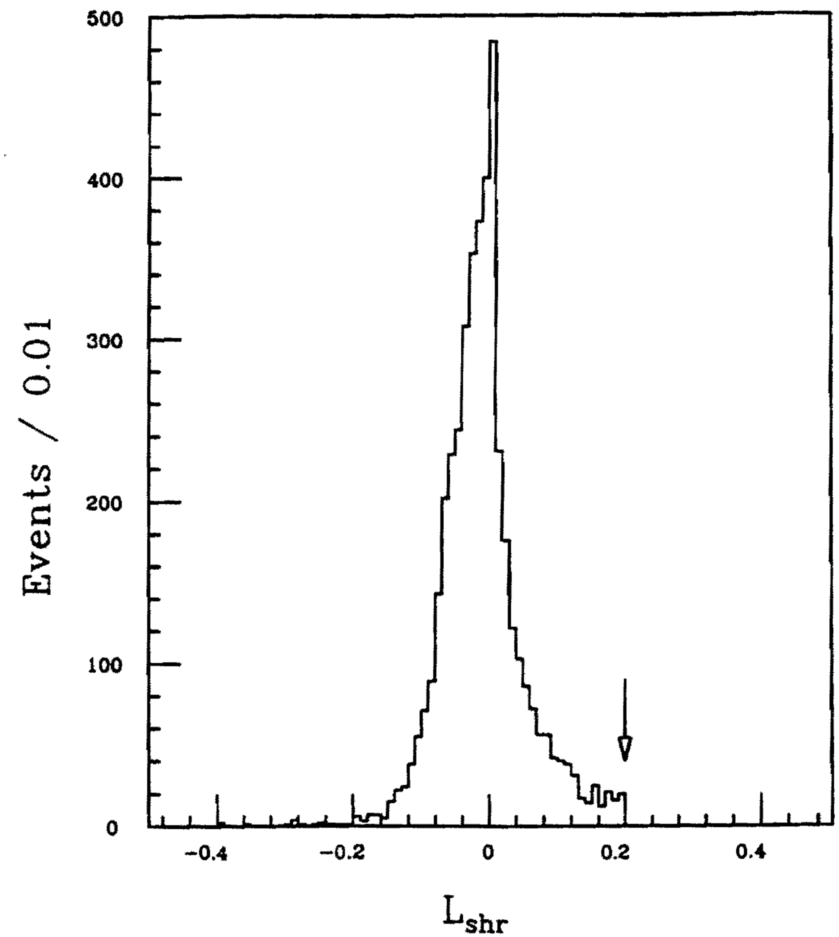

Figure 4.5: Distribution of L_{shr} for isolated central electrons passing the identification cuts listed in section 4.1.4.

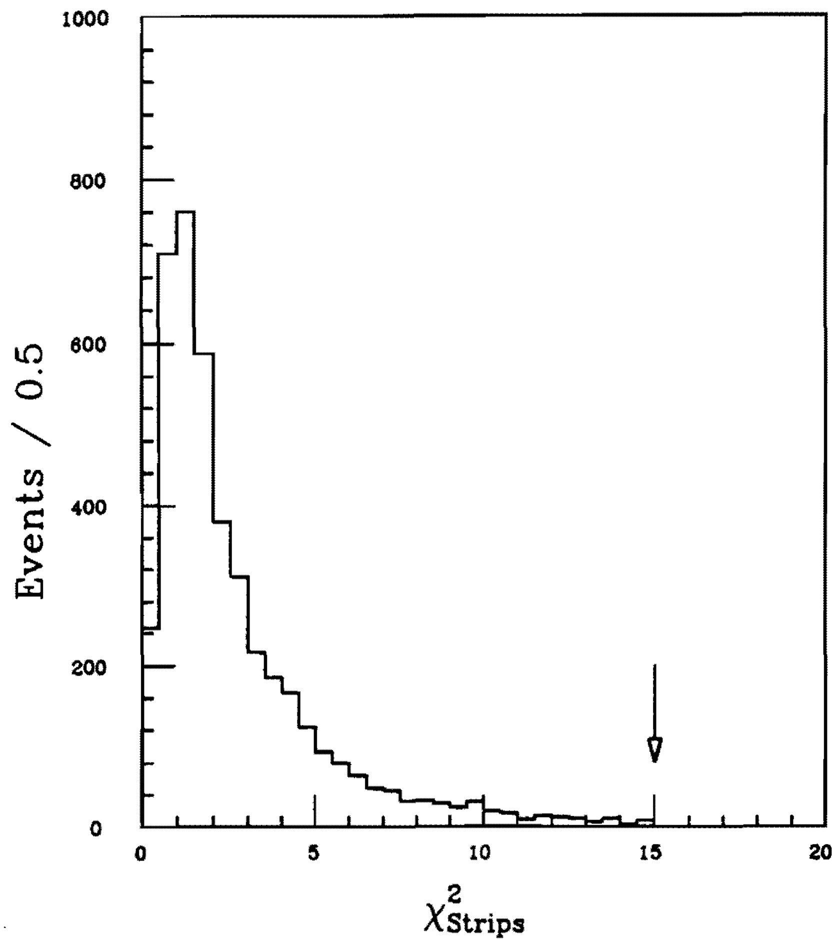

Figure 4.6: Distribution of χ^2_{Strips} for isolated electrons passing the identification cuts listed in section 4.1.4.

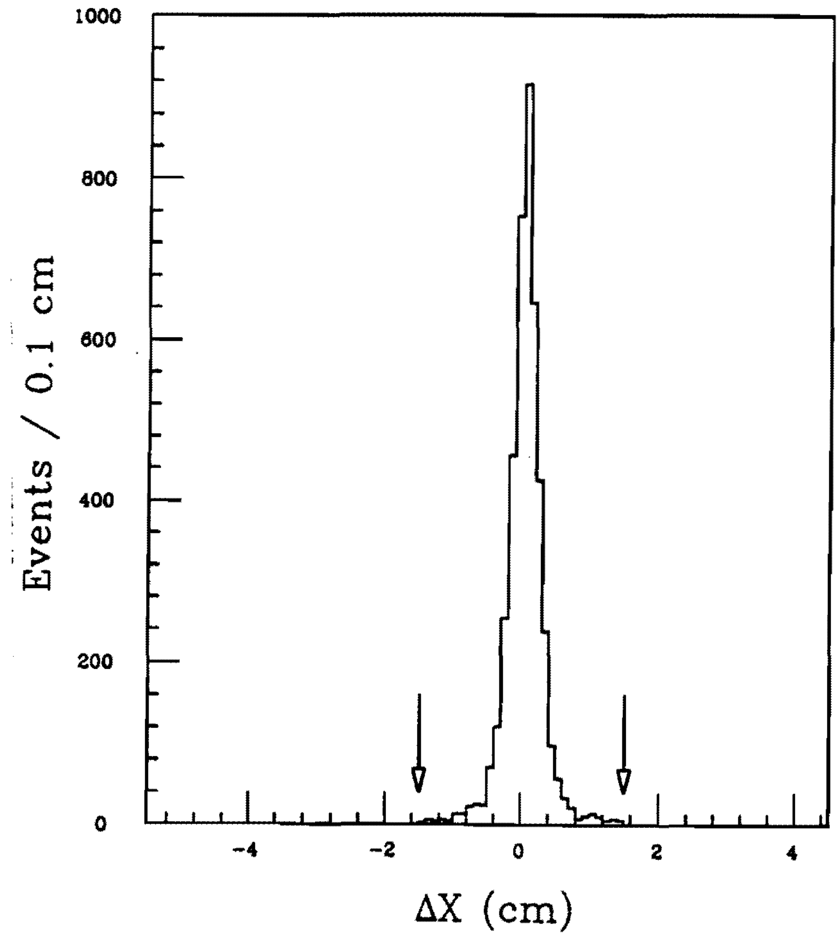

Figure 4.7: Distribution of ΔX for isolated electrons passing the identification cuts listed in section 4.1.4.

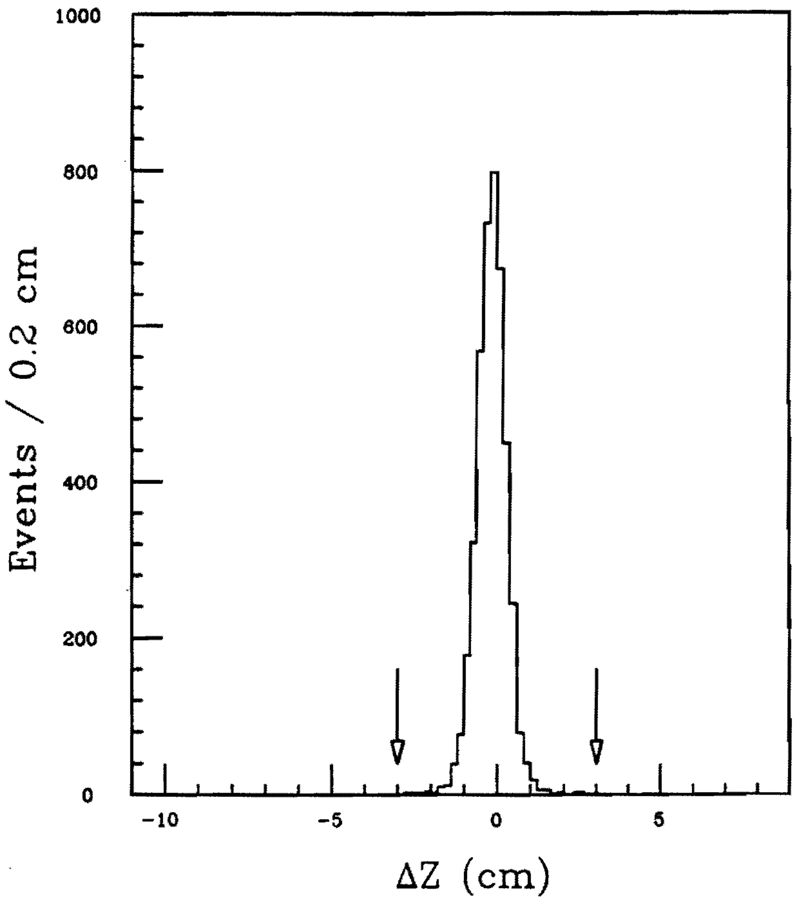

Figure 4.8: Distribution of ΔZ for isolated electrons passing the identification cuts listed in section 4.1.4.

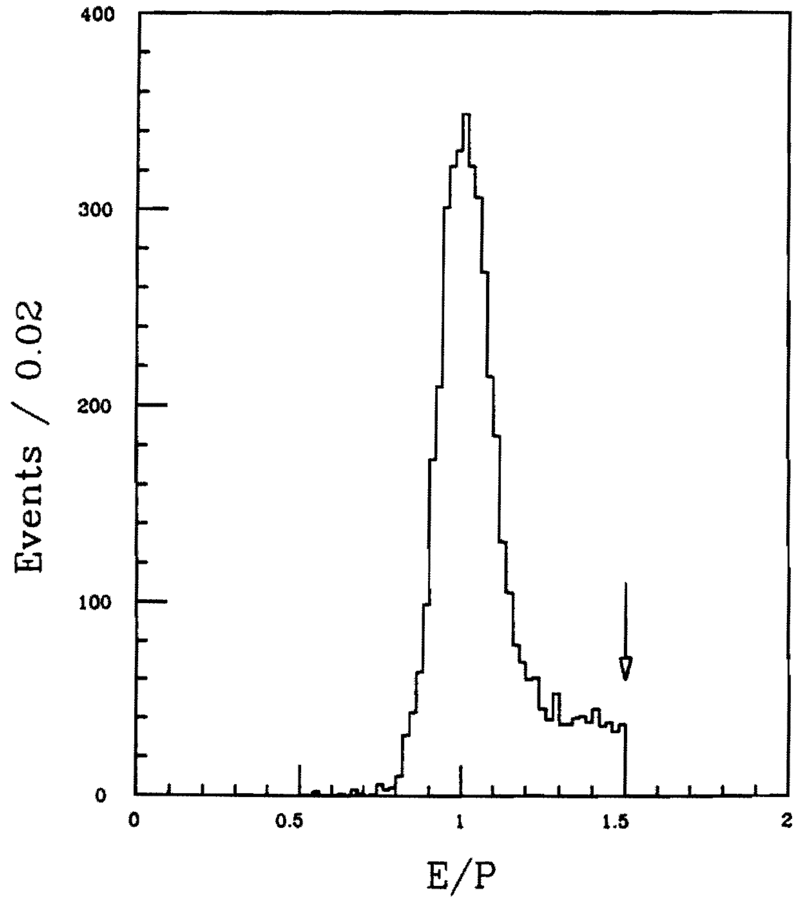

Figure 4.9: Distribution of E/p for isolated electrons passing the identification cuts listed in section 4.1.4.

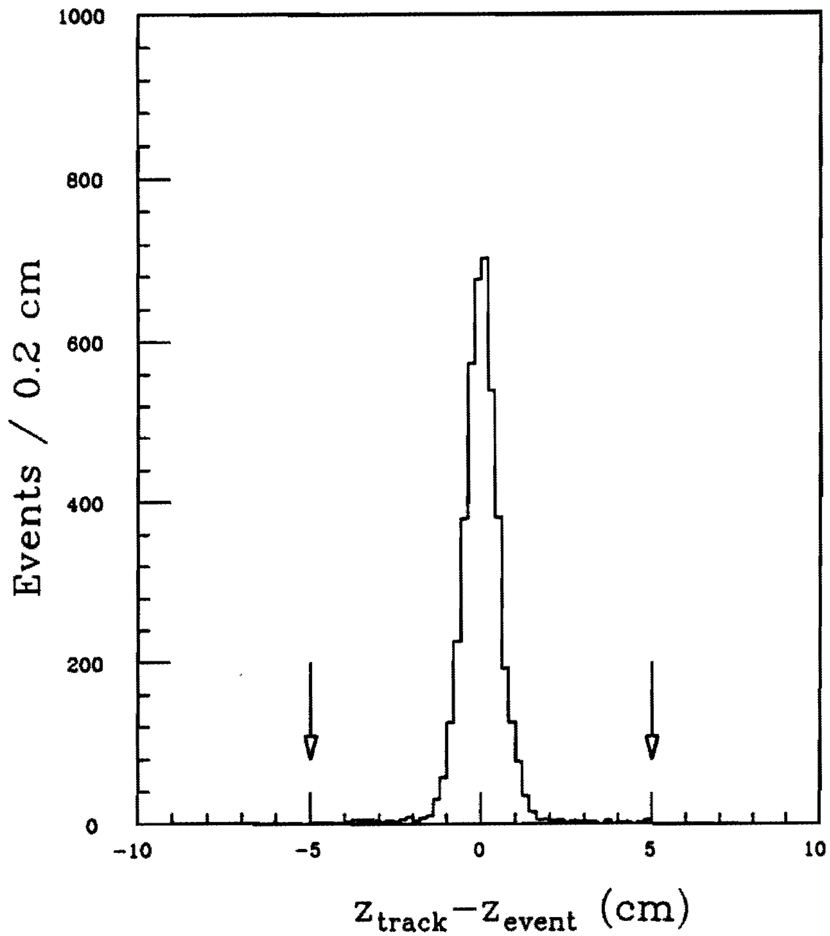

Figure 4.10: Distribution of the track offset in z for isolated electrons passing the identification cuts listed in section 4.1.4.

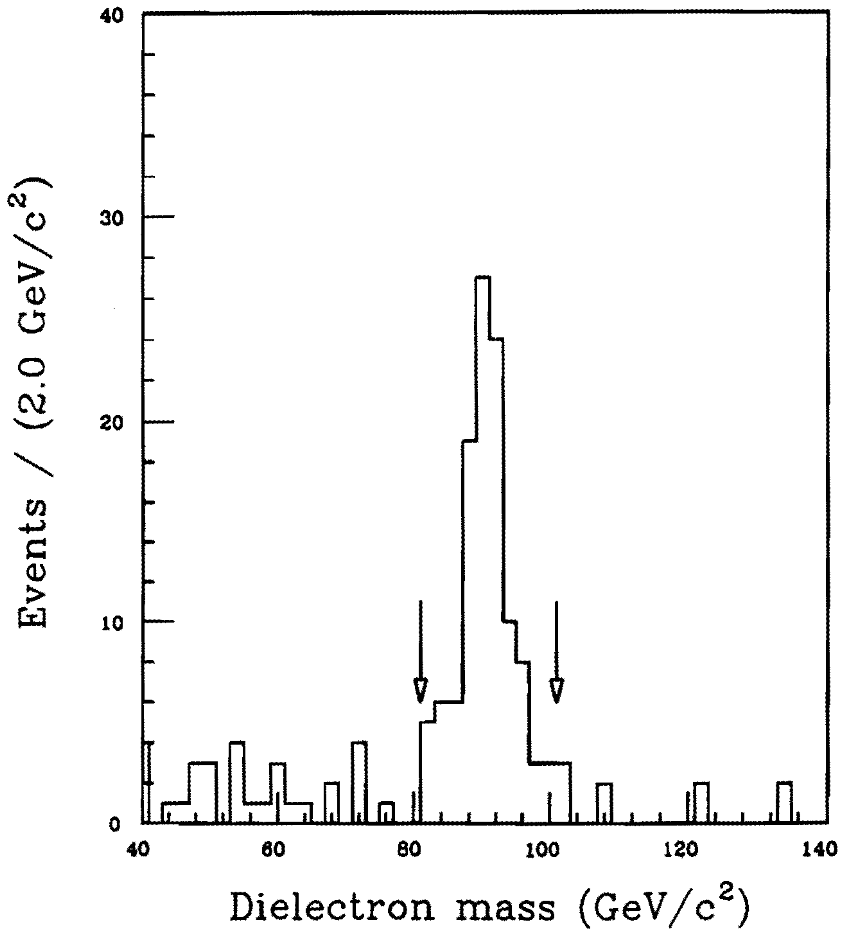

Figure 4.11: Dielectron invariant mass distribution; events with 81 GeV/c^2 $< m_{ee} <$ 101 GeV/c^2 are used in the electron identification efficiency calculation.

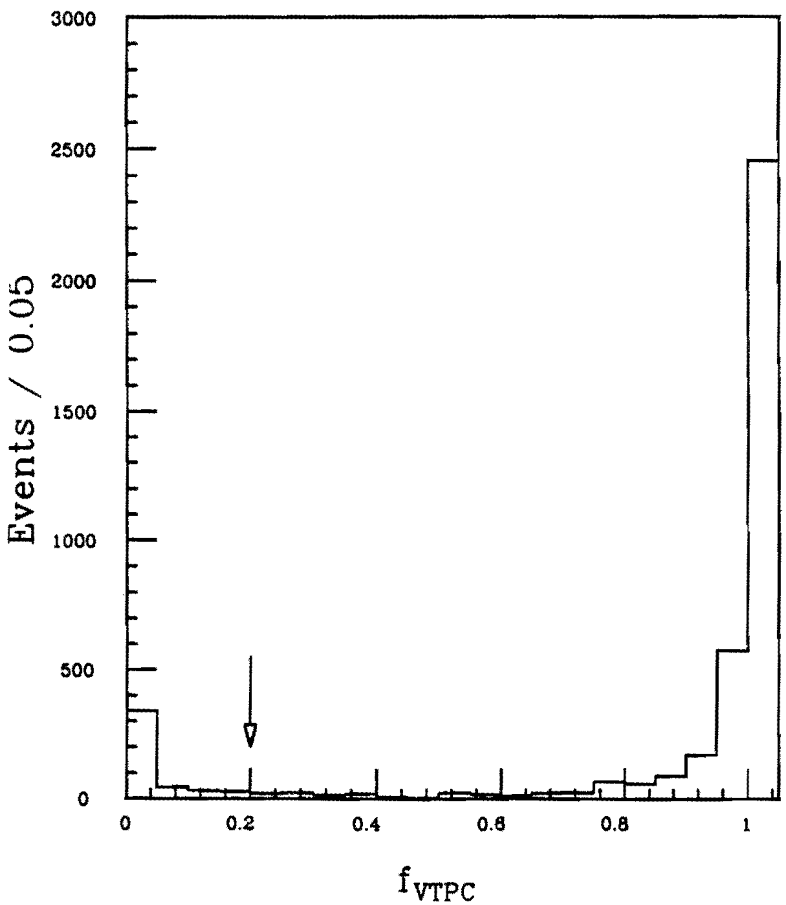

Figure 4.12: Fraction of expected hits observed in the VTPC along an electron's trajectory. Events falling to the left of the arrow are rejected by the conversion filter.

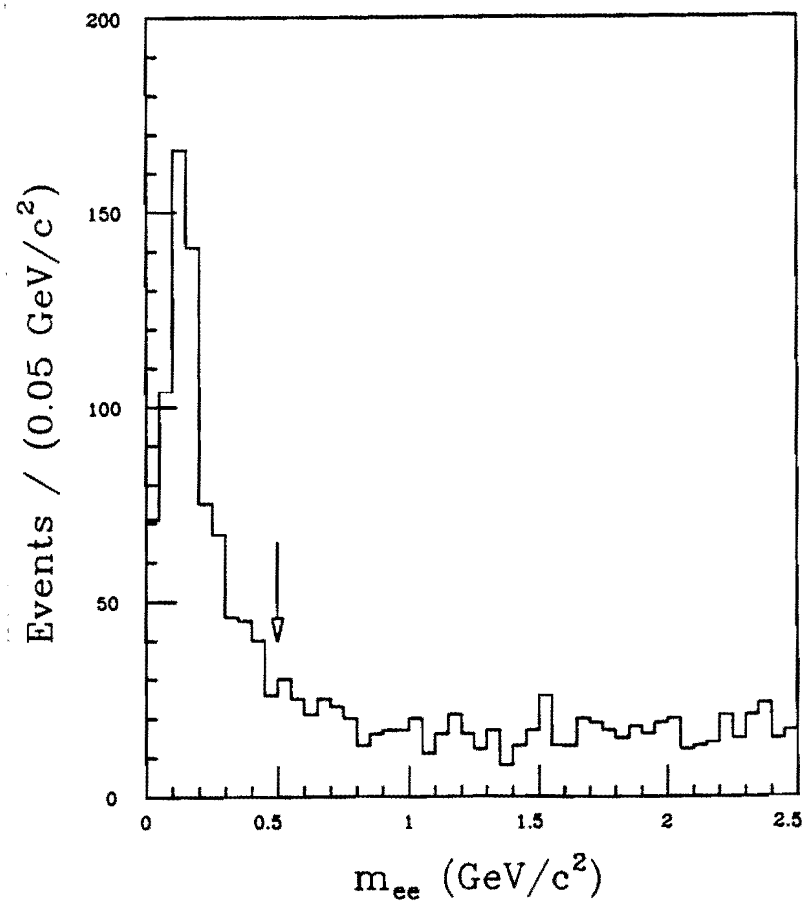

Figure 4.13: Invariant mass of electrons with a nearby track. Events falling to the left of the arrow are rejected by the conversion filter.

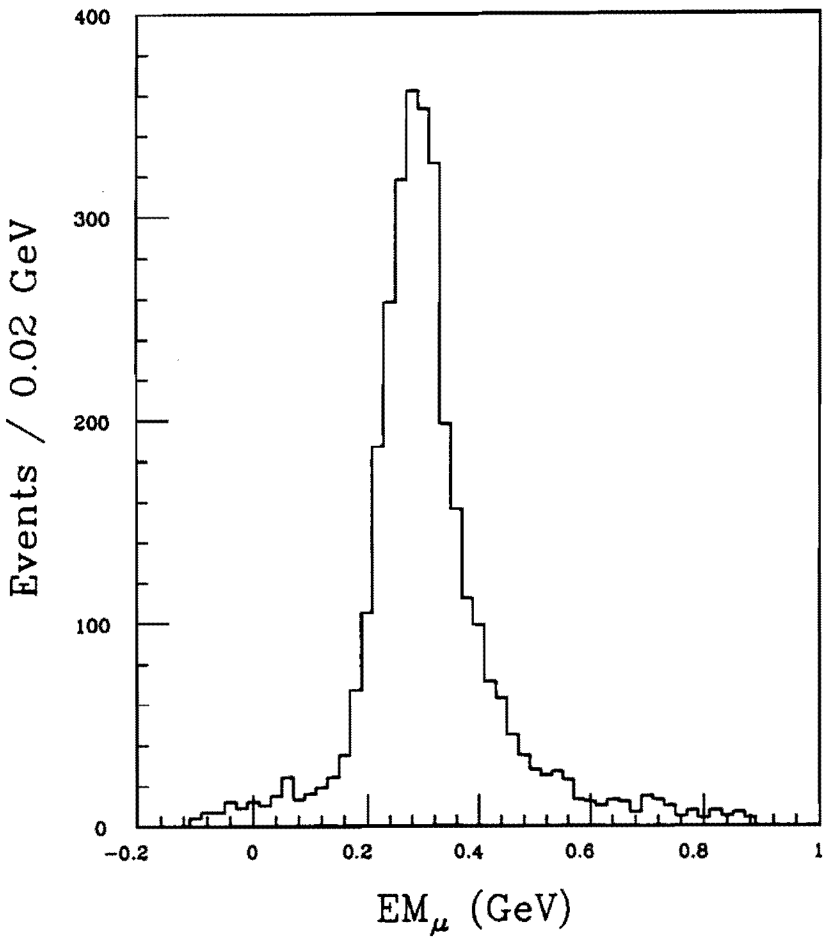

Figure 4.14: Energy deposited in the CEM by 57 GeV testbeam muons. From [Wes89].

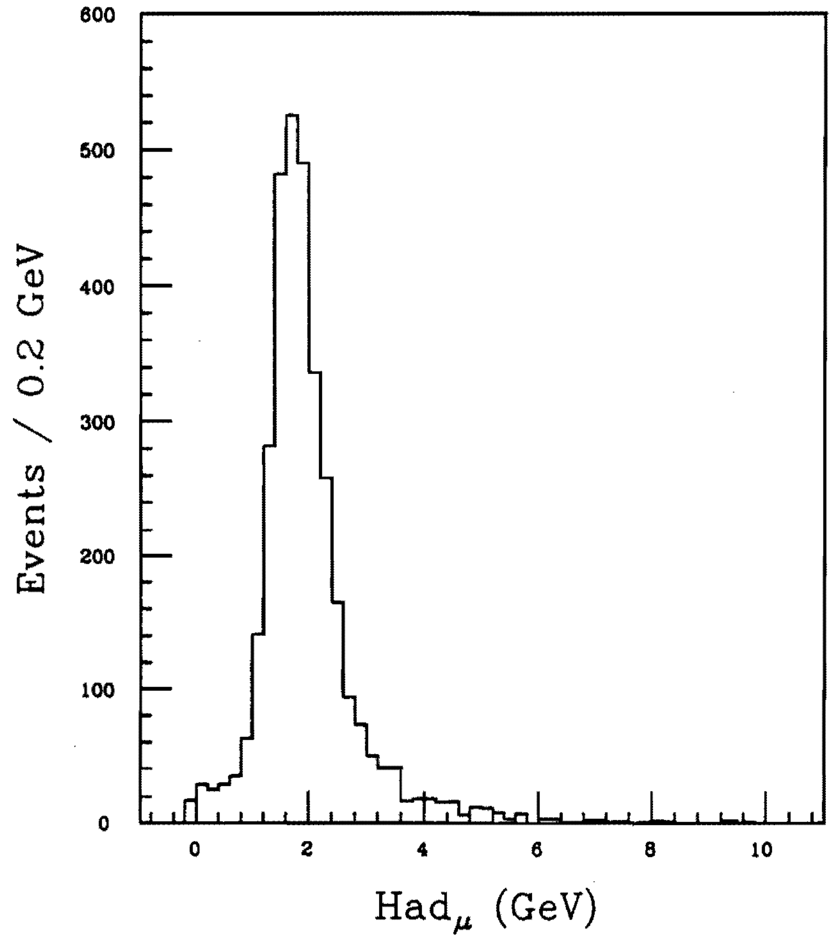

Figure 4.15: Energy deposited in the CHA by 57 GeV testbeam muor From [Wes89].

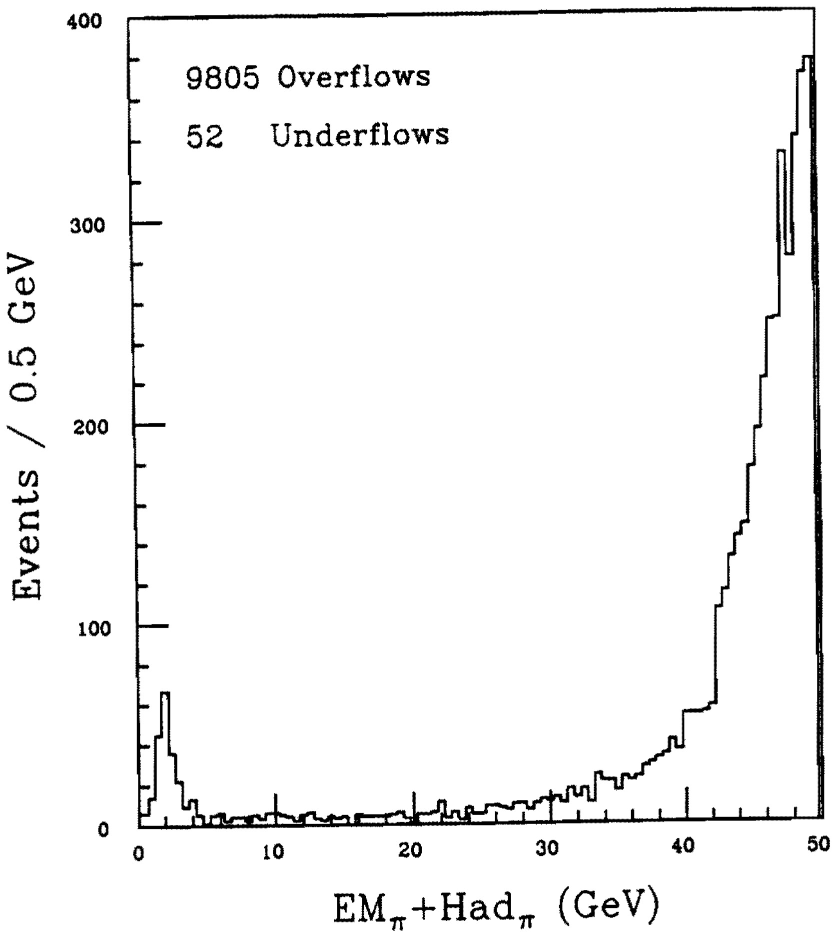

Figure 4.16: Energy deposited by 57 GeV testbeam pions in the combined CEM+CHA. The peak at small energy is due to non-interacting pions and untagged muons. From [Smi89].

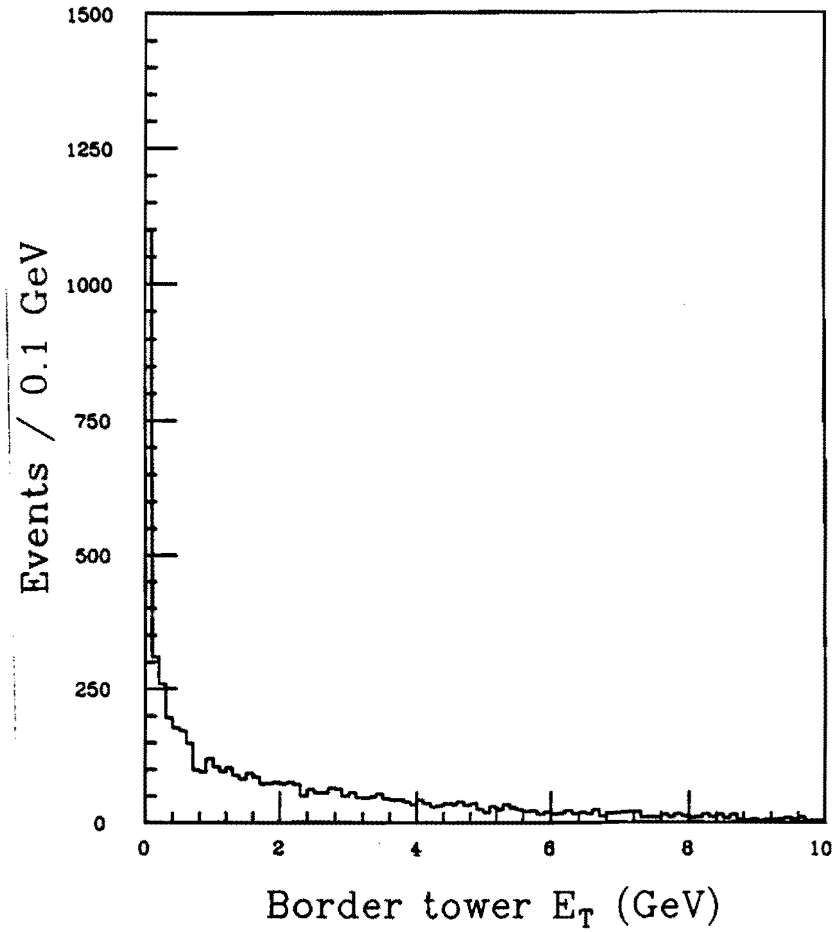

Figure 4.17: Border tower transverse energy distribution for muons passing the identification cuts listed in section 4.2.3.

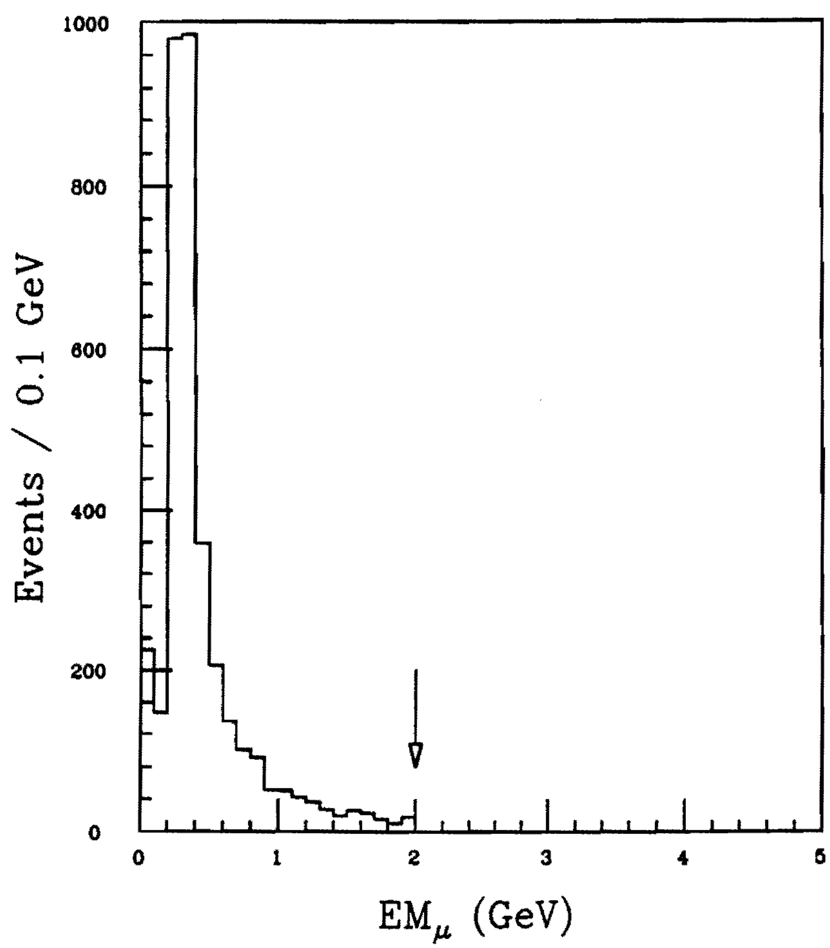

Figure 4.18: Distribution of the energy deposited in the CEM by isolated central muons passing the identification cuts listed in section 4.2.3.

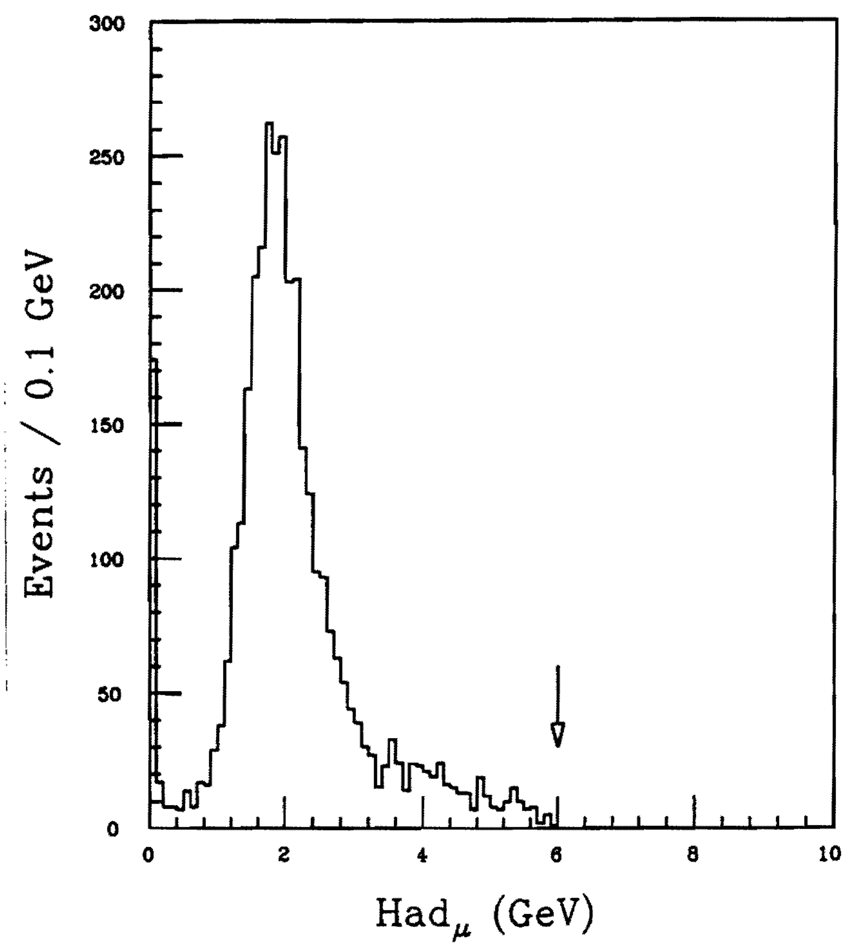

Figure 4.19: Distribution of the energy deposited in the CHA by isolated centr muons passing the identification cuts listed in section 4.2.3.

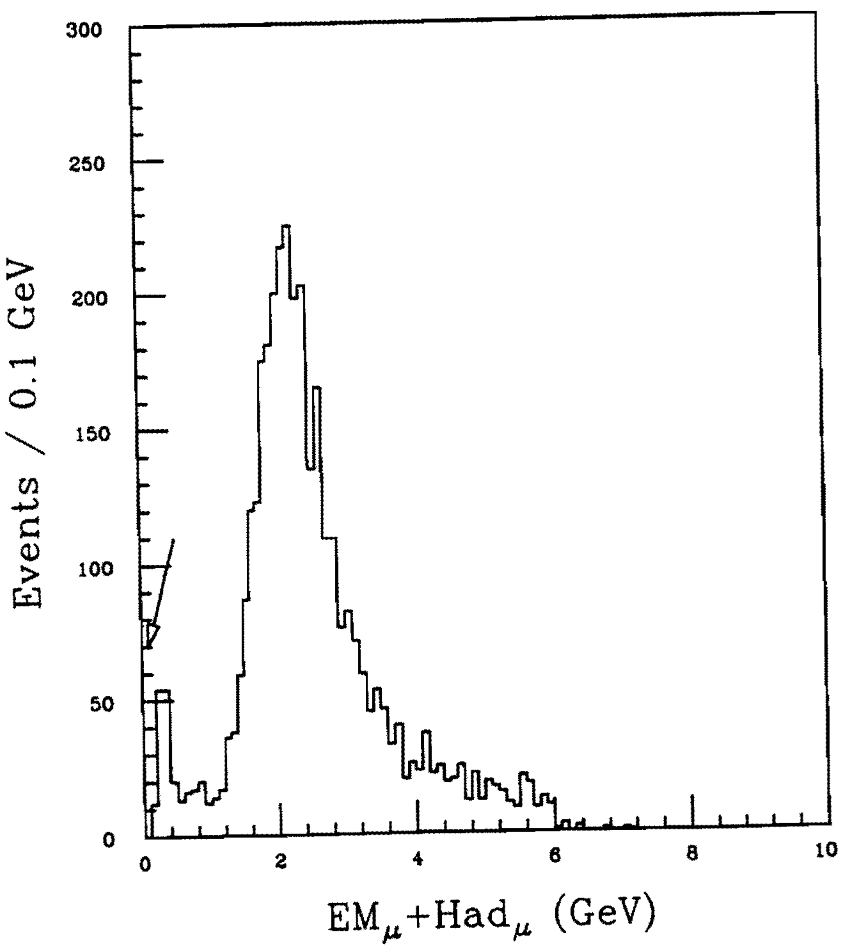

Figure 4.20: Distribution of the total CEM+CHA energy deposited by isolated central muons passing the identification cuts listed in section 4.2.3.

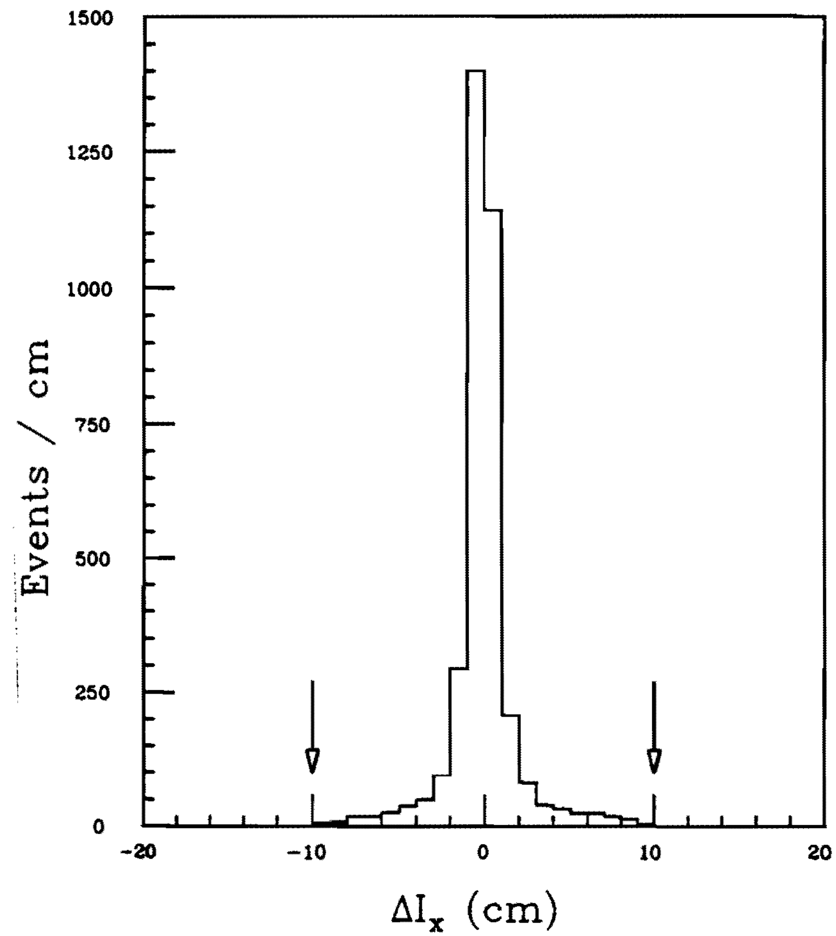

Figure 4.21: Distribution of the difference in intercept, in the local wedge x–y plane, between the CMU stub and the extrapolated CTC track, for isolated central muons passing the identification cuts listed in section 4.2.3.

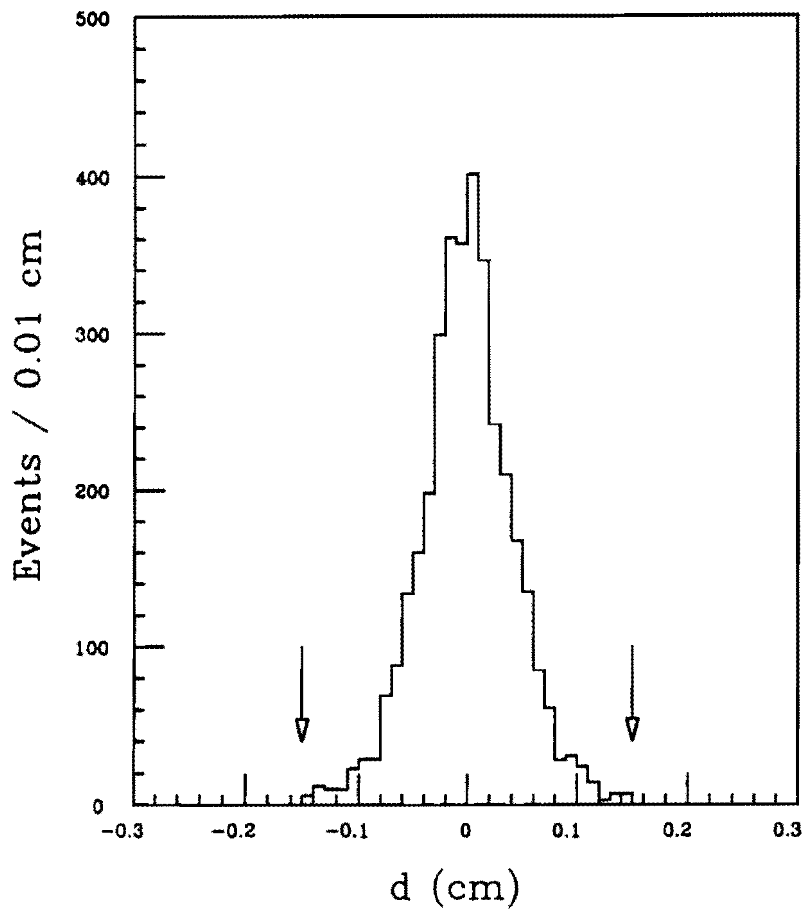

Figure 4.22: Distribution of the track impact parameter for isolated central muons passing the identification cuts listed in section 4.2.3.

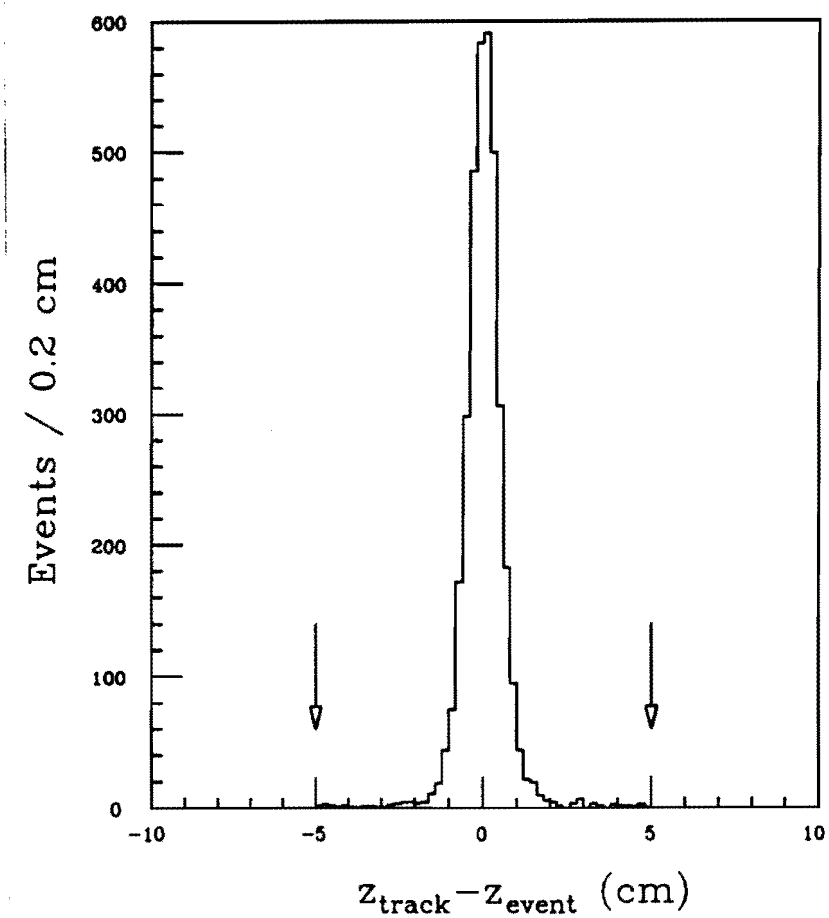

Figure 4.23: Distribution of the track z-coordinate offset for isolated central muons passing the identification cuts listed in section 4.2.3.

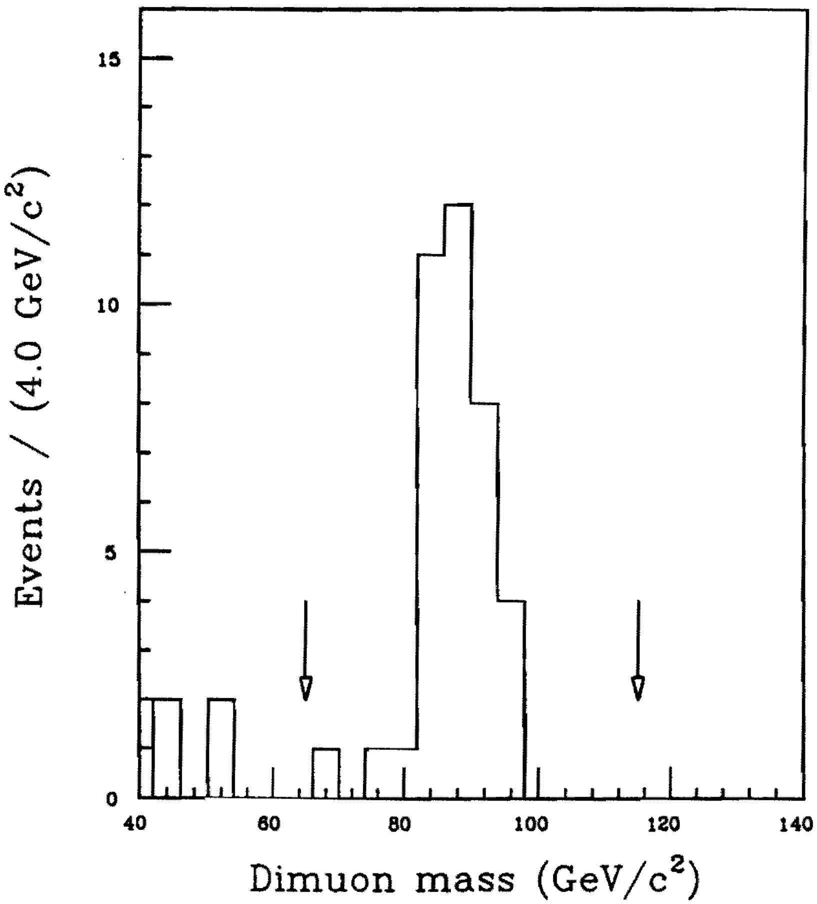

Figure 4.24: Dimuon invariant mass distribution; events with $65\,\mathrm{GeV}/c^2 < m_{\mu\mu} < 115\,\mathrm{GeV}/c^2$ are used in the muon identification efficiency calculation.

Chapter 5

Monte Carlo Data Sets

We describe the Monte Carlo event samples to which later chapters will refer for defining a $t\bar{t}$ signal region and for studying its W+dijet background. All the generated events were subjected to a realistic detector simulation and subsequently reconstructed through the same chain of algorithms that is executed on real $p\bar{p}$ collisions.

5.1 Generation of $t\bar{t}$ samples

We used the Monte Carlo ISAJET [Pai86] to generate samples of $p\bar{p} \to t\bar{t} + X$ events. The main features of this generator are discussed in the section below, after which the datasets themselves will be described.

5.1.1 The ISAJET program

ISAJET produces $t\bar{t}$ events in four separate steps. First, the parton level hard scattering is generated according to the leading order perturbative QCD two-jet cross section, convoluted with structure functions evolved to some appropriate momentum scale Q^2. To generate events efficiently, ISAJET starts a run by constructing an envelope for the two-jet differential cross section:

$$\frac{d\sigma}{dp_T^2\, d\eta_1\, d\eta_2} < F(p_T) \stackrel{\mathrm{def}}{=} A\, p_T^{-b} \tag{5.1}$$

where p_T is the transverse momentum of either jet, and η_1, η_2 are the jet pseudo-rapidities. For each event, the jet transverse momentum is generated according to $F(p_T)$. The event is then accepted if its QCD cross section is larger than a uniform random number times $F(p_T)$. This produces unweighted events.

In the second step, initial and final state partons are developed into parton cascades according to the branching approximation algorithm due to Fox and Wolfram [Fox80]. The application of this algorithm to the initial state requires some care, for which the Sjöstrand approach was chosen [Sjo85]. Thus, scaling violations in jet fragmentation are implemented, inducing jet broadening, and additional, resolvable jets may appear. The matrix element for widely separated jets however, is only approximately reproduced by this method.

Final state partons are subsequently hadronized according to the Field and Feynman independent jet fragmentation ansatz. This is the third step in the ISAJET program. Independent fragmentation correctly describes the fast hadrons in a jet, but it does not conserve energy-momentum, nor flavor. In ISAJET, energy-momentum conservation is enforced by boosting all hadrons to the rest frame of the fragmented jets, rescaling the three-momenta by a common factor, and recalculating the energies. Heavy quarks (charm, bottom and top) are fragmented according to the Peterson model, where the ϵ_Q parameter (see equation 1.20) is set to 0.8 GeV^2/m_Q^2 in the case of charm, and 0.5 GeV^2/m_Q^2 otherwise.

The final event generation step in ISAJET is the addition of beam jets, which result from spectator parton interactions. Here, ISAJET uses a simplified version of a scheme proposed by Abramovskii, Kancheli, and Gribov [Abr72] to describe minimum bias data. This scheme is modified to account for the experimental observation that spectators interact more strongly in hard scattering events.

5.1.2 ISAJET data sets

ISAJET version 6.25 was run to generate $t\bar{t}$ events for top masses of 60, 70 and 80 GeV/c². Only final states where one of the top quarks decays semileptonically into an electron or a muon, whereas its partner decays hadronically, were retained. The EHLQ1 structure functions were used, and the QCD scale was set to:

$$Q^2 = \frac{2\,\hat{s}\,\hat{t}\,\hat{u}}{\hat{s}^2 + \hat{t}^2 + \hat{u}^2} \tag{5.2}$$

where $\hat{s}$, $\hat{t}$ and $\hat{u}$ are the standard Mandelstam invariants for the parton-parton scattering. The transverse momentum of the top quarks was constrained between 6 and 200 GeV/c.

The integrated luminosities of the $t\bar{t}$ samples are 44, 97 and 193 pb^{-1} for $m_{top} = 60$, 70 and 80 GeV/c² respectively, in both the electron + jets and the muon + jets channels. These samples were normalized to the theoretical cross section calculation described in chapter 1, rather than to ISAJET's estimate. A summary is provided in table 5.1.

m_{top} (GeV/c²)	$\sigma_{t\bar{t}}$ (pb)	$\int \mathcal{L}\,dt$ (pb^{-1})
60	1260	44
70	569	97
80	285	193

Table 5.1: ISAJET $t\bar{t}$ samples. For each top mass, the production cross section from [Ell91], and the integrated luminosity of the corresponding Monte Carlo sample are indicated.

5.2 Generation of W+dijet samples

ISAJET does not properly simulate the process $p\bar{p} \rightarrow W + 2\,\mathrm{jets}$ when the jets are emitted at wide angles. We used the PAPAGENO [Hin89a] Monte Carlo instead. As in the previous section, we start with a short overview of the generator program, and present the data sets afterwards.

5.2.1 The PAPAGENO program

PAPAGENO is a parton level Monte Carlo which uses exact tree-level matrix elements for the processes it simulates. For events containing a W accompanied by one or more partons, it uses a computation by Hagiwara and Zeppenfeld [Hag89]. Since loop diagrams are not included in the calculation of the matrix elements, divergences arising from soft and collinear partons in next-to-leading order tree diagrams are not cancelled, and some regulating cuts must be introduced. Leaving out loop diagrams also affects the overall normalization of the cross section at a given order in the coupling constant α_S. This can be compensated for by renormalizing α_S, which hereby becomes dependent on a momentum scale Q^2. The resulting uncertainty on the cross section normalization is about 50% [Hin89b]. The shape of the physical distributions however, should not be affected by this neglect of loop diagrams, provided the regulating cuts are chosen so as to be hidden by the experimental resolution on the transverse momentum and mutual separation of the jets. We emphasize that PAPAGENO only produces exclusive final states with a W and a fixed number of partons.

In PAPAGENO, the decaying of the W is an optional feature with some limitations. When this feature is enabled, only one sign of W charge is produced, and the W decays with a 100% branching fraction into the selected channel. Hence, the predicted event rates must be multiplied by a factor of 2/9 (if the $W \to tb$ mode is inhibited, which we shall assume throughout this work). For events with a W and two jets, PAPAGENO decays the W according to a $(1+\cos^2\theta)$ distribution, rather than the correct $(1\pm\cos\theta)^2$ form, but, because of the transverse motion of the W, the difference is too small to be noticeable.

In the CDF implementation of PAPAGENO, final state partons are hadronized using ISAJET routines. When the process involves a vector boson in the final state, the subsequent global momentum rescaling is done differently than in ISAJET, in order to leave the boson momentum unaffected. In each final state jet separately, the particle three-momenta are rescaled so that the magnitude of the total jet three-momentum equals that of the parent parton. This procedure violates conservation of $\hat{s}$, the invariant mass of the initial state parton system, but this is a much smaller effect than that of modifying the boson momentum. Jet broadening, the effect of scaling violations in jet fragmentation, is not simulated.

Finally, an underlying event is added by calling the appropriate ISAJET routines.

PAPAGENO uses the VEGAS algorithm [Lep78,Lep80] to calculate a hadronic

cross section σ as the convolution integral of the partonic cross section $\hat{\sigma}$ with structure functions F_a, F_b:

$$\sigma(p\bar{p}\to Wjj) = \int dx_1\, dx_2 \sum_{a,b} F_a(x_1,Q^2)\, F_b(x_2,Q^2)\, \hat{\sigma}(ab\to Wjj) \tag{5.3}$$

An initial run, during which no events are output, serves to sample the integrand and create a grid of function values to be used as probability density $p(x)$ for subsequent iterations. The integral is then evaluated as a sum over M configurations (x) of initial and final state momenta, distributed according to the density $p(x)$:

$$\int f(x)\, dx \;\to\; \frac{1}{M}\sum_{(x)} \frac{f(x)}{p(x)} \tag{5.4}$$

This produces events with weights $f(x)/[M\,p(x)]$. Since these events must still be processed through a lengthy detector simulation program, it is more efficient to work with unweighted events. This is realized as follows. A maximum on the set of event weights is obtained during PAPAGENO's initial, outputless run, and is saved for the next run. An event is then retained only if its weight is greater than a uniform random number times the maximum.

5.2.2 PAPAGENO data sets

We used PAPAGENO version 3.12, with the EHLQ1 structure functions and a QCD coupling constant evaluated at the scale:

$$Q = \frac{1}{2N}\sum_{i=1}^{N}\sqrt{p_{Ti}^2 + m_i^2} \tag{5.5}$$

where N is the number of primary particles in the final state, and p_{Ti}, m_i their transverse momenta and masses; $N = 3$ for the process $p\bar{p}\to W + 2\,\text{jets}$. To avoid divergences in the matrix elements, we required the transverse momentum of each jet to be greater than 7 GeV, and the (η,ϕ) separation between jets to be at least 0.4. An additional cut on the jet pseudo-rapidity, $|\eta_{\text{jet}}| < 3.5$, was imposed to reduce event generation in regions of phase space that are irrelevant to subsequent analysis.

The same set of PAPAGENO events was used to obtain final states where the W decays into the electron channel, and final states where the W decays into the muon channel. The integrated luminosity of both samples is 35 pb^{-1}, according to the PAPAGENO calculation for the cross section.

5.3 Detector simulation

All the Monte Carlo data sets were passed through a full detector simulation program [Fre87]. We now discuss various aspects of the simulated detector response.

5.3.1 Jet energy scale and detection efficiency

The energy scale of the central calorimeter has been determined with testbeams of pions having energies between 15 and 150 GeV, and electrons with energies between 10 and 50 GeV [Abe91a]. The calorimeter response to low energy pions (0.5 to 10 GeV) was obtained from an analysis of isolated tracks in the CTC in minimum bias events. This analysis consisted in comparing the transverse momentum of such tracks with the energy collected in the calorimeter, after including a correction for the energy of neutral particles. The response attenuation due to uninstrumented spaces between calorimeter modules is also incorporated in the simulation.

Several checks of the simulated jet energy response were done. One of them started from a selection of events with an isolated direct photon recoiling against a single jet. The photon was detected as an electromagnetic cluster with no associated track and satisfying a tight χ^2_{Strips} requirement to reject photons from π^0 decay. No clusters with $E_T > 3$ GeV were allowed in the photon hemisphere. Hence the transverse momentum of the photon balanced that of the parton in the opposite hemisphere. This was used to verify the jet energy scale. Figure 5.1 shows the probability of detecting a jet with $E_T > 10$ GeV recoiling against a photon in direct photon events. This plot assumes equality of the parton and photon transverse momenta. The curve is a Monte Carlo prediction. The agreement indicates that the modeling of the detector response in the simulation program

is correct within a few percent. Other studies have compared the jet transverse energy spectrum in the inclusive electron sample with that of a Monte Carlo sample of $b\bar{b}$ and $c\bar{c}$ events. A conservative estimate of the uncertainty on the Monte Carlo jet energy scale is 20% for a jet with 10 GeV of transverse energy.

5.3.2 Electron identification efficiency

We measured the Monte Carlo electron identification efficiency from our sample of PAPAGENO W+dijet events, where the W decays in the electron channel. Events are selected by requiring that the electron pass all the fiducial cuts (section 4.1.5), have $E_T > 20$ GeV, and Iso(0.7) < 12 GeV. The efficiency of a cut is then simply the fraction of those electrons which pass the cut. Results are shown in table 5.2. The Monte Carlo efficiencies agree reasonably well with those measured from real

Cut	N_c	ϵ_c
$Had/EM < 0.055 + 0.045 \times E/(100\text{ GeV})$	4327	.997 $\pm$ .001
$L_{shr} < 0.2$	4120	.949 $\pm$ .003
$\chi^2_{Strips} < 15$	4142	.954 $\pm$ .003
$\|\Delta X\| < 1.5$ cm	4134	.953 $\pm$ .003
$\|\Delta Z\| < 3.0$ cm	4161	.959 $\pm$ .003
$E/p < 1.5$	4106	.946 $\pm$ .003
Track quality	4224	.973 $\pm$ .002
All Cuts	3678	.847 $\pm$ .005

Table 5.2: Electron selection cuts and their efficiencies as calculated from 4340 $W \to e\nu$ Monte Carlo events.

data (cfr table 4.1). It should be noted that these numbers are not sensitive to the values of the isolation and E_T cuts. For example, an isolation cut of Iso(0.7) < 3 GeV gives a total Monte Carlo efficiency of 0.849 ± 0.007, whereas no isolation cut at all reduces the total efficiency to 0.842 ± 0.005. Similarly, by varying the E_T threshold from 10 to 30 GeV, the total efficiency changes only from 0.840 ± 0.005 to 0.849 ± 0.006.

5.3.3 Muon identification efficiency

The efficiency of the muon identification cuts in the simulated detector is determined from our sample of PAPAGENO W+dijet events, with the W decaying in the muon channel. Muons used for this purpose are required to penetrate the fiducial region described in section 4.2.4, to have a transverse momentum above 20 GeV/c, and to pass the isolation cut Iso(0.4) < 5 GeV. The efficiencies are listed in table 5.3. The Monte Carlo muon efficiencies are consistent with real

Cut	N_c	ϵ_c
$EM_\mu < 2$ GeV	2268	0.989 ± .002
$Had_\mu < 6$ GeV	2248	0.980 ± .003
$EM_\mu + Had_\mu > 0.1$ GeV	2293	1.000 ± .000
$\|\Delta I_z\| < 10$ cm	2293	1.000 ± .000
$\|z_{track} - z_{event}\| < 5$ cm	2280	0.994 ± .002
$d < 0.15$ cm	2292	1.000 ± .000
All Cuts	2216	0.966 ± .004

Table 5.3: Muon selection cuts and their efficiencies as calculated from 2293 $W \rightarrow \mu\nu$ Monte Carlo events.

data (table 4.3), and are not sensitive to the exact values of the isolation and p_T cuts.

5.3.4 Monte Carlo acceptance corrections

Our Monte Carlo electron samples are normalized to the integrated luminosity of the CDF inclusive electron sample, which is (4.05 ± 0.28) pb^{-1}. Three corrections are independently applied to this normalization. The first one is the trigger efficiency, estimated to be $(98.0 \pm 0.5)\%$ (section 4.1.1). We do not apply the conversion filter (section 4.1.7) to our Monte Carlo data. Hence the Monte Carlo rates must be adjusted to take into account the overefficiency of this filter ($f_{prompt} = 0.027 \pm 0.003$). Finally, we also correct for the small discrepancy between the electron identification efficiency in the detector simulation program and in the real data. This contributes a factor of (1.044 ± 0.029).

The CDF inclusive muon sample has an integrated luminosity of (3.54 ± 0.24) pb^{-1}. The inefficiency of the combined level 1 and level 2 central muon trigger (section 4.2.1) contributes a correction factor of $(90 \pm 2)\%$. In addition, we compensate for the fraction of prompt muons rejected by the cosmic ray filter with a factor of 0.998 (section 4.2.5), and for the mismatch in muon identification probability between data and Monte Carlo, which gives a ratio of (0.993 ± 0.025).

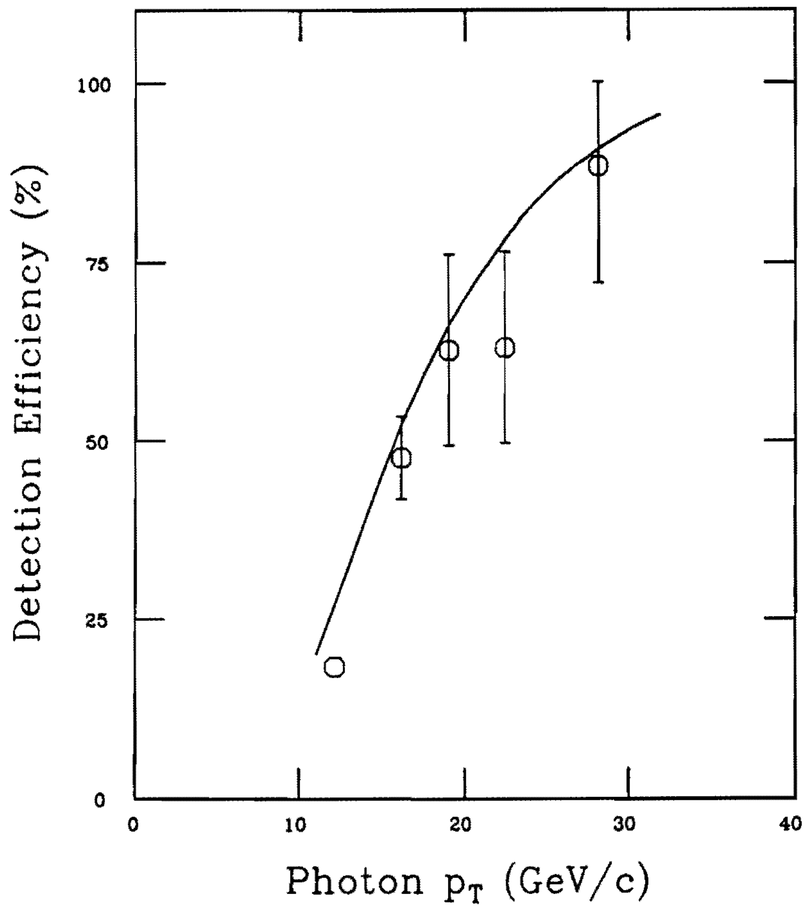

Figure 5.1: Probability of detecting a jet with $E_T > 10$ GeV opposite a prompt photon. The curve is a Monte Carlo prediction. From [Abe91a]

Chapter 6

Final Event Samples

The signal region for the process $p\bar{p} \to t\bar{t} + X \to l\nu_l jj + X$, where j stands for a jet and l for a lepton, is defined. Two independent final event samples are thus generated, one with a high p_T electron tag, and one with a high p_T muon tag. These samples are expected to be enriched in top decays, but, as shown in section 6.2, they consist mainly of events coming from the process $p\bar{p} \to Wjj \to l\nu_l jj$. Other sources of background, such as multijet events where a jet is misidentified as a lepton, or $b\bar{b}$ production, are discussed in section 6.3.

6.1 Signal region definition

Lepton identification, jet reconstruction, and neutrino energy measurement were introduced in chapter 4. We shall now use these event selection tools to define a signal region with minimal background contamination. The backgrounds that concern us here are those coming from fake leptons, $b\bar{b}$ production, and to a lesser extent, Z^0 and Drell-Yan processes. A separation between top and W+dijet events will not yet be attempted: it will be the subject of chapter 7. An examination of the Monte Carlo samples described in chapter 5 will guide us in several instances.

6.1.1 Event vertex

The z-coordinate of CDF event vertices has a gaussian distribution with mean at the center of the detector and with standard deviation around 35 cm. This is shown in figure 6.1 for a sample of 8000 inclusive muon events satisfying some loose cuts. To insure good containment of the jets and leptons in the calorimeters, we require the primary vertex of each event to be within 60 cm of the center of the detector.

6.1.2 Jet topology

For the top signature we are considering, events should contain several jets: two jets from the hadronic decay of one of the W's, two bottom quark jets, and jets from initial state radiation. Accordingly, we require at least two jets per event, with a transverse energy greater than 10 GeV and a pseudo-rapidity η_d less than 2. Here, η_d is the pseudo-rapidity calculated with respect to the center of the detector rather than the event vertex. Accepted jets will thus penetrate the central or plug calorimeter.

6.1.3 Lepton selection

Electrons and muons are required to pass the identification cuts listed in sections 4.1.4 and 4.2.3 respectively, and to enter the fiducial regions described in sections 4.1.5 and 4.2.4. In addition, electrons must pass the conversion filter (section 4.1.7), and muons the cosmic ray filter (section 4.2.5).

6.1.4 Missing transverse energy and lepton isolation

By analyzing the kinematics of heavy quark semileptonic decays, it was pointed out at the end of chapter 1 that a high transverse momentum lepton will be surrounded with less energy if its parent quark is the top rather than the bottom. Similar isolation properties should prove helpful for rejecting fake leptons arising from misidentified jets. In figure 6.2, we show a scatter plot of the electron border tower transverse energy BE versus the missing transverse energy $\not\!\!E_T$, for events with two jets and a 'good' electron with $p_T^e \geq 20$ GeV/c. A comparison with figures 6.3 and 6.4 indicates clearly that the majority of W and top events are characterized by high $\not\!\!E_T$ and low BE. The same conclusion can be drawn for events in the muon channel, as is seen from scatter plots 6.5 through 6.7. We therefore enrich the W and top quark content of our event samples by requiring

$\not\!\!E_T \geq 20\,\mathrm{GeV}$ and $BE < 2\,\mathrm{GeV}$. These cuts, combined with the lepton transverse momentum cut described in the next section, retain at least 20% of the $t\bar{t}$ events with a lepton and two or more jets, for $m_{top} \geq 60$ GeV/c^2. On the other hand, as will be shown later, the remaining background from QCD and $b\bar{b}$ production is between 10 and 20%.

6.1.5 Lepton transverse momentum

The average transverse momentum of leptons from quark decay increases with the quark's mass. This provides a way to separate $t\bar{t}$ production from $b\bar{b}$ production and from other lower energy processes. Figure 6.8 is a scatter plot of the muon transverse momentum p_T^μ versus $\not\!\!E_T$, for events with an isolated 'good' muon and two or more jets. The same plot is shown in figures 6.9 and 6.10 for the W and $t\bar{t}$ Monte Carlo data sets. For our final event samples we require the transverse momentum of the lepton to be at least 20 GeV/c.

6.1.6 Removal of $Z^0 \to l^+l^-$ events

Our event selection requires the presence of a single high p_T isolated lepton. A large fraction of events associated with Z^0 or Drell-Yan production will satisfy this lepton demand, and can only be eliminated by the missing transverse energy cut and the dijet requirement. A small background will still remain due to the limited resolution of the $\not\!\!E_T$ measurement. To improve rejection of Z^0 events, a special filter is used.

In the electron channel, this filter rejects events containing a second central electron of opposite charge, with $Had/EM < 0.1$, $E/p < 2$, and combining with the first electron to form an invariant mass between 70 and 110 GeV/c^2. Events are also rejected when a second electron is found outside the central region, if it passes the above Had/EM and invariant mass cuts.

In the muon channel, the Z^0 filter looks for a second CTC track with $p_T \geq 10\,\mathrm{GeV/c}$, and pointing to a calorimeter tower with $EM < 2\,\mathrm{GeV}$, $Had < 6\,\mathrm{GeV}$, and $Iso(0.4) < 10$ GeV. If this track is less than 5 cm away from the muon track along the z direction, and if the two tracks make up an invariant mass greater than 65 GeV/c^2, the event is discarded.

We have applied the Z^0 filter on our W and top Monte Carlo data sets and found it to be less than 1% overefficient. A study of ISAJET simulated Z^0 decays leads to the conclusion that the remaining Z^0 background in the final samples is less than (1.0 ± 0.4) % in the electron channel and less than (1.6 ± 0.6) % in the muon channel.

6.1.7 Event counts

Table 6.1 shows the number of events left in the CDF and Monte Carlo data sets after the cuts described in the previous subsections are applied. The Monte Carlo samples have been normalized as described in section 5.3.4. The ratio of muon over electron events observed in the CDF data disagrees with the Monte Carlo predictions. This will be further investigated in section 6.3 below.

Event sample	Muons	Electrons	Ratio (%)
CDF data	79 ± 9	107 ± 10	74 ± 11
PAPAGENO W + 2 jets	53 ± 2	98 ± 3	54 ± 3
ISAJET $t\bar{t}$, $m_{top} = 60$ GeV/c^2	27 ± 1	55 ± 2	49 ± 3
ISAJET $t\bar{t}$, $m_{top} = 70$ GeV/c^2	20 ± 1	40 ± 1	51 ± 3
ISAJET $t\bar{t}$, $m_{top} = 80$ GeV/c^2	15 ± 1	28 ± 1	56 ± 2

Table 6.1: Final event sample sizes in the CDF and Monte Carlo data sets. The last column gives the ratio of the muon to electron event counts. The uncertainties shown are statistical only, and do not include the uncertainty on the Monte Carlo acceptance corrections.

6.2 Comparison with W+dijet production

In this section we present several event quantities for comparison between the data and the PAPAGENO W+dijet calculation. Figures 6.11 through 6.20 show PAPAGENO histograms with CDF data points from the final electron or muon

sample superimposed. The quantities represented are the lepton–neutrino transverse mass and transverse momentum, the dijet invariant mass, and the azimuth and pseudo-rapidity separation between the two highest E_T jets in each event. The transverse mass and momentum are calculated according to the following prescription:

$$m_T^{l\nu} \stackrel{\text{def}}{=} \sqrt{2\,(|\vec{p}_T^{\,l}|\,|\vec{\not{E}}_T| - \vec{p}_T^{\,l} \cdot \vec{\not{E}}_T)} \tag{6.1}$$

$$\vec{p}_T^{\,l\nu} \stackrel{\text{def}}{=} \vec{p}_T^{\,l} + \vec{\not{E}}_T \tag{6.2}$$

The good agreement between data and Monte Carlo indicates that the final samples are primarily composed of W+dijet events.

6.3 Backgrounds from multijet and $b\bar{b}$ production

QCD multijet events contaminate the signal region by faking lepton signatures, and through fluctuations in the amount and location of energy deposited by individual jets. A typical case of electron misidentification occurs when the trajectory of a neutral pion overlaps that of a charged pion inside a jet. The charged pion leaves a track in the CTC, whereas the neutral pion gives up most of its energy in the electromagnetic calorimeter, thus exhibiting an electron-like signature. Prompt muon signals, on the other hand, are faked by charged hadrons which punch through the calorimeters without depositing much energy, or when fast pions and kaons decay in flight into muons and neutrino's. Finally, substantial amounts of missing transverse energy can be generated when jets escape unseen through cracks in the detector, or simply fluctuate by the amount of energy they deposit. The signal region also includes contributions from $b\bar{b}$ production, since this process is a genuine source of leptons and neutrino's; these are of lesser energy however, than the decay products of W and top.

We use two different methods to estimate the multijet and $b\bar{b}$ contamination of our final event samples. The methods have in common a study of lepton isolation characteristics, since leptons from the background are expected to be less isolated than those from the signal processes.

6.3.1 Method 1: BE versus $\not{E}_T$

For the first method, we start from a scatter plot of the border tower transverse energy BE versus the missing transverse energy $\not{E}_T$ (figures 6.2 and 6.5), and define four regions (see diagram below):

Region A: $BE \geq 5$ GeV and $\not{E}_T \leq 10$ GeV

Region B: $BE \geq 5$ GeV and $\not{E}_T \geq 20$ GeV

Region C: $BE \leq 2$ GeV and $\not{E}_T \leq 10$ GeV

Region D: $BE \leq 2$ GeV and $\not{E}_T \geq 20$ GeV

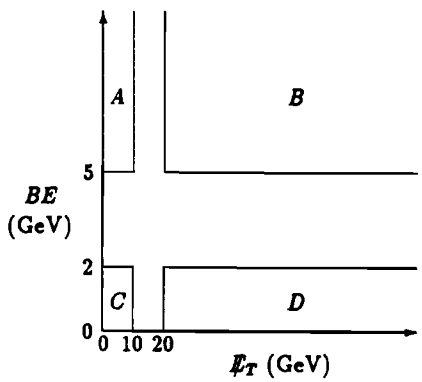

Regions A, B and C contain mostly background, whereas D is the signal region. Let us write N_X for the total number of events in region X, and B_X for the number of background events in X. If we can assume that BE and $\not{E}_T$ are uncorrelated for background events, then the following must hold:

$$\frac{B_D}{B_B} = \frac{B_C}{B_A} \tag{6.3}$$

or, since $B_A \approx N_A$, $B_B \approx N_B$ and $B_C \approx N_C$:

$$B_D \approx \frac{N_B \cdot N_C}{N_A} \tag{6.4}$$

Scatter plots 6.2 and 6.5 do not show any obvious correlation between BE and $\not{E}_T$. It has been argued elsewhere [Abe91c] that this is simply a consequence of the fact that the parts of a background event which contribute to BE are independent of the parts which contribute to $\not{E}_T$.

In the electron sample, we find $N_A = 169$, $N_B = 22$ and $N_C = 78$, so that $B_D = 10 \pm 3$, corresponding to a (10 ± 3) % background fraction in the final sample.

In the muon sample, $N_A = 94$, $N_B = 22$ and $N_C = 67$, giving $B_D = 16 \pm 4$, or a (20 ± 6) % background fraction in the final sample.

6.3.2 Method 2: Isolation efficiency

The second method requires that we estimate the efficiency ϵ_W of the isolation cut $BE < 2$ GeV on true W or top events, and the efficiency ϵ_b of the same cut on background events. We calculate ϵ_W from our samples of PAPAGENO W+dijet events, and ϵ_b from samples of lepton+dijet data with $\not{E}_T < 10$ GeV. Furthermore, let S be the set of events which satisfy all the requirements listed in section 6.1 except for lepton isolation. Define N_p (N_f) to be the number of events in S which pass (fail) the isolation cut, N_W the number of true W or top events in S, and N_b the number of true background events. We have the following relations:

$$N_p = \epsilon_W N_W + \epsilon_b N_b \tag{6.5}$$

$$N_p + N_f = N_W + N_b \tag{6.6}$$

which can be solved for N_W and N_b. The background fraction f_{bg} in our final sample is then:

$$f_{bg} = \frac{\epsilon_b N_b}{N_p} \tag{6.7}$$

For the CDF electron sample, we obtain $\epsilon_W = (92 \pm 7)$ %, $\epsilon_b = (21 \pm 3)$ %, $N_p = 107$ and $N_f = 44$. Our equations are then solved with $N_W = 105 \pm 19$ and $N_b = 46 \pm 26$, so that $f_{bg} = (9 \pm 5)$ %.

In the muon case, $\epsilon_W = (88 \pm 5)\,\%$, $\epsilon_b = (25 \pm 3)\,\%$, $N_p = 79$ and $N_f = 38$. This yields $N_W = 79 \pm 18$ and $N_b = 38 \pm 23$. The fraction of background in the final muon sample is $f_{bg} = (12 \pm 8)\,\%$.

6.3.3 Summary

The background estimates obtained by the two methods described above are consistent with each other. They favor a higher background in the muon sample than in the electron sample, though not quite sufficient to explain the discrepancy in muon to electron ratio displayed in table 6.1. To understand this better, we consider the set of events obtained from our final sample definition without the two jet requirement, and study the muon to electron ratio as a function of the number of jets with $E_T > 10$ GeV and $\eta_d < 2$ in the event. We introduce the notation N_i^μ (N_i^e) for the number of events in the muon (electron) channel which have exactly i jets, and R_i^μ (R_i^e) for the ratio of the number of events with i jets to the number of events with $i-1$ jets. Measurement results are listed in table 6.2. The muon to electron ratios for data events with 0 or 1 jet are consistent with the PAPAGENO prediction of $(54 \pm 3)\,\%$ for the 2 jet case. The muon to electron ratio for data events with 2 jets is approximately two standard deviations above this expected value. A look at the R_2^μ and R_2^e ratios indicates that this effect results from a relative excess in the number of muon events combined with a slight depletion in the relative number of electron events. This supports the assertion that jets spawn fake muon signals more easily than fake electron signals. The following observation corroborates this interpretation. When counting the number of jets in an electron event, only calorimetry clusters whose centroid is at least an (η, ϕ) distance of 0.7 away from the electron are taken into account. This is done in order to avoid counting the electron cluster itself as an additional jet. No similar restriction is made in the muon channel, but it can certainly be tried. This is shown in table 6.3. Most numbers have shifted in the expected direction. In particular, the excess in the two jet mode has been somewhat reduced.

Number of jets	Muon channel		Electron channel		N_i^μ/N_i^e (%)
	N_i^μ	R_i^μ (%)	N_i^e	R_i^e (%)	
0	975		1927		51 ± 2
1	244	25 ± 2	427	22 ± 1	57 ± 5
2	64	26 ± 4	85	20 ± 2	75 ± 12
3	11	17 ± 6	21	25 ± 6	52 ± 19
4	4		1		
Total	1298		2461		53 ± 2

Table 6.2: Final sample sizes before the jet requirement. For each lepton channel, the number N_i of events with i jets, and the ratio $R_i \stackrel{\text{def}}{=} N_i/N_{i-1}$ are given. The last column gives the muon to electron ratio for each event class.

Number of jets	Muon channel		Electron channel		N_i^μ/N_i^e (%)
	N_i^μ	R_i^μ (%)	N_i^e	R_i^e (%)	
0	1005		1927		52 ± 2
1	223	22 ± 2	427	22 ± 1	52 ± 4
2	57	26 ± 4	85	20 ± 2	67 ± 11
3	10	18 ± 6	21	25 ± 6	48 ± 18
4	3		1		
Total	1298		2461		53 ± 2

Table 6.3: Final sample sizes before the jet requirement. This is the same as table 6.2, except that jets are only counted if they are at least an (η, ϕ) distance of 0.7 away from the lepton.

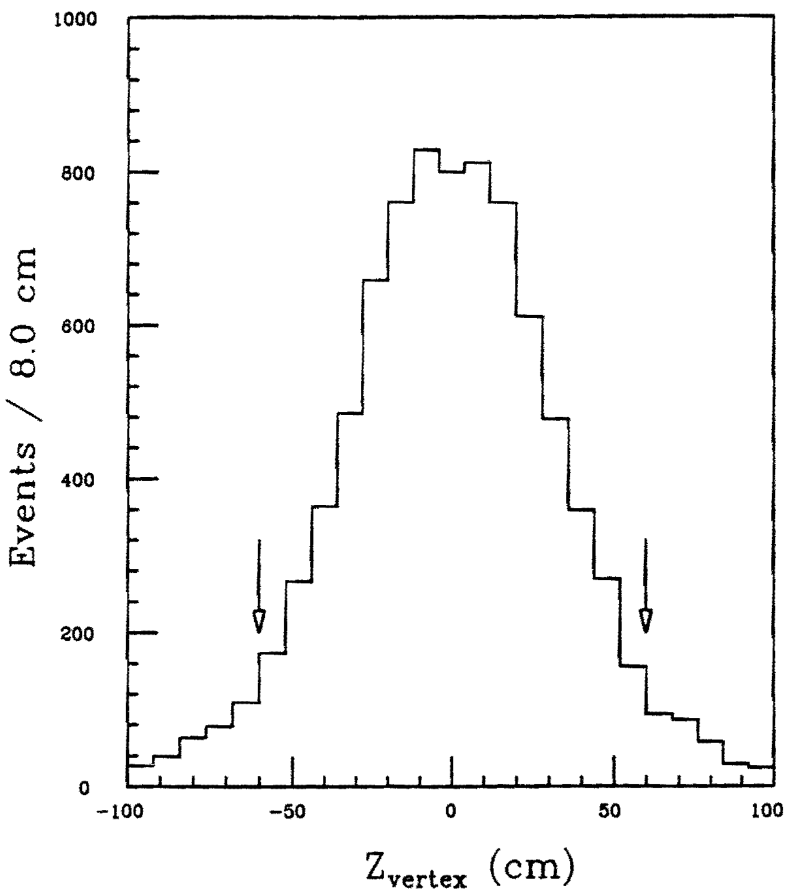

Figure 6.1: Event vertex distribution along the beam axis for a sample of inclusive muon events passing loose muon identification cuts. The arrows indicate the cuts made in the analysis.

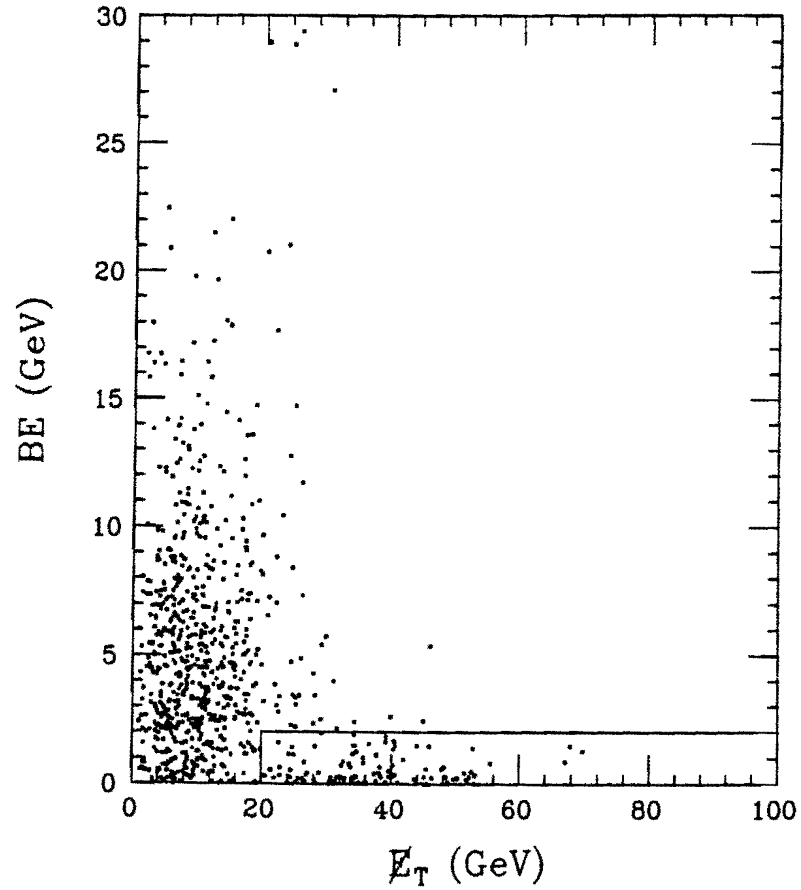

Figure 6.2: CDF data: electron border tower transverse energy versus missing transverse energy for events with two jets and an electron passing the identification cuts, the fiducial cuts, and with $p_T^e \geq 20\,\mathrm{GeV/c}$. The contour marks the cuts made in the analysis.

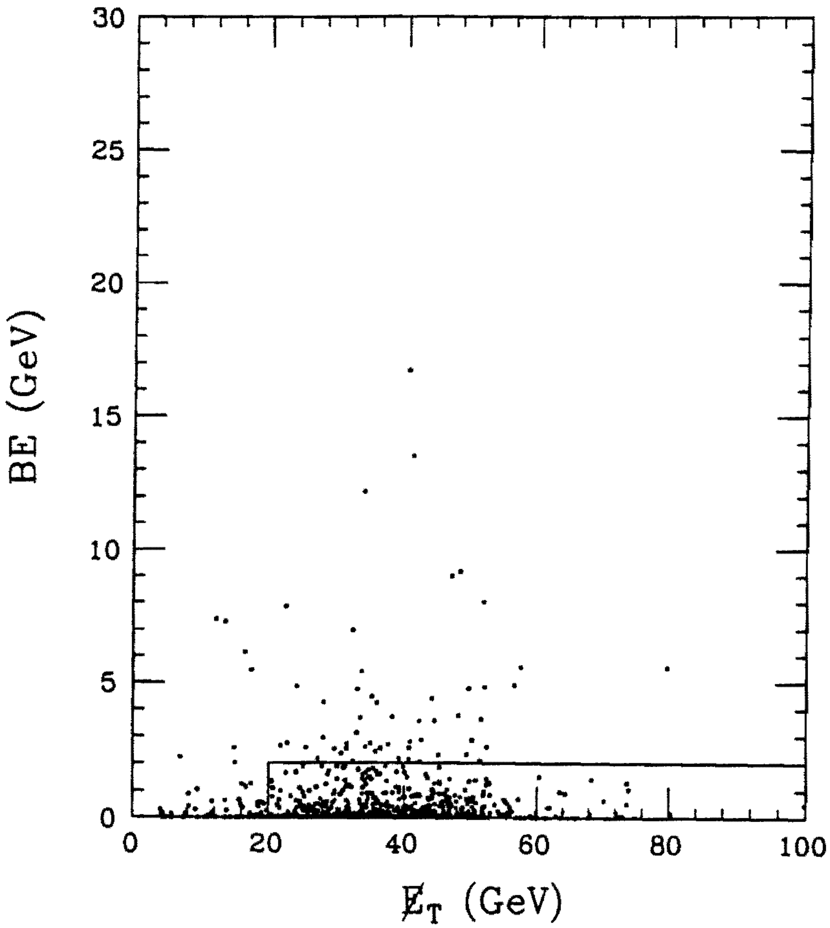

Figure 6.3: Same as figure 6.2, but for a 28 pb^{-1} sample of PAPAGENO W+dijet events.

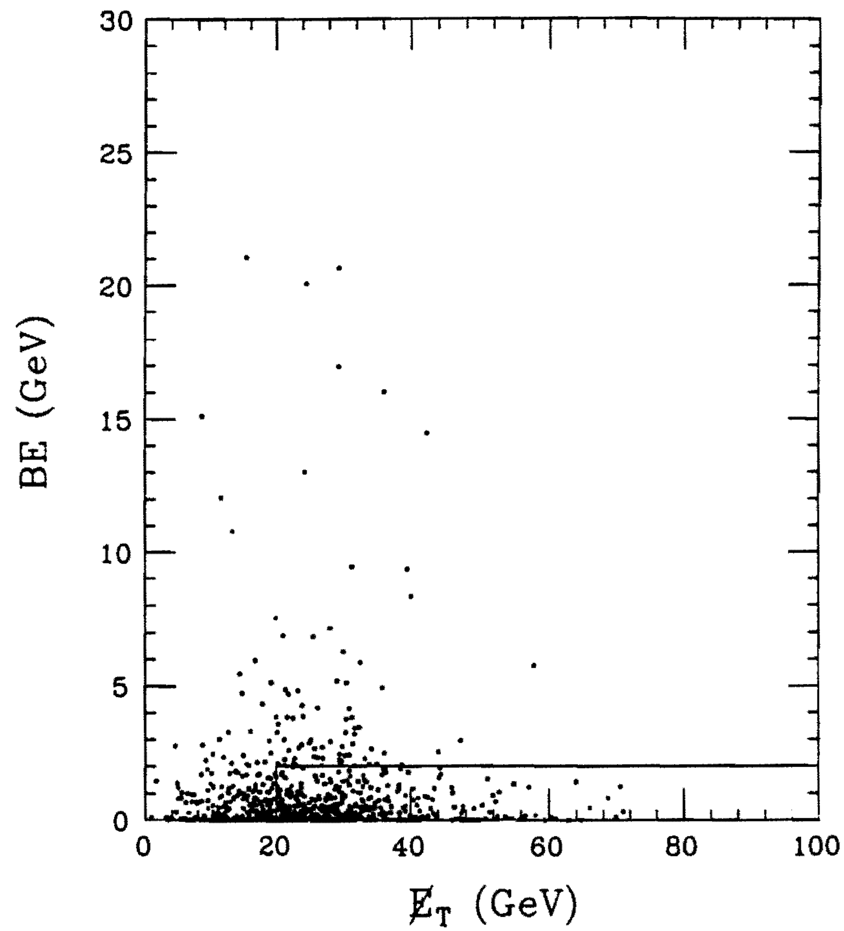

Figure 6.4: Same as figure 6.2, but for a 46 pb^{-1} sample of ISAJET $t\bar{t}$ events, with $m_{top} = 70$ GeV/c^2.

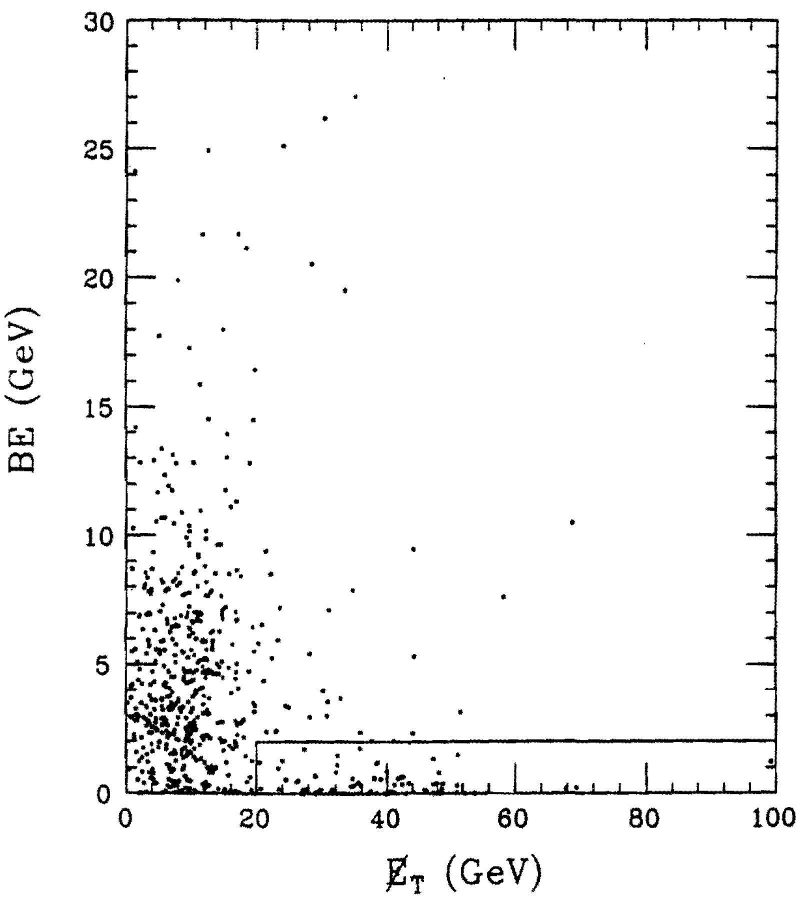

Figure 6.5: CDF data: muon border tower transverse energy versus missing transverse energy for events with two jets and a muon passing the identification cuts, the fiducial cuts, and with $p_T^\mu \geq 20$ GeV/c. The contour marks the cuts made in the analysis.

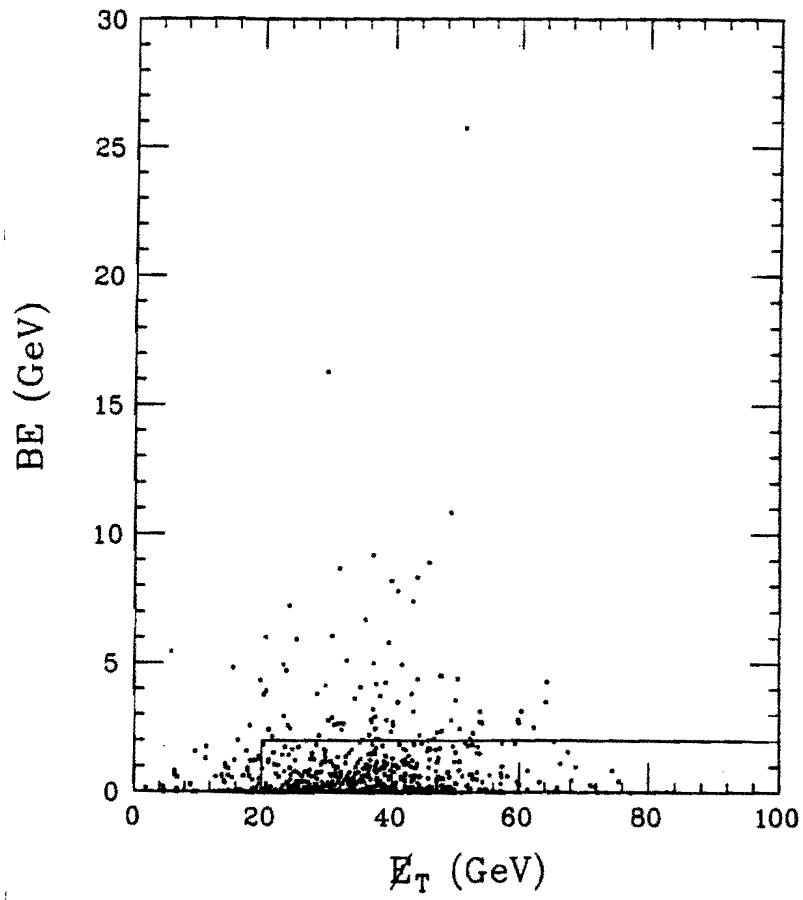

Figure 6.6: Same as figure 6.5, but for a 35 pb^{-1} sample of PAPAGENO W+dijet events.

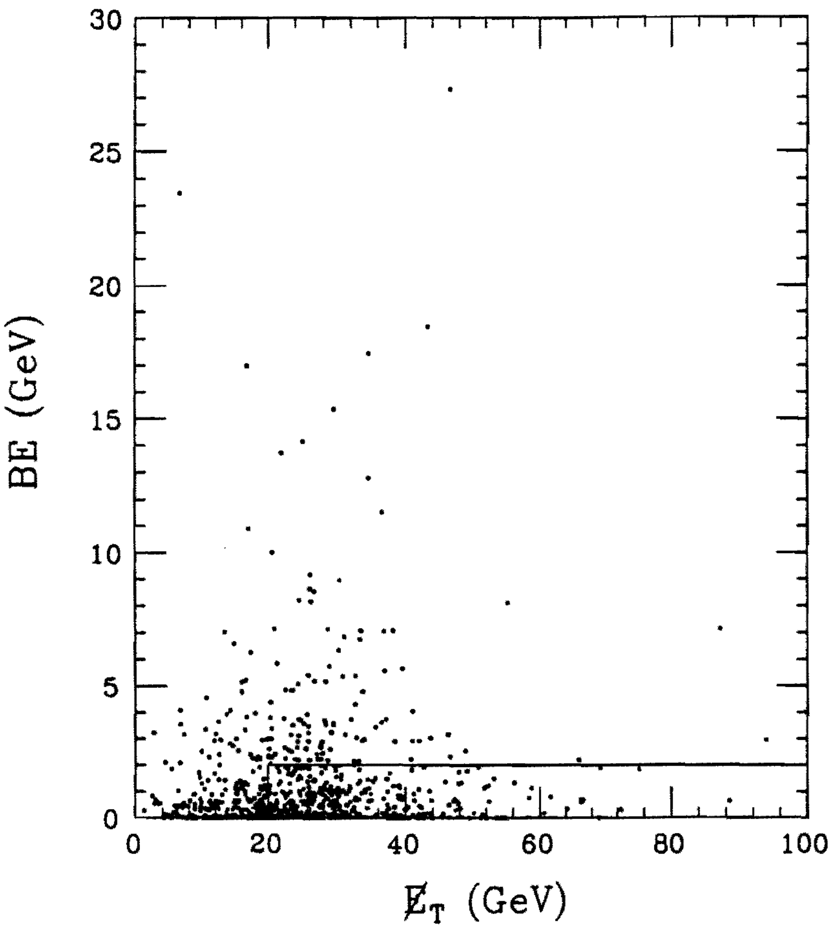

Figure 6.7: Same as figure 6.5, but for a 65 pb^{-1} sample of ISAJET $t\bar{t}$ events, with $m_{top} = 70$ GeV/c^2.

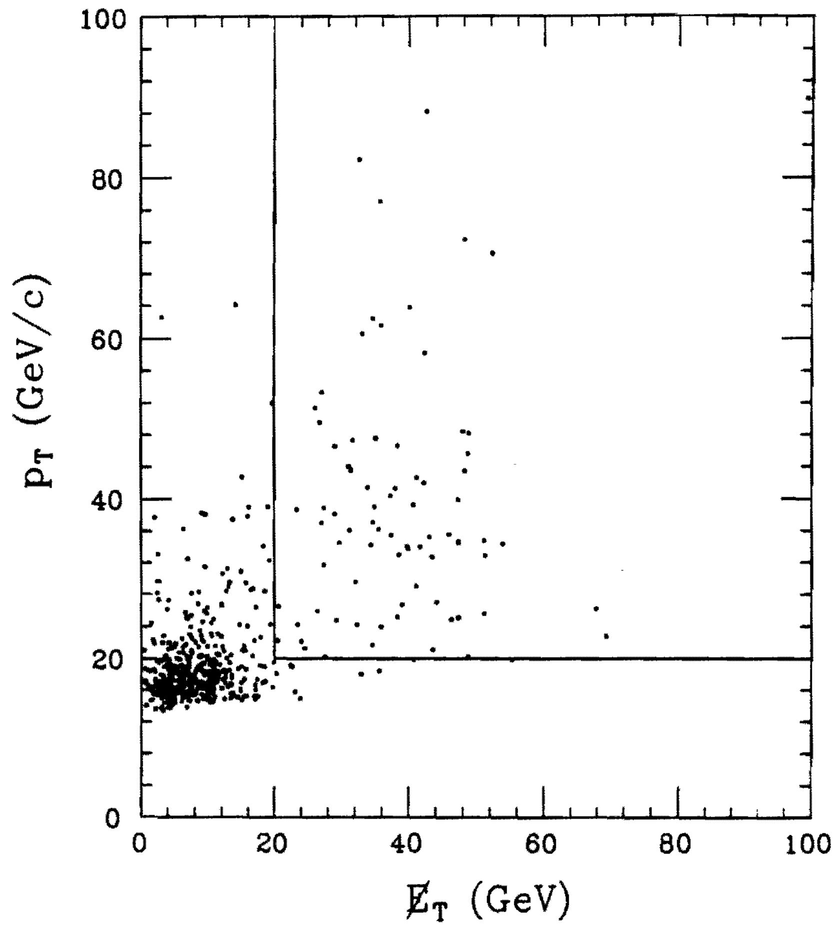

Figure 6.8: CDF data: muon transverse momentum versus missing transverse energy for events with two jets and a muon passing the identification and fiducial cuts, and with $BE < 2$ GeV and $p_T \geq 15$ GeV/c. The contour marks the cuts made in the analysis.

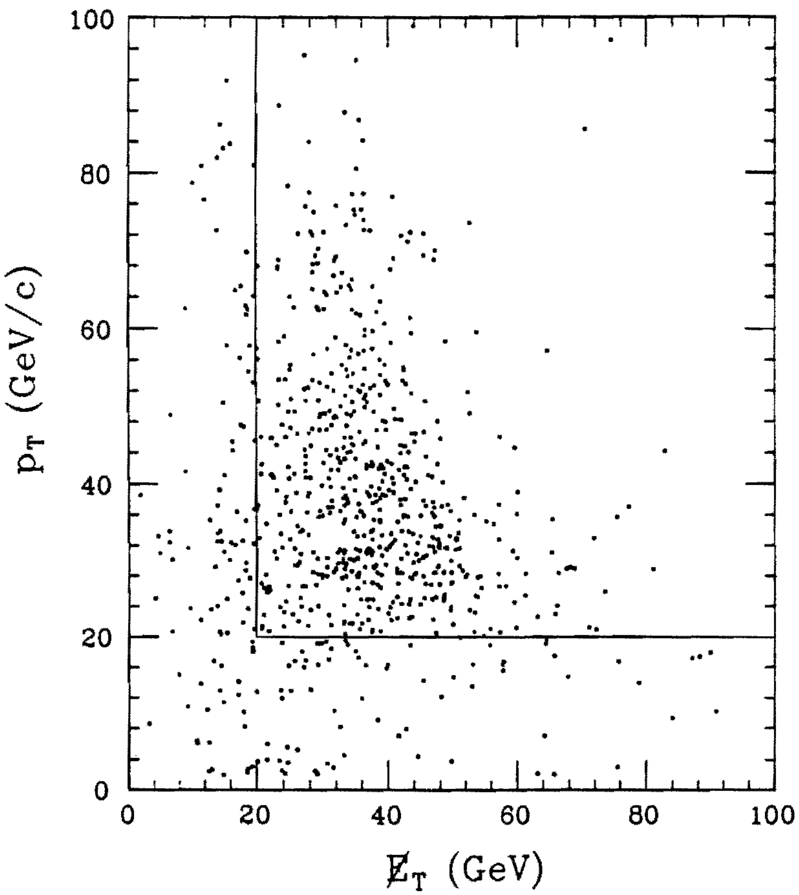

Figure 6.9: Same as figure 6.8, but for a 35 pb^{-1} sample of PAPAGENO W+dijet events, and without the muon p_T cut.

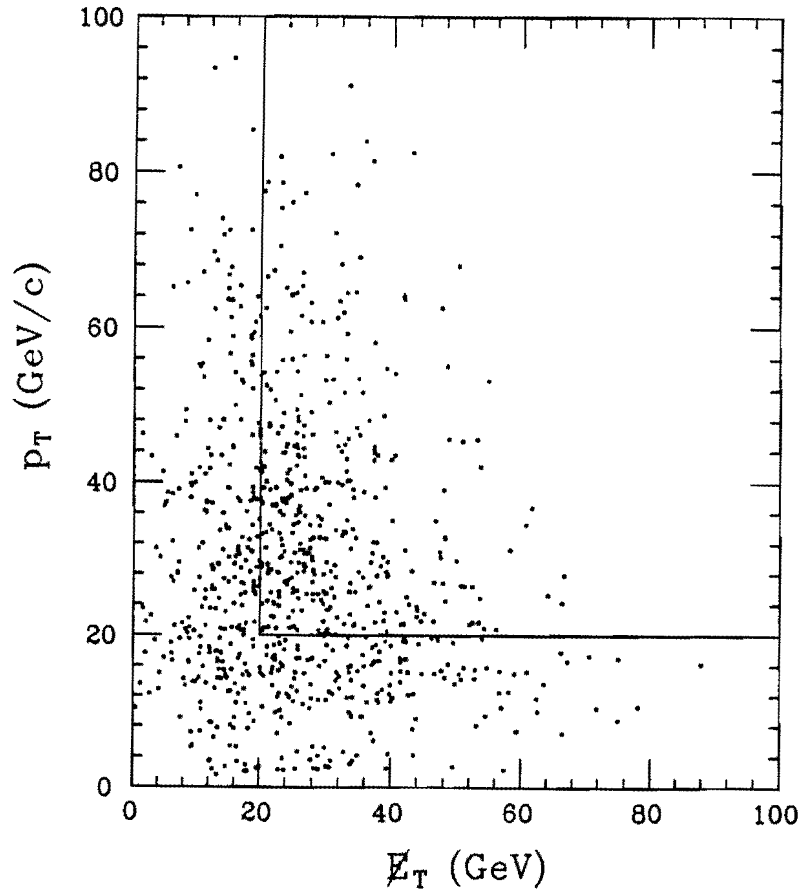

Figure 6.10: Same as figure 6.8, but for a 55 pb^{-1} sample of ISAJET $t\bar{t}$ events, with m_{top} = 70 GeV/c^2. No muon p_T cut was done for this plot.

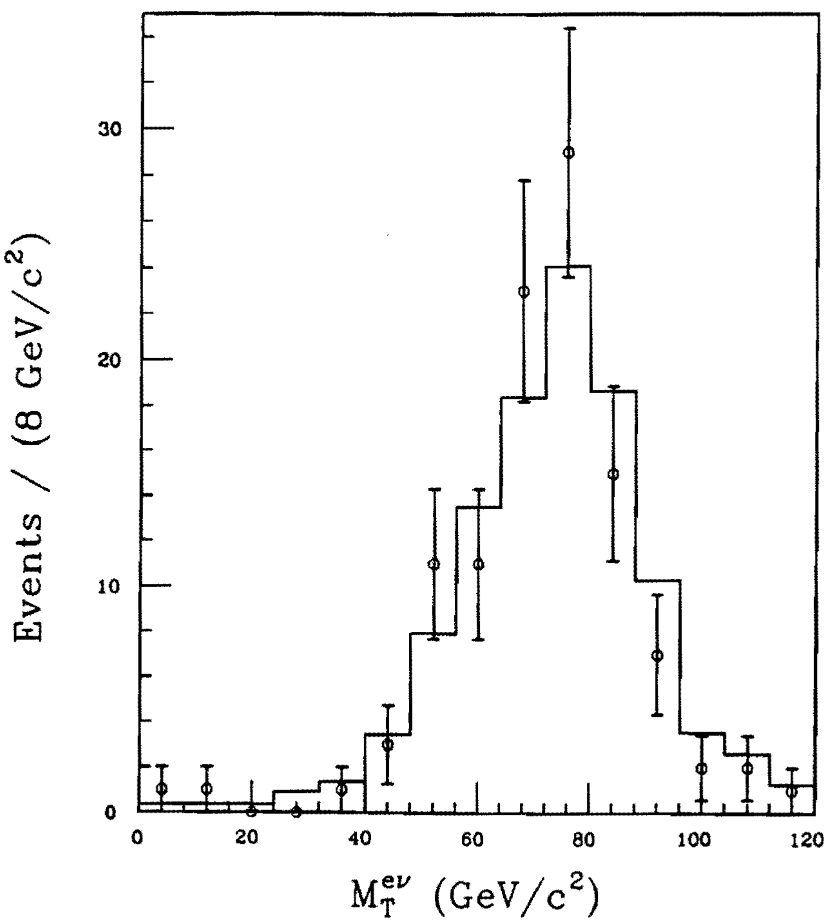

Figure 6.11: Lepton-neutrino transverse mass distribution for the final CDF electron sample and for the W+dijet Monte Carlo (histogram, normalized to the data).

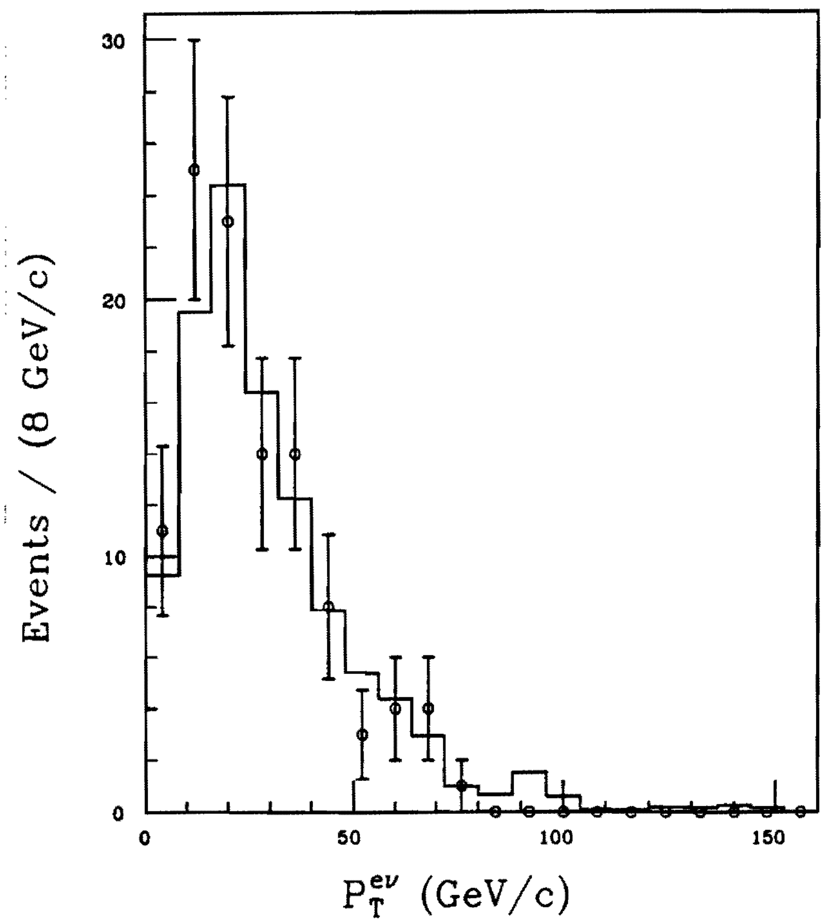

Figure 6.12: Lepton-neutrino transverse momentum distribution for the final CDF electron sample and for the W+dijet Monte Carlo (histogram, normalized to the data).

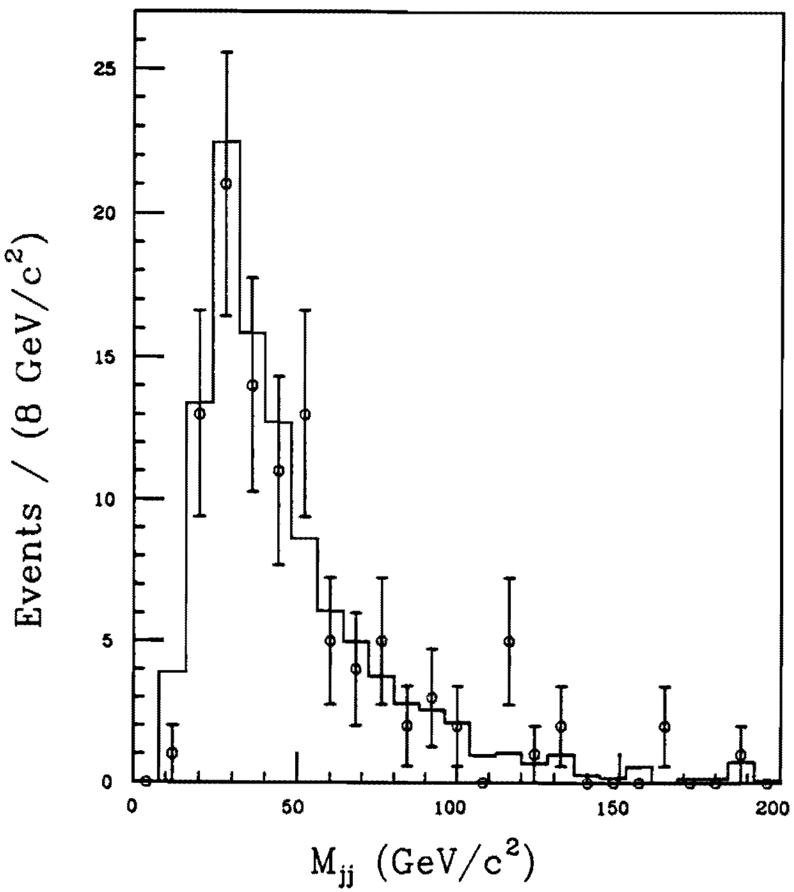

Figure 6.13: Dijet invariant mass distribution for the final CDF electron sample and for the W+dijet Monte Carlo (histogram, normalized to the data).

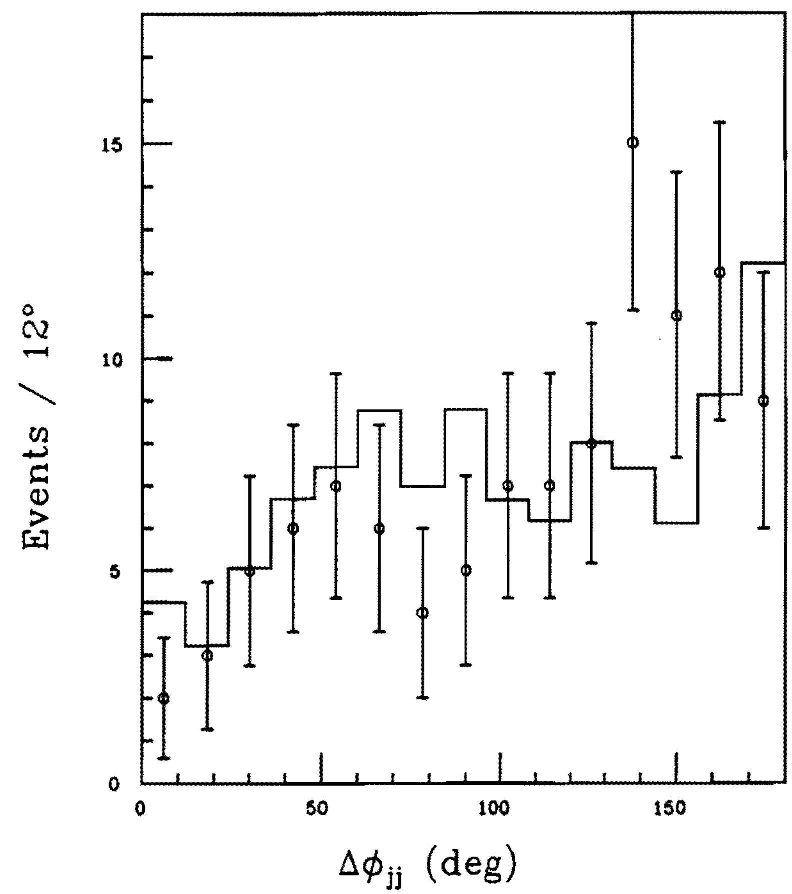

Figure 6.14: Azimuthal separation between the two highest E_T jets, for the final CDF electron sample and for the W+dijet Monte Carlo (histogram, normalized to the data).

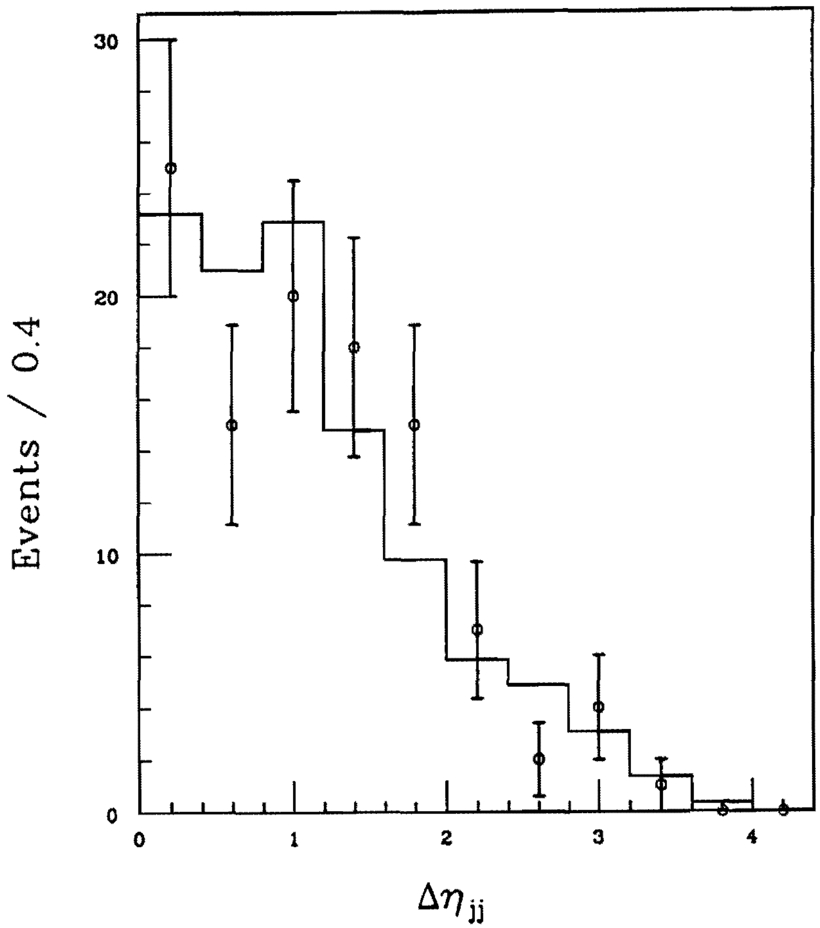

Figure 6.15: Pseudo-rapidity separation between the two highest E_T jets, for the final CDF electron sample and for the W+dijet Monte Carlo (histogram, normalized to the data).

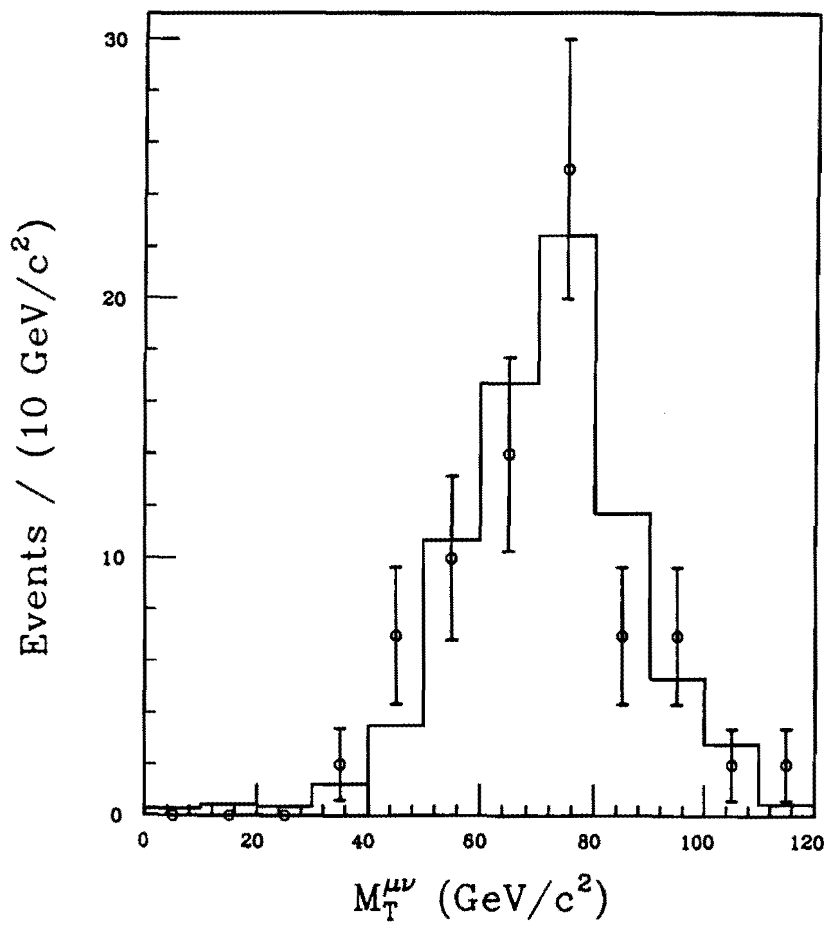

Figure 6.16: Lepton–neutrino transverse mass distribution for the final CDF muon sample and for the W+dijet Monte Carlo (histogram, normalized to the data).

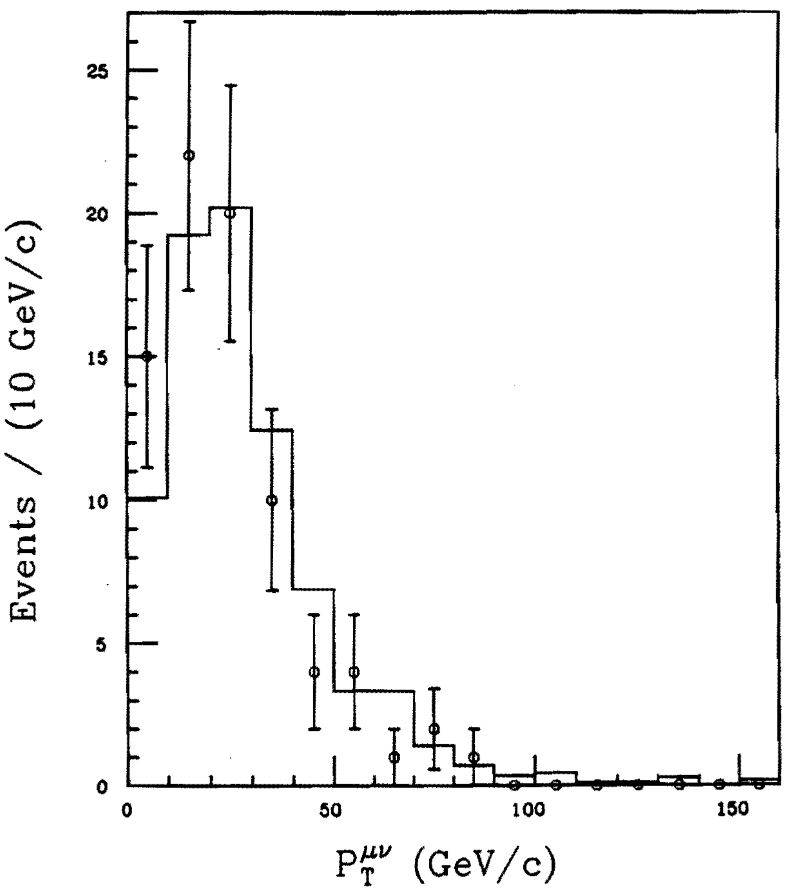

Figure 6.17: Lepton-neutrino transverse momentum distribution for the final CDF muon sample and for the W+dijet Monte Carlo (histogram, normalized to the data).

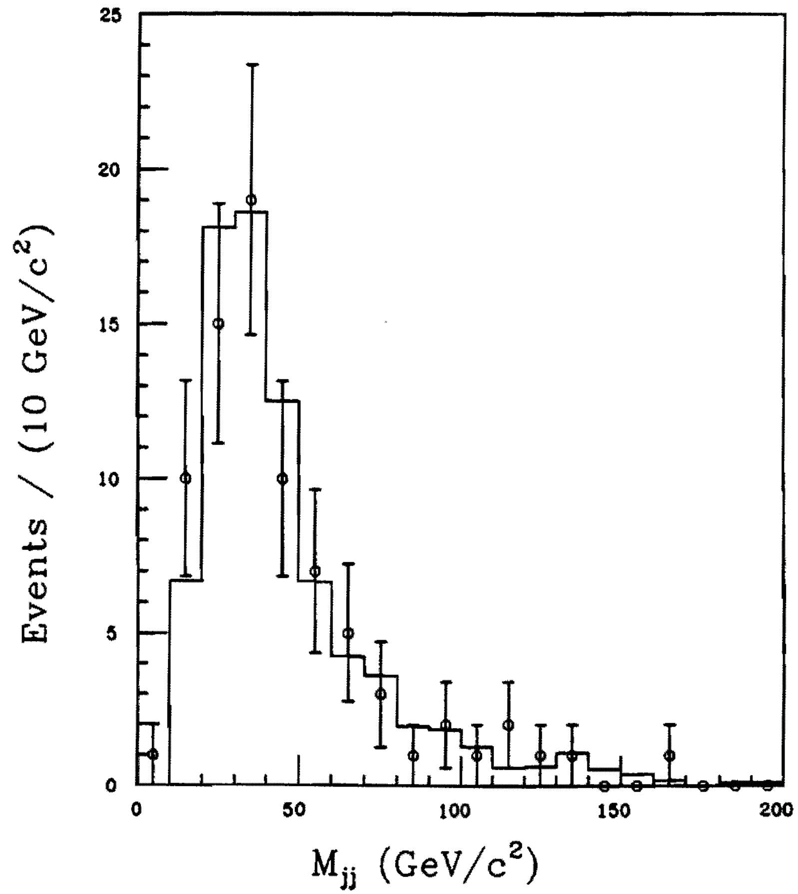

Figure 6.18: Dijet invariant mass distribution for the final CDF muon sample and for the W+dijet Monte Carlo (histogram, normalized to the data).

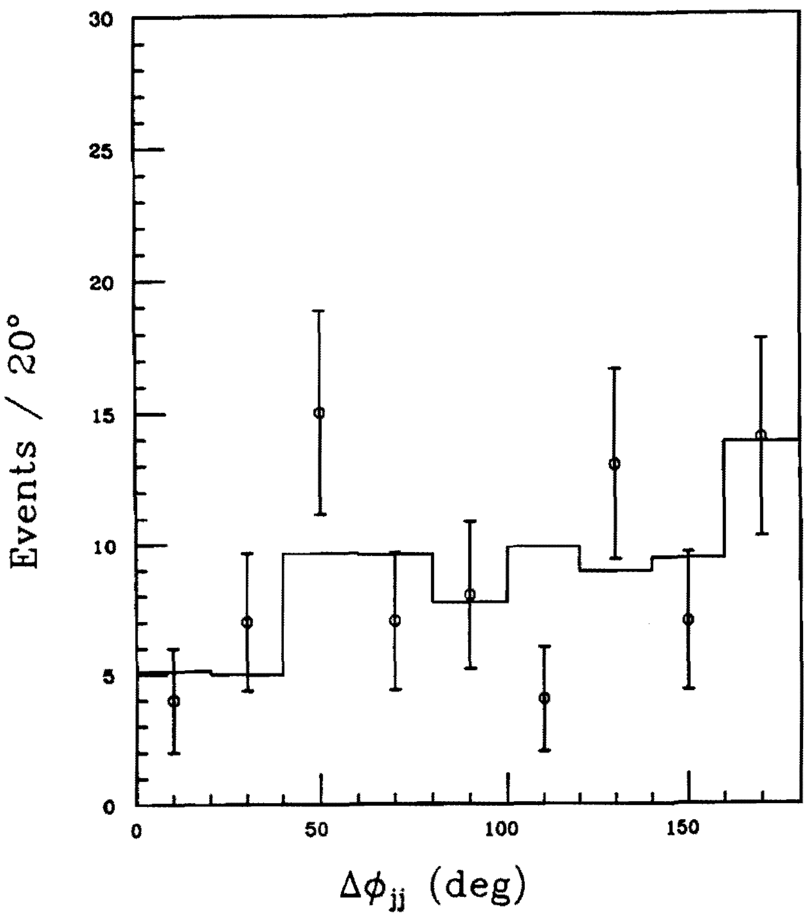

Figure 6.19: Azimuthal separation between the two highest E_T jets, for the final CDF muon sample and for the W+dijet Monte Carlo (histogram, normalized to the data).

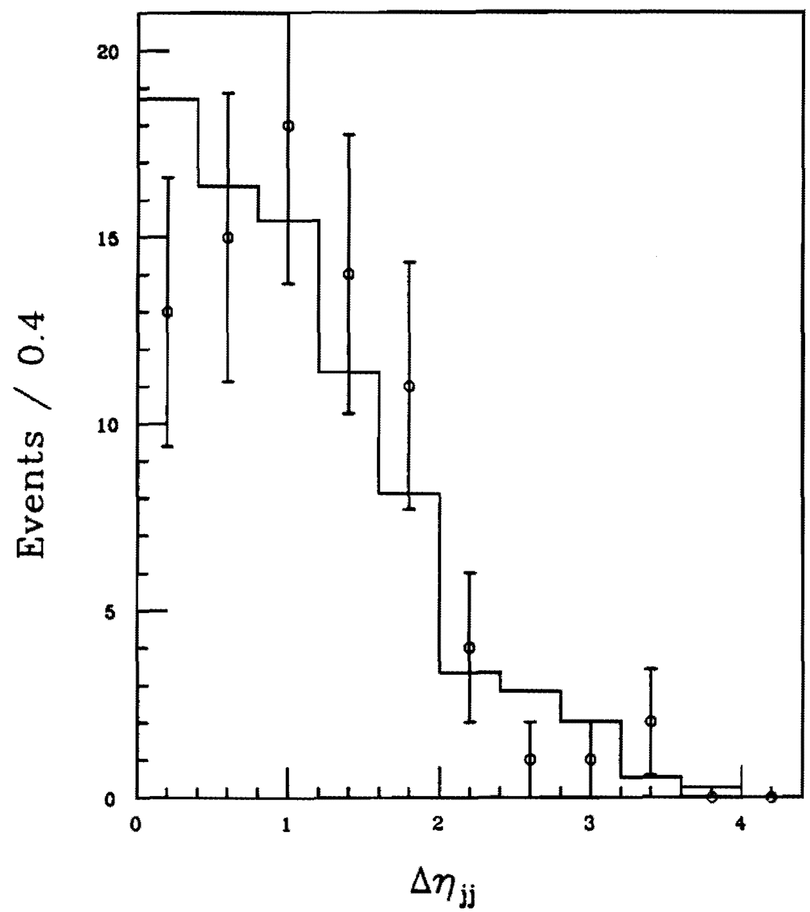

Figure 6.20: Pseudo-rapidity separation between the two highest E_T jets, for the final CDF muon sample and for the W+dijet Monte Carlo (histogram, normalized to the data).

Chapter 7

Transverse Mass Analysis

In section 6.2, the final event samples were shown to be consistent with production of a W accompanied by two jets. Given the available statistics and our understanding of the backgrounds, the production of top quarks does not appear necessary to explain the data. In this chapter, we shall try to quantify this statement by setting an upper limit on the $t\bar{t}$ production cross section for each top mass for which we have a Monte Carlo data set. By comparing these upper limits with the theoretical calculation of the cross section described in chapter 1, we shall be able to derive a lower limit on the top mass.

The occurrence of the process $p\bar{p} \to t\bar{t} + X \to l\nu_l jj + X$ according to Standard Model predictions should be observable in several ways [Bae89,Ros89]. For example, the fraction of W events which contain n or more jets will be enhanced by $t\bar{t}$ contributions. This is also the case for the ratio of (W + n jet) to (Z + n jet) events. If its mass is large enough, the top should alter the shape of the dijet invariant mass spectrum in events containing a W and two or more jets. On the other hand, for a top mass below the W mass, the transverse mass spectrum of the lepton–neutrino system should exhibit a shoulder to the left of the W peak. Of all these signatures, the transverse mass one is the least sensitive to the large systematic uncertainties associated with jet reconstruction. In figures 7.1 to 7.4 we show Monte Carlo transverse mass spectra for the W+dijet process with and without top contributions of various masses added in. We shall use the shape of these spectra to estimate an upper limit on the $t\bar{t}$ content of the data. Clearly, as the top's mass increases, the change of shape it induces becomes less significant, so that we do not expect our method to work for top masses above 80 GeV/c^2.

The ability of the CDF detector simulation program to adequately model the

resolution of the transverse mass measurement has been demonstrated in [Abe91a]. This was done by comparing a sample of W + 1 jet events, where the W decays into the electron channel, to a corresponding Monte Carlo sample. The rationale for using an exclusive W + 1 jet sample is the low top quark contamination (at most 15% if the top mass is above 60 GeV/c^2), combined with some significant hadronic activity to smear the missing transverse energy measurement. One may nevertheless argue that the missing transverse energy resolution is not only affected by the jet energy measurement itself, but also by the relative orientation of jets in a given event. Thus, a satisfactory check of the W + 1 jet case does not guarantee that the Monte Carlo properly models transverse mass spectra in the W + 2 jet case. In what follows, we shall overlook this objection, and trust that our general methodology, as well as our estimate of the systematic uncertainties, are sufficiently conservative to yield reliable results.

7.1 Disentangling $t\bar{t}$ from W contributions

Let us for the moment assume that the final data samples contain no background, and consist exclusively of W and top events. One can then try to fit the transverse mass distribution, in each lepton channel separately, to a linear superposition of the corresponding W and top distributions:

$$\frac{dN}{dm_T^{l\nu}} = \alpha\,\mathcal{T}(m_T^{l\nu}) + \beta\,\mathcal{W}(m_T^{l\nu}) \tag{7.1}$$

where $\mathcal{W}$ and $\mathcal{T}$ are the transverse mass distributions obtained from our Monte Carlo data sets, with the normalizations described in chapter 5. The coefficients α and β simply represent the respective amounts of $t\bar{t}$ and W Monte Carlo needed to fit the data. It is important to realize that the normalization of the Monte Carlo W sample does not affect the fitted value of α; only the shape of the distributions matters.

In addition to W and possibly $t\bar{t}$, our data samples contain contributions from background processes such as $b\bar{b}$ and $c\bar{c}$ production, QCD jets with misidentified leptons, $W \to \tau\bar{\nu}_\tau \to e\bar{\nu}_e\nu_\tau\bar{\nu}_\tau$, $W \to \tau\bar{\nu}_\tau \to \mu\bar{\nu}_\mu\nu_\tau\bar{\nu}_\tau$, and, if the top mass is below 65 GeV/c^2, $W \to t\bar{b}$. Events from all these processes will yield low values of transverse mass, thereby enhancing the effective top contribution determined from the fit. Thus our upper limits on $\sigma_{t\bar{t}}(\mathrm{m_{top}})$ will tend to be conservative estimates.

7.1.1 The fitting procedure

A binned maximum likelihood method is used to determine the W and top contents of the data [Abe91a]. We assume that Poisson statistics govern the bin contents, and introduce likelihood functions $\mathcal{L}_e(\alpha,\beta)$ and $\mathcal{L}_\mu(\alpha,\beta)$ in each lepton channel separately:

$$\mathcal{L}(\alpha,\beta) \stackrel{\mathrm{def}}{=} \prod_{i=1}^{N} \frac{m_i^{k_i}}{k_i!}\, e^{-m_i} \tag{7.2}$$

where we dropped the e/μ subscript not to overload the notation. In this definition, N is the number of bins, k_i the number of events observed in bin i, and m_i the number of events expected in bin i:

$$m_i \stackrel{\mathrm{def}}{=} \alpha\, t_i + \beta\, w_i \tag{7.3}$$

with t_i, w_i the number of events predicted in bin i by the top and W Monte Carlo's respectively. The best fit for α and β is found by maximising $\mathcal{L}(\alpha,\beta)$, or equivalently, by minimizing the function:

$$L(\alpha,\beta) \stackrel{\mathrm{def}}{=} -\ln\mathcal{L} - \sum_{i=1}^{N} \ln k_i! \;=\; \sum_{i=1}^{N} (m_i - k_i \ln m_i) \tag{7.4}$$

which is the negative log-likelihood up to terms independent of α and β.

We shall also attempt a combined fit of the transverse mass spectra in the electron and muon channels. The combined likelihood function is given by [Fro79]:

$$\mathcal{L}_{e\mu}(\alpha,\beta) \stackrel{\mathrm{def}}{=} \mathcal{L}_e(\alpha,\beta)\cdot\mathcal{L}_\mu(\alpha,\beta) \tag{7.5}$$

7.1.2 Results

We have used the MINUIT program [Jam75] to minimise the modified log-likelihood function (7.4) in the electron channel, the muon channel, and both channels combined. In the electron channel, the fit was done over 12 bins from 24 to 120

GeV/c^2. A coarser binning was chosen in the muon channel to compensate for the smaller event count: 10 bins from 20 to 120 GeV/c^2. The fits were repeated for each of the top masses $\mathrm{m_{top}}$ = 60, 70 and 80 GeV/c^2. Results are shown in table 7.1. The statistical uncertainties on α and β correspond to a change of 0.5 in the log-likelihood. The numbers are consistent with no top in the 60–80 GeV/c^2 mass range, although results from the muon channel are much less constraining that those from the electron channel. This is partly due to the excess of muon over electron events observed in the data. If the number of muon events in the data is artificially lowered to agree with the Monte Carlo predicted ratio to the number of electron events in the data, the 60 GeV/c^2 fit in the muon channel gives $\alpha = 0.15 \pm 0.19$ instead of 0.21 ± 0.22. Log-likelihood contour plots of α versus β are shown in figures 7.5 to 7.8.

Lepton channel	$\mathrm{m_{top}}$ (GeV/c^2)	α	β	χ^2	N_{DF}
e	60	0.00 ± 0.12	1.09 ± 0.13	8.0	10
	70	0.01 ± 0.24	1.09 ± 0.15	7.9	10
	80	0.26 ± 0.74	1.02 ± 0.23	7.7	10
μ	60	0.21 ± 0.22	1.34 ± 0.19	12.1	8
	70	0.44 ± 0.39	1.28 ± 0.21	11.3	8
	80	0.64 ± 1.10	1.26 ± 0.35	12.4	8
$e+\mu$	60	0.06 ± 0.11	1.19 ± 0.11	25.9	20
	70	0.17 ± 0.21	1.15 ± 0.12	25.0	20
	80	0.42 ± 0.62	1.10 ± 0.19	25.3	20

Table 7.1: Transverse mass fit results in the electron channel, the muon channel, and both channels combined. The uncertainties shown are statistical only. The last two columns indicate the χ^2 of the fit and the number of degrees of freedom.

7.2 Systematic uncertainties on the $t\bar{t}$ contribution

In order to derive an upper limit on $\sigma_{t\bar{t}}$, we shall need to estimate the systematic uncertainty on the fitted fraction α of $t\bar{t}$ events in our data samples. It will also be necessary to understand how this systematic uncertainty varies with α. We shall therefore distinguish between the uncertainty δn on the number of predicted $t\bar{t}$ events, and the uncertainty Δs on the shape of the transverse mass distributions [Abe91a]. Uncertainties on the jet energy scale, underlying event, and fit interval contribute to Δs, which is expressed as an absolute uncertainty. On the other hand, δn is expressed fractionally and combines uncertainties on the integrated luminosity of the data samples, on the lepton detection efficiencies, the number of jets from initial state radiation, and top quark fragmentation properties. We shall treat δn and Δs as statistically independent, and write the total systematic uncertainty $\sigma(\alpha)$ on α as:

$$\sigma(\alpha) = \sqrt{(\Delta s)^2 + (\alpha \cdot \delta n)^2} \tag{7.6}$$

The next section describes in detail the calculations of δn and Δs for the electron, muon, and combined lepton samples.

7.2.1 Uncertainties affecting event counts: δn

Top quark fragmentation

The fragmentation characteristics of the top quark affect the amount of energy deposited in the vicinity of the decay lepton, and hence its isolation. This was studied in reference [Abe91a] by varying the ϵ_Q parameter in the Peterson fragmentation model (equation 1.20) from 0.2 GeV^2/m$_{top}^2$ to 1.5 GeV^2/m$_{top}^2$. The nominal value used by ISAJET is $\epsilon_Q = 0.5\,\mathrm{GeV}^2/\mathrm{m}_{top}^2$. The higher value leads to a decrease in acceptance of about 7.6% for $\mathrm{m}_{top} = 60$ GeV/c^2 and 5.0% for higher top masses. Although these results were obtained for the electron case, we shall assume that they also hold in the muon case since the isolation cuts used for both types of lepton are very similar. When considering the combined electron and muon sample, we shall again use the same numbers, for these uncertainties are completely correlated.

Initial state radiation

The number and the transverse energy of jets produced by initial state radiation affects the acceptance of $t\bar{t}$ events by our selection cuts. The associated systematic uncertainty was estimated as follows. For each reconstructed jet in a given Monte Carlo $t\bar{t}$ event, we made a list of the generated particles which fell within an (η, ϕ) radius of 0.7 from the jet axis, and computed the fraction of total transverse energy carried by these particles, which does not come from initial state radiation. The reconstructed jet transverse energy was then multiplied by this fraction, and the jet selection criteria reapplied. We take half the resulting change in acceptance as our systematic uncertainty due to initial state radiation. This systematic uncertainty was separately computed in the electron channel, the muon channel, and both channels combined. The difference between the three cases however, is not very significant (see table 7.2).

Lepton detection efficiency

The efficiency of the lepton identification criteria was determined with a statistical uncertainty of 2.4% on CDF data, and 0.5% on Monte Carlo data. We shall conservatively take 3% as the uncertainty on the Monte Carlo modeling of lepton identification. Since the uncertainties $\Delta\epsilon_\mu$ and $\Delta\epsilon_e$ on the muon and electron detection efficiencies are associated with binomial fluctuations on independent measurements, they should be considered as uncorrelated when calculating their effect on the combined electron plus muon sample. Thus, if $N_{t\bar{t}}^{\mu}$ and $N_{t\bar{t}}^{e}$ are the numbers of $t\bar{t}$ events predicted in the muon and electron channels respectively, then the systematic uncertainty $\Delta\epsilon$ due to lepton identification in the combined sample is given by:

$$\Delta\epsilon = \frac{\sqrt{\left(\Delta\epsilon_\mu N_{t\bar{t}}^{\mu}\right)^2 + \left(\Delta\epsilon_e N_{t\bar{t}}^{e}\right)^2}}{N_{t\bar{t}}^{\mu} + N_{t\bar{t}}^{e}} \tag{7.7}$$

This equation predicts a $\Delta\epsilon$ which is somewhat smaller on the combined sample than the uncertainty on each individual sample. Here again we have chosen a conservative approach and take $\Delta\epsilon = 3\%$.

Integrated luminosity

The luminosity measurement described in chapter 3 carries an uncertainty of 6.8%, common to all data samples.

Results

Table 7.2 summarizes our estimates of the systematic uncertainties in the overall normalization, as a function of top mass. As stated above, these are fractional uncertainties.

Lepton channel	m_{top} (GeV/c^2)	Fragmentation model	Initial-state radiation	Lepton efficiency	Integrated luminosity	Total δn
e	60	0.076	0.136	0.03	0.068	0.173
	70	0.050	0.110	0.03	0.068	0.142
	80	0.050	0.092	0.03	0.068	0.128
μ	60	0.076	0.123	0.03	0.068	0.163
	70	0.050	0.091	0.03	0.068	0.128
	80	0.050	0.068	0.03	0.068	0.112
$e+\mu$	60	0.076	0.132	0.03	0.068	0.169
	70	0.050	0.104	0.03	0.068	0.137
	80	0.050	0.083	0.03	.0.068	0.122

Table 7.2: Relative systematic uncertainties on the predicted number of $t\bar{t}$ events. The uncertainties are summed in quadrature in the last column.

7.2.2 Uncertainties affecting the transverse mass: Δs

By far the largest systematic uncertainty on the transverse mass measurement comes from the Monte Carlo modeling of the missing transverse energy $\not{E}_T$. The uncertainty on this quantity has two sources: the jet energy scale and the underlying event. An additional systematic uncertainty arises from the choice of transverse mass interval over which the fit is performed.

Monte-Carlo jet energy scale

The Monte Carlo modeling of the jet energy scale was estimated to be correct within 20% in section 5.3.1. To evaluate the effect of this uncertainty on the W and top Monte Carlo transverse mass spectra, we artificially changed all the jet energies by $\pm 20\%$, recalculated the $\not{E}_T$ and the transverse mass, and reselected the events. This procedure gave us new transverse mass distributions $\mathcal{T}$ and $\mathcal{W}$ which we used to refit the data and obtain new values for the parameter α. The results are shown in table 7.3.

Lepton channel	m_{top} (GeV/c^2)	Nominal fit	Jet energy scale +20%	Jet energy scale −20%
e	60	0.00 ± 0.12	-0.12 ± 0.08	0.12 ± 0.15
	70	0.01 ± 0.24	-0.20 ± 0.20	0.18 ± 0.30
	80	0.26 ± 0.74	-0.38 ± 0.60	0.77 ± 0.94
μ	60	0.21 ± 0.22	0.14 ± 0.18	0.44 ± 0.32
	70	0.44 ± 0.39	0.25 ± 0.32	0.72 ± 0.54
	80	0.64 ± 1.12	0.41 ± 0.88	1.30 ± 1.27
$e+\mu$	60	0.06 ± 0.11	-0.03 ± 0.08	0.20 ± 0.15
	70	0.17 ± 0.20	-0.01 ± 0.17	0.33 ± 0.27
	80	0.42 ± 0.62	-0.03 ± 0.48	1.02 ± 0.75

Table 7.3: Values of the fitted $t\bar{t}$ fraction α obtained after varying the jet energy scale by amounts corresponding to the systematic uncertainty on this quantity. The uncertainties shown are statistical only.

Underlying event model

The underlying event energy is defined as the vector sum of all the calorimeter energy not contained in an electron cluster, nor in a jet cluster of E_T greater than 5 GeV. The mean underlying event E_T in our lepton + 2 jet data agrees to within 15% with the W+dijet and $t\bar{t}$ Monte Carlo's. We adopt a conservative approach and take 20% to be the systematic uncertainty on the underlying event E_T. The effect of this uncertainty on the fitted amount of $t\bar{t}$ in the data was determined in the same manner as for the jet energy scale uncertainty. Results are shown in table 7.4.

Lepton channel	m_{top} (GeV/c^2)	Nominal fit	Underlying event +20%	Underlying event −20%
e	60	0.00 ± 0.12	0.01 ± 0.12	-0.05 ± 0.12
	70	0.01 ± 0.24	0.32 ± 0.25	-0.05 ± 0.24
	80	0.26 ± 0.74	0.38 ± 0.77	0.14 ± 0.72
μ	60	0.21 ± 0.22	0.25 ± 0.22	0.26 ± 0.22
	70	0.44 ± 0.39	0.49 ± 0.37	0.53 ± 0.39
	80	0.64 ± 1.12	0.83 ± 1.06	1.18 ± 1.05
$e+\mu$	60	0.06 ± 0.11	0.09 ± 0.11	0.07 ± 0.11
	70	0.17 ± 0.20	0.21 ± 0.20	0.18 ± 0.20
	80	0.42 ± 0.62	0.56 ± 0.61	0.58 ± 0.58

Table 7.4: Values of the fitted $t\bar{t}$ fraction α obtained after varying the underlying event E_T by amounts corresponding to the systematic uncertainty on this quantity. The uncertainties shown are statistical only.

Transverse mass interval used in the fit

The effect of the transverse mass interval used in the fit was determined by refitting the data using either one more or one less bin at the low end of the transverse mass spectrum. For the case of the combined electron + muon fit, we added, then removed one bin from both lepton spectra simultaneously. The corresponding values of α are shown in table 7.5.

Results

For each of the three effects described above, we calculated the systematic uncertainty on α as the corresponding average shift in α. Unphysical values of α were not allowed: whenever α was found negative by the fitting, it was reset to zero for the computation of the systematic uncertainty. The results are shown in table 7.6.

Lepton channel	m_{top} (GeV/c^2)	Nominal fit	Fit interval +1 bin	Fit interval −1 bin
e	60	0.00 ± 0.12	0.03 ± 0.12	0.00 ± 0.13
	70	0.01 ± 0.24	0.06 ± 0.24	0.04 ± 0.25
	80	0.26 ± 0.74	0.47 ± 0.72	0.41 ± 0.76
μ	60	0.21 ± 0.22	0.18 ± 0.22	0.26 ± 0.23
	70	0.44 ± 0.39	0.39 ± 0.38	0.47 ± 0.40
	80	0.64 ± 1.12	0.45 ± 1.09	0.98 ± 1.10
$e+\mu$	60	0.06 ± 0.11	0.07 ± 0.11	0.09 ± 0.11
	70	0.17 ± 0.20	0.18 ± 0.20	0.20 ± 0.21
	80	0.42 ± 0.62	0.49 ± 0.61	0.65 ± 0.62

Table 7.5: Values of the fitted $t\bar{t}$ fraction α obtained after adding or removing one bin at the low end of the transverse mass interval used in the fit. The uncertainties shown are statistical only.

Lepton channel	m_{top} (GeV/c^2)	Jet energy scale	Underlying event	$m_T^{l\nu}$ interval	Total Δs
e	60	0.061	0.005	0.015	0.063
	70	0.089	0.016	0.040	0.099
	80	0.390	0.119	0.180	0.446
μ	60	0.153	0.047	0.040	0.165
	70	0.234	0.068	0.041	0.246
	80	0.446	0.362	0.264	0.632
$e+\mu$	60	0.100	0.019	0.020	0.103
	70	0.166	0.027	0.020	0.169
	80	0.510	0.148	0.147	0.551

Table 7.6: Absolute systematic uncertainties in α, due to effects requiring the transverse mass distribution to be refit. The uncertainties are summed in quadrature in the last column.

7.2.3 Other systematic uncertainties

Top quark production properties were studied in reference [Abe91a] by comparing the ISAJET and PAPAGENO Monte Carlo's. It was found that PAPAGENO generates a slightly softer top quark transverse momentum distribution, but the effects on the transverse mass measurement and $t\bar{t}$ acceptance are insignificant for top masses greater than 50 GeV/c^2.

Other possible sources of uncertainty, such as the electron energy calibration and the muon track momentum reconstruction, are negligible compared to the effects studied above.

7.3 Limits on $\sigma_{t\bar{t}}$ and m_{top}

The first step towards deriving an upper limit on the $t\bar{t}$ production cross section is to obtain a likelihood distribution for α, the fitted fraction of $t\bar{t}$ events. This operation is however not uniquely defined, as it requires that we reduce a two-dimensional likelihood function $\mathcal{L}(\alpha,\beta)$ to a one-dimensional one by somehow eliminating the β dependence. There are at least three reasonable ways of proceeding. In the simplest case, one introduces a *conditional* likelihood:

$$\mathcal{L}_{con}(\alpha) \stackrel{\text{def}}{=} N_{con}\,\mathcal{L}(\alpha,\beta_{max}), \tag{7.8}$$

where N_{con} is a normalization constant which insures that the integral of $\mathcal{L}_{con}(\alpha)$ over the physical range of α is 1.0, and β_{max} is the value of β at the maximum of $\mathcal{L}(\alpha,\beta)$. A conditional likelihood allows one to make probability statements regarding one parameter (α in this case), for a fixed value of the second parameter. A second possibility is to use the *marginal* likelihood:

$$\mathcal{L}_{mar}(\alpha) \stackrel{\text{def}}{=} N_{mar} \int_0^{+\infty} \mathcal{L}(\alpha,\beta)\,d\beta \tag{7.9}$$

In contrast with the first case, confidence intervals constructed from a marginal likelihood are valid for any value of the parameter that has been integrated out. Finally, one can also define the *maximal* likelihood:

$$\mathcal{L}_{max}(\alpha) \stackrel{\text{def}}{=} N_{max} \max_{\beta\in[0,+\infty]} \mathcal{L}(\alpha,\beta) \tag{7.10}$$

Here again, the one-dimensional likelihood is normalized to an area of 1.0 over the range of positive α. In figures 7.5 to 7.8, the dotted line in the (α,β) plane shows the path along which the likelihood must be evaluated to obtain $\mathcal{L}_{max}(\alpha)$ up to an overall normalization factor. In our subsequent calculations, we shall always use the $\mathcal{L}_{max}$ solution of the aforementioned ambiguity, because it incorporates in a natural way correlations between α and β.

Before extracting upper limits on the $t\bar{t}$ cross section from $\mathcal{L}_{max}$, we must first convolute this likelihood function with a smearing factor, which we take to be a Gaussian with width equal to the total systematic uncertainty $\sigma(\alpha)$, as defined in equation (7.6):

$$\hat{\mathcal{L}}(\hat{\alpha}) \stackrel{\text{def}}{=} \int_0^{+\infty} \mathcal{L}_{max}(\alpha)\, \frac{e^{-\frac{1}{2}\frac{(\hat{\alpha}-\alpha)^2}{(\Delta s)^2+(\alpha\,\delta n)^2}}}{\sqrt{2\pi[(\Delta s)^2+(\alpha\,\delta n)^2]}}\,d\alpha \tag{7.11}$$

Note that this convolution preserves the normalization of the likelihood function, provided we define $\hat{\mathcal{L}}(\hat{\alpha})$ to be zero for negative $\hat{\alpha}$. Several examples of the smeared and unsmeared top likelihood functions are plotted in figures 7.9 to 7.12.

Given a likelihood function $\hat{\mathcal{L}}(\hat{\alpha})$, the 95% confidence level upper limit $\hat{\alpha}_{max}$ is defined by:

$$\int_0^{\hat{\alpha}_{max}} \hat{\mathcal{L}}(\hat{\alpha})\,d\hat{\alpha} \;=\; 0.95 \tag{7.12}$$

For each top mass, we then obtain a 95% confidence level upper limit on the $t\bar{t}$ production cross section from the relation:

$$\hat{\sigma}_{max} \;=\; \sigma_{t\bar{t}}\;\hat{\alpha}_{max} \tag{7.13}$$

where $\sigma_{t\bar{t}}$ is the cross section used to normalize the Monte Carlo samples, and $\hat{\alpha}_{max}$ is the solution of equation (7.12) for the appropriate smeared top likelihood function. The upper limit $\hat{\sigma}_{max}$ is actually independent of $\sigma_{t\bar{t}}$. This follows from equation (7.13), and from the fact that α, being the fraction of $t\bar{t}$ cross section needed to fit the data, is inversely proportional to $\sigma_{t\bar{t}}$. A summary of the numbers used in the calculation of the upper limits is presented in table 7.7.

In figure 7.13, the upper limit on $\sigma_{t\bar{t}}$ is plotted as a function of mass, together

Lepton channel	m_{top} (GeV/c^2)	$\alpha \pm$ (stat)	Δs	δn	σ_{max} (pb)	$\hat{\sigma}_{max}$ (pb)	Theoretical $\sigma_{t\bar{t}}^{min}$ (pb)	Theoretical $\sigma_{t\bar{t}}$ (pb)
e	60	0.00 ± 0.12	0.063	0.173	358	412	995	1260
	70	0.01 ± 0.24	0.099	0.142	313	346	453	569
	80	0.26 ± 0.74	0.446	0.128	490	577	229	285
μ	60	0.21 ± 0.22	0.165	0.163	857	1004	995	1260
	70	0.44 ± 0.39	0.246	0.128	702	787	453	569
	80	0.64 ± 1.10	0.632	0.112	814	923	229	285
$e+\mu$	60	0.06 ± 0.11	0.103	0.169	363	473	995	1260
	70	0.17 ± 0.21	0.169	0.137	324	397	453	569
	80	0.42 ± 0.62	0.551	0.122	452	581	229	285

Table 7.7: Summary of the calculation of upper limits on the $t\bar{t}$ cross section. The upper limits obtained from the unsmeared (σ_{max}) and smeared ($\hat{\sigma}_{max}$) top likelihood functions are both indicated. The theoretical numbers are from [Ell91].

with the theoretical prediction. The points where the experimental curves intersect the lower theoretical curve correspond to the 95% C.L. lower limits on the top mass. The top mass intervals *excluded* by this analysis are:

1. For the electron+dijet sample: $60 < m_{top} < 73$ GeV/c^2, at the 95% C.L.,
2. For the muon+dijet sample, no 95% C.L. interval can be excluded; at the 90% C.L., we can exclude $60 < m_{top} < 63$ GeV/c^2,
3. For the combined electron+dijet and muon+dijet samples: $60 < m_{top} < 72$ GeV/c^2, at the 95% C.L.

The result obtained from the combined electron and muon channels is actually weaker than the result from the electron channel alone. This is entirely due to the higher level of background in the muon channel. As noted earlier, background processes yield low transverse mass values, thereby faking a $t\bar{t}$ signal. Clearly, adding this type of false information to the analysis can only weaken its conclusion.

The significance of the above numbers can be illustrated by performing a simple test on our calculation methods: what upper limit can we set on the $t\bar{t}$ content of the Monte Carlo W+dijet sample? In other words, assuming that PAPAGENO correctly models W+dijet data, what are the best results one could hope to obtain from the data? Here, we completely neglect the effect of systematic uncertainties and background contamination. We take full advantage of the high statistics of our Monte Carlo samples, while still maintaining the normalization derived from the CDF data sets. In table 7.8, we show the parameter values and unsmeared upper limits on $\sigma_{t\bar{t}}$ obtained from this test. Using these numbers, one

Lepton channel	m_{top} (GeV/c^2)	α	β	N_{DF}	σ_{max} (pb)
e	60	0.00 ± 0.11	1.00 ± 0.12	10	332
	70	0.00 ± 0.22	1.00 ± 0.14	10	281
	80	0.00 ± 0.63	1.00 ± 0.21	10	383
μ	60	0.00 ± 0.17	1.00 ± 0.16	8	553
	70	0.00 ± 0.30	1.00 ± 0.18	8	423
	80	0.00 ± 0.85	1.00 ± 0.28	8	564
$e+\mu$	60	0.00 ± 0.09	1.00 ± 0.10	20	269
	70	0.00 ± 0.18	1.00 ± 0.11	20	223
	80	0.00 ± 0.51	1.00 ± 0.17	20	308

Table 7.8: Fit parameters and unsmeared upper limits obtained by testing the PAPAGENO W+dijet samples instead of CDF data.

would derive a lower top mass limit of 71 GeV/c^2 in the muon channel, 75 GeV/c^2 in the electron channel, and 77 GeV/c^2 in both channels combined. The actual limit obtained from the CDF electron+dijet sample comes remarkably close to the limits expected from this ideal situation. On the other hand, our inability to extract a 95% C.L. limit from CDF muon+dijet events is more likely due to a higher background contamination than to larger systematic uncertainties. This can be inferred by comparing the unsmeared σ_{max} values in tables 7.7 and 7.8: the discrepancy is much larger in the muon case than in the electron case.

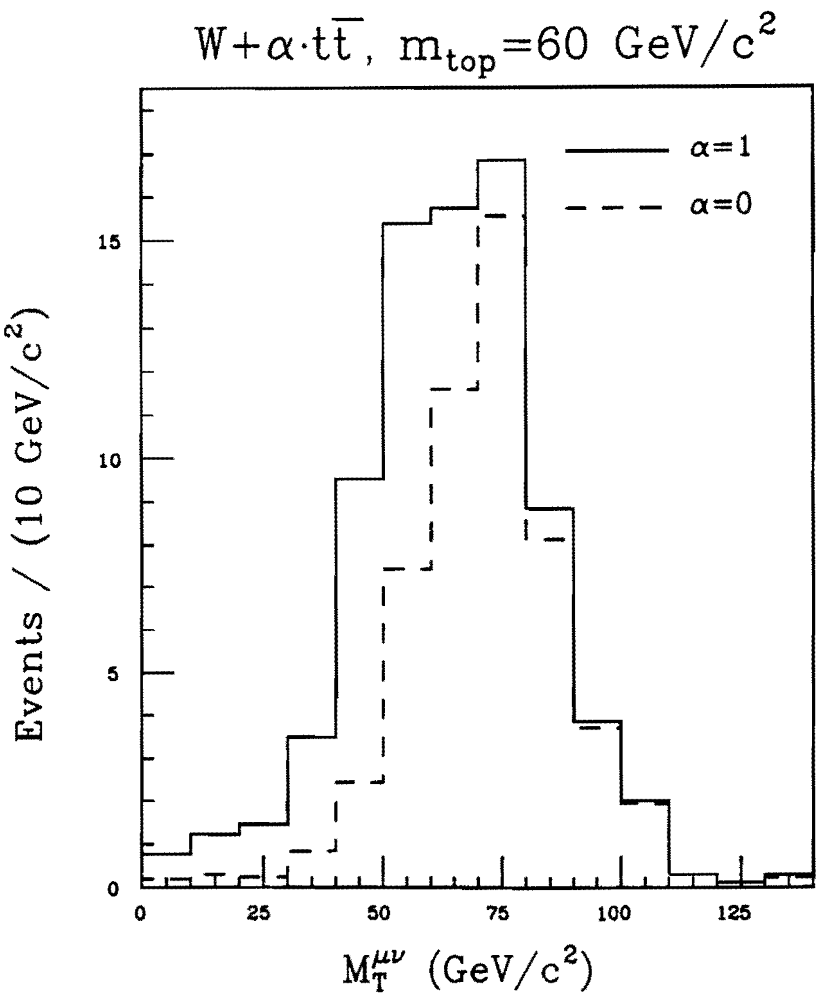

Figure 7.1: Monte Carlo spectrum of the muon–neutrino transverse mass for W+dijet events with ($\alpha = 1$) and without ($\alpha = 0$) a 60 GeV/c^2 top contribution, after full detector simulation. The normalization of the Monte Carlo samples is described in chapter 5.

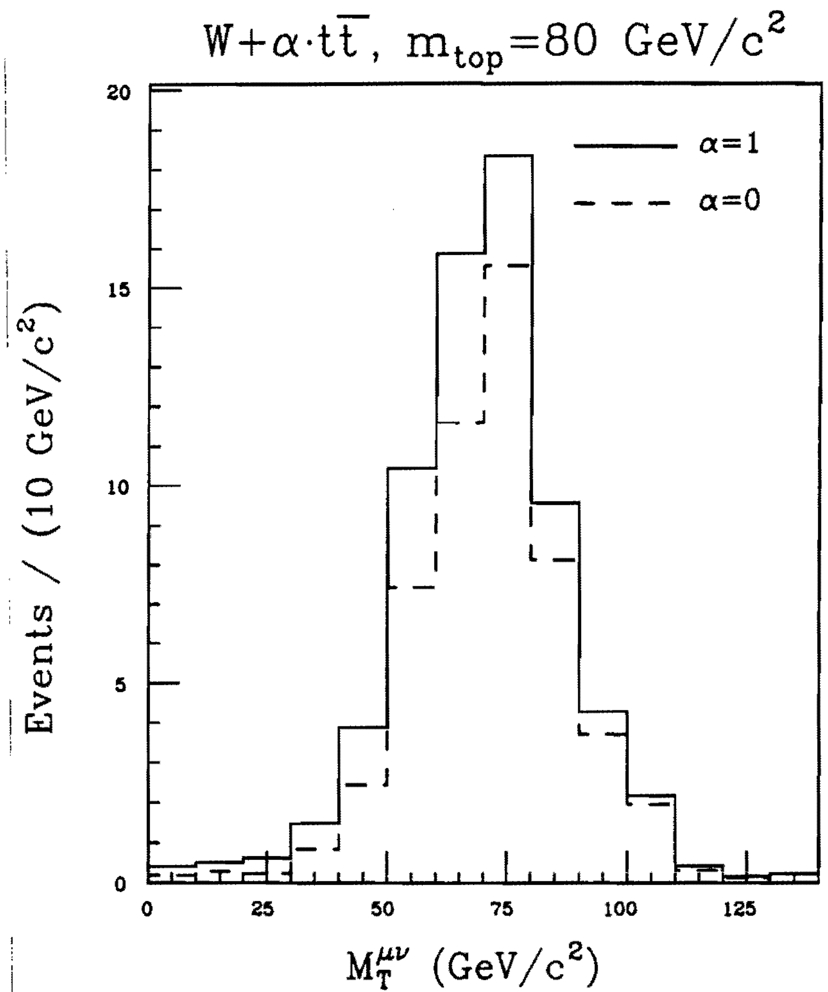

Figure 7.2: Monte Carlo spectrum of the muon–neutrino transverse mass for W+dijet events with ($\alpha = 1$) and without ($\alpha = 0$) a 80 GeV/c^2 top contribution, after full detector simulation. The normalization of the Monte Carlo samples is described in chapter 5.

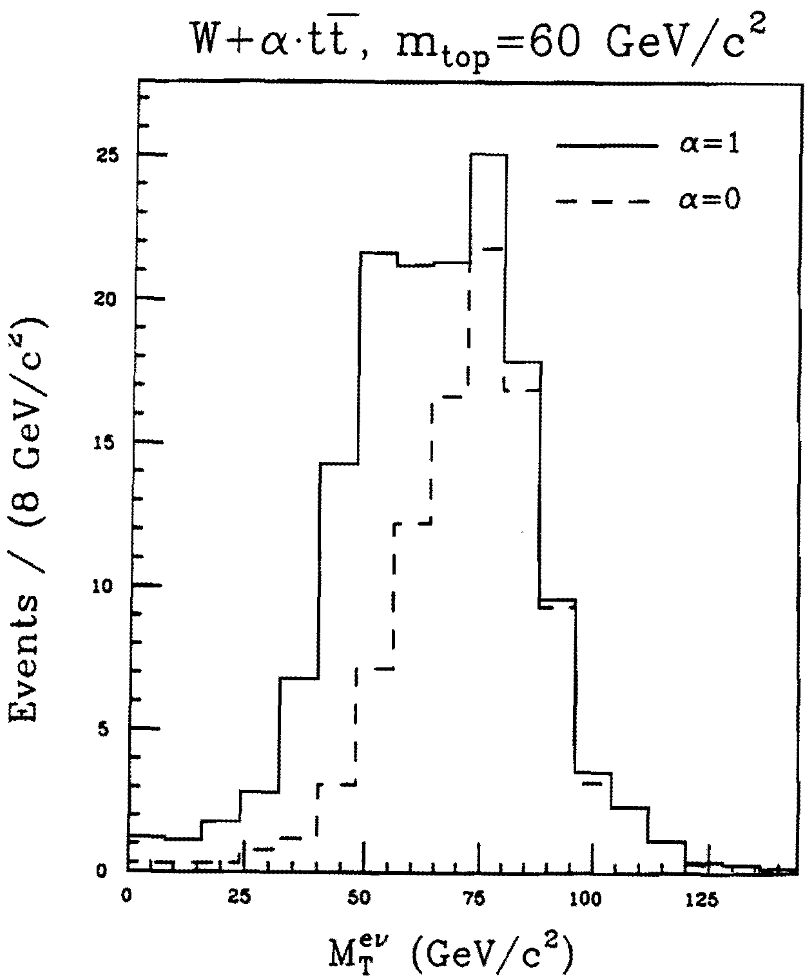

Figure 7.3: Monte Carlo spectrum of the electron-neutrino transverse mass for W+dijet events with ($\alpha = 1$) and without ($\alpha = 0$) a 60 GeV/c^2 top contribution, after full detector simulation. The normalization of the Monte Carlo samples is described in chapter 5.

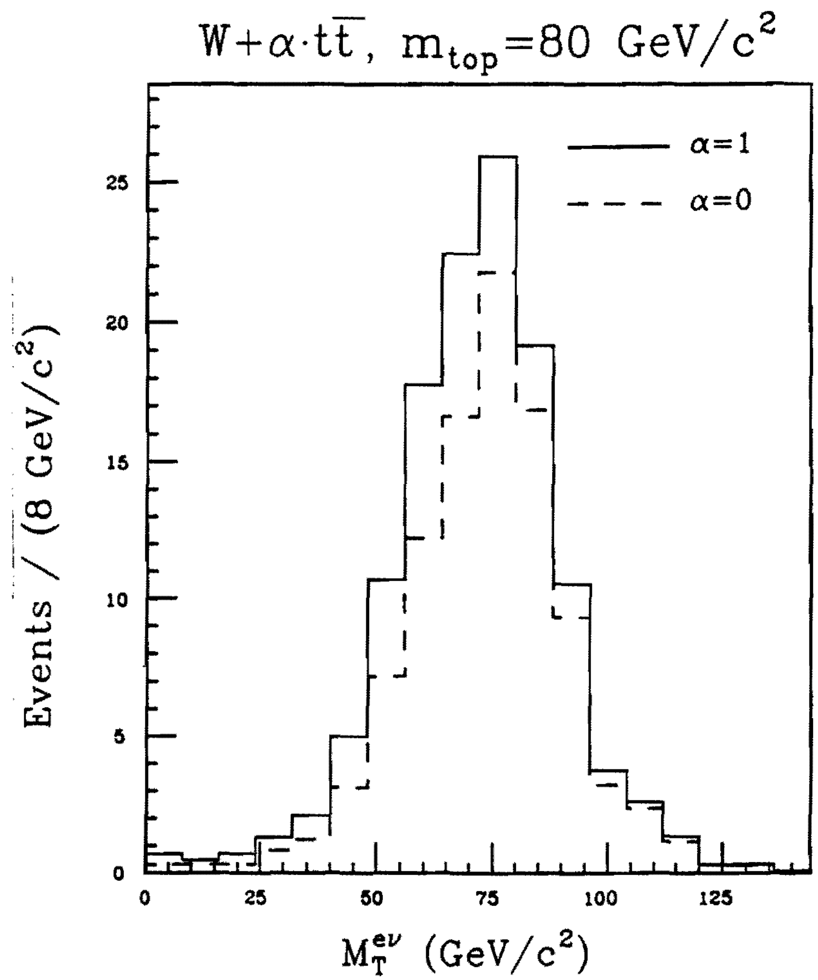

Figure 7.4: Monte Carlo spectrum of the electron-neutrino transverse mass for W+dijet events with ($\alpha = 1$) and without ($\alpha = 0$) a 80 GeV/c^2 top contribution, after full detector simulation. The normalization of the Monte Carlo samples is described in chapter 5.

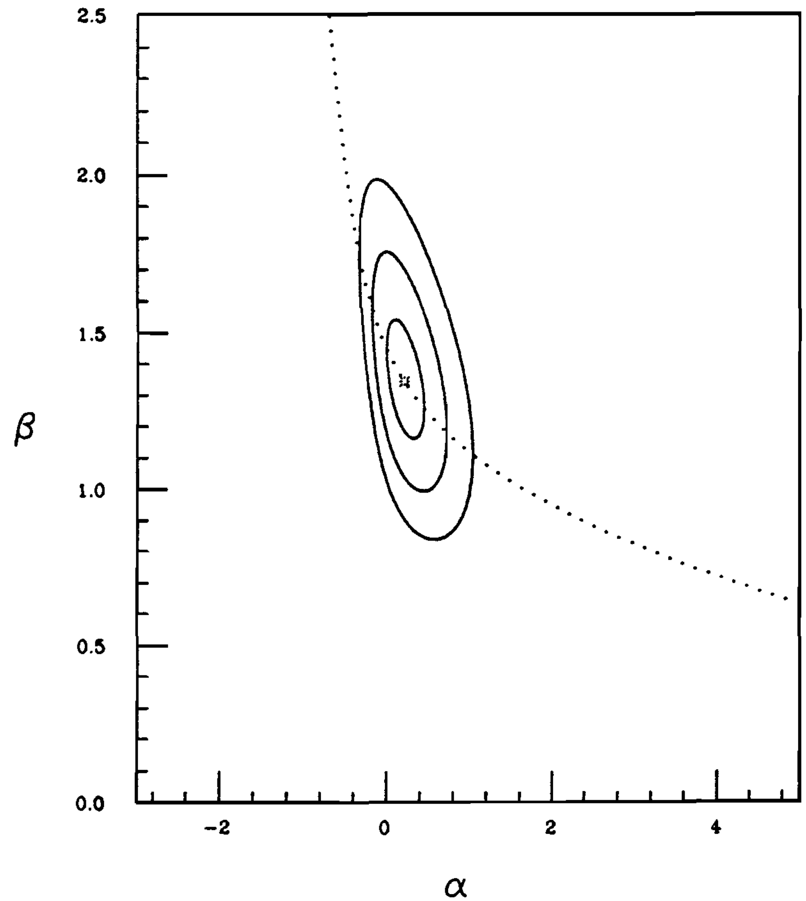

Figure 7.5: Log-likelihood contours in $\alpha - \beta$ space, for the fit to a 60 GeV/c^2 top in the muon channel. The contours correspond to drops of 0.5, 2.0 and 4.5 with respect to the maximum of the log-likelihood function. The dots mark the path along which the likelihood is maximal in each slice α = constant.

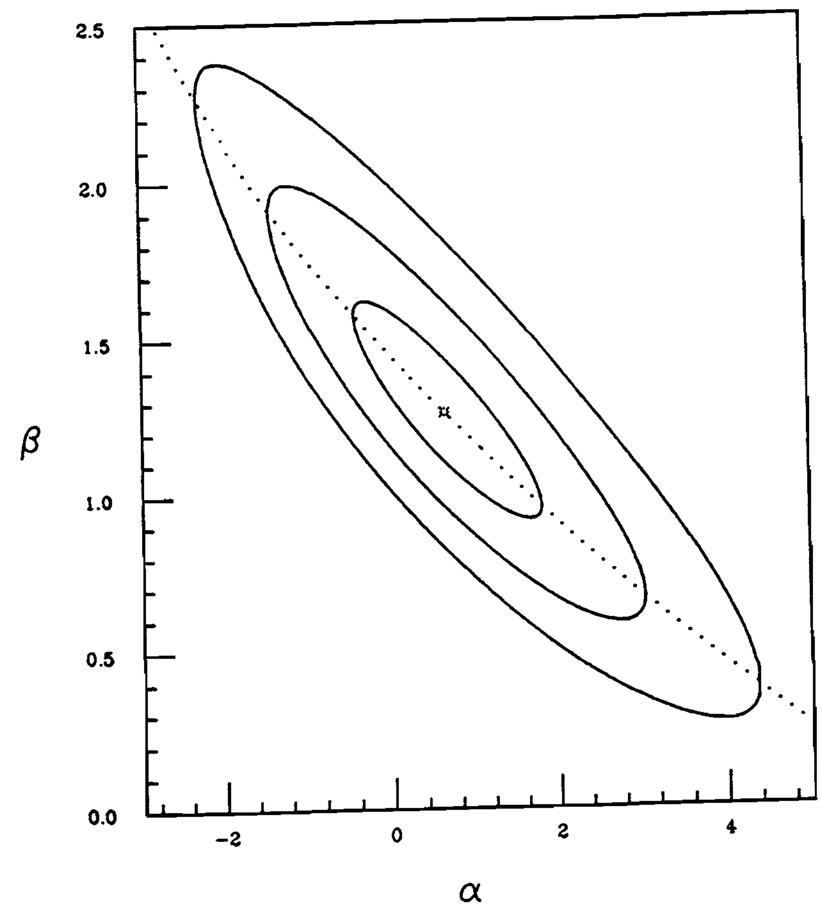

Figure 7.6: Log-likelihood contours in $\alpha - \beta$ space, for the fit to an 80 GeV/c^2 top in the muon channel. The contours correspond to drops of 0.5, 2.0 and 4.5 with respect to the maximum of the log-likelihood function. The dots mark the path along which the likelihood is maximal in each slice α = constant.

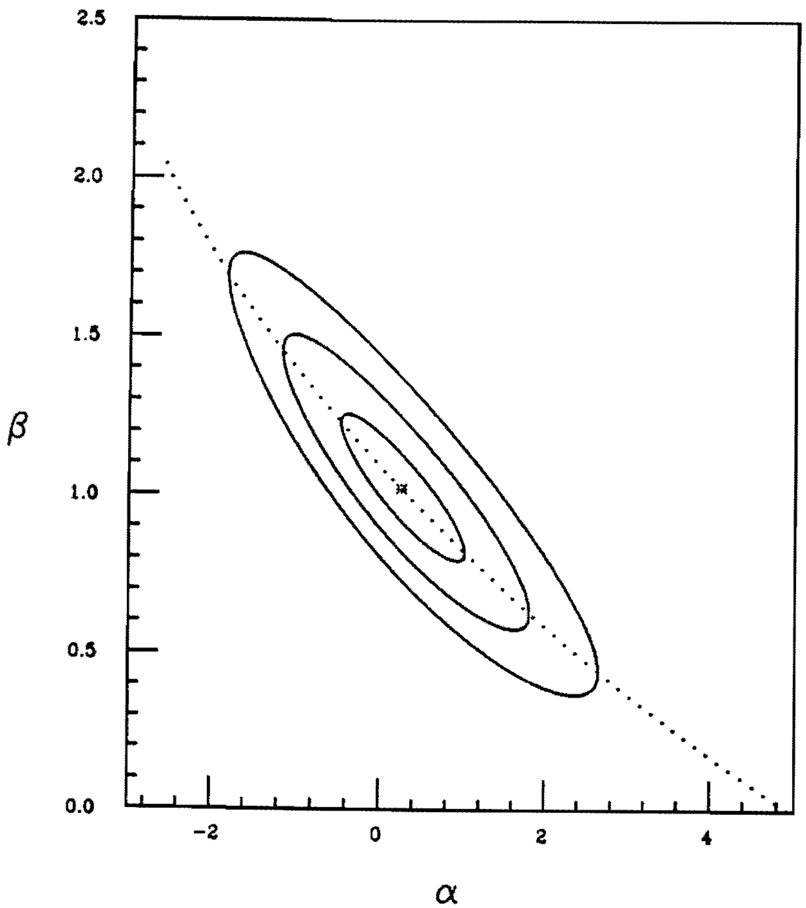

Figure 7.7: Log-likelihood contours in $\alpha - \beta$ space, for the fit to an 80 GeV/c^2 top in the electron channel. The contours correspond to drops of 0.5, 2.0 and 4.5 with respect to the maximum of the log-likelihood function. The dots mark the path along which the likelihood is maximal in each slice α = constant.

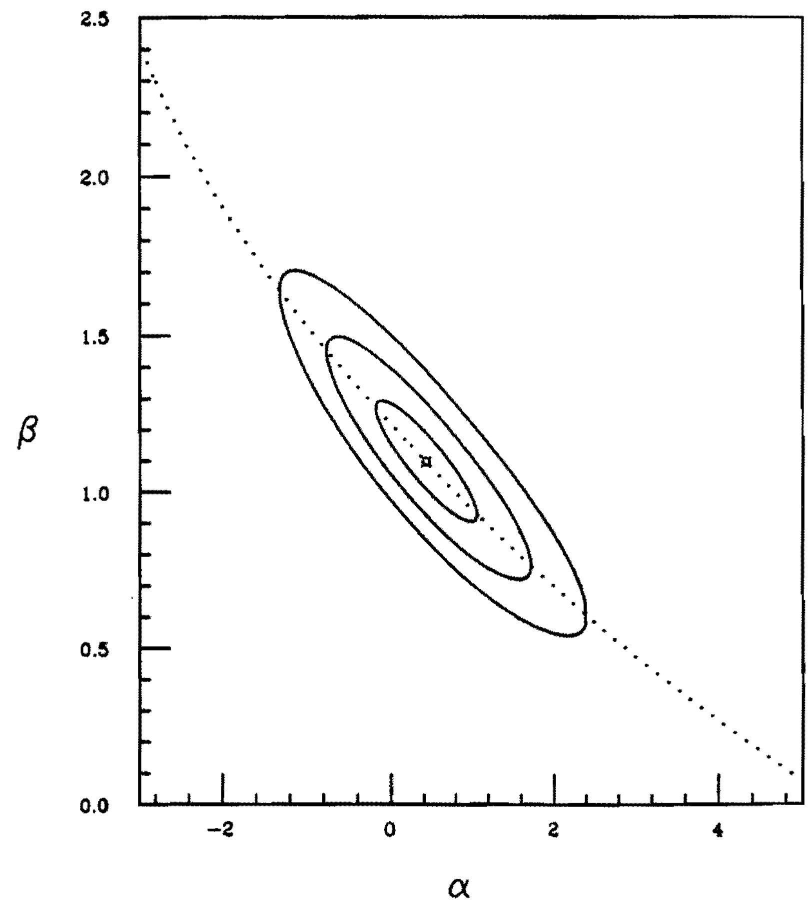

Figure 7.8: Log-likelihood contours in $\alpha - \beta$ space, for the combined electron and muon channel fit to an 80 GeV/c^2 top. The contours correspond to drops of 0.5, 2.0 and 4.5 with respect to the maximum of the log-likelihood function. The dots mark the path along which the likelihood is maximal in each slice α = constant.

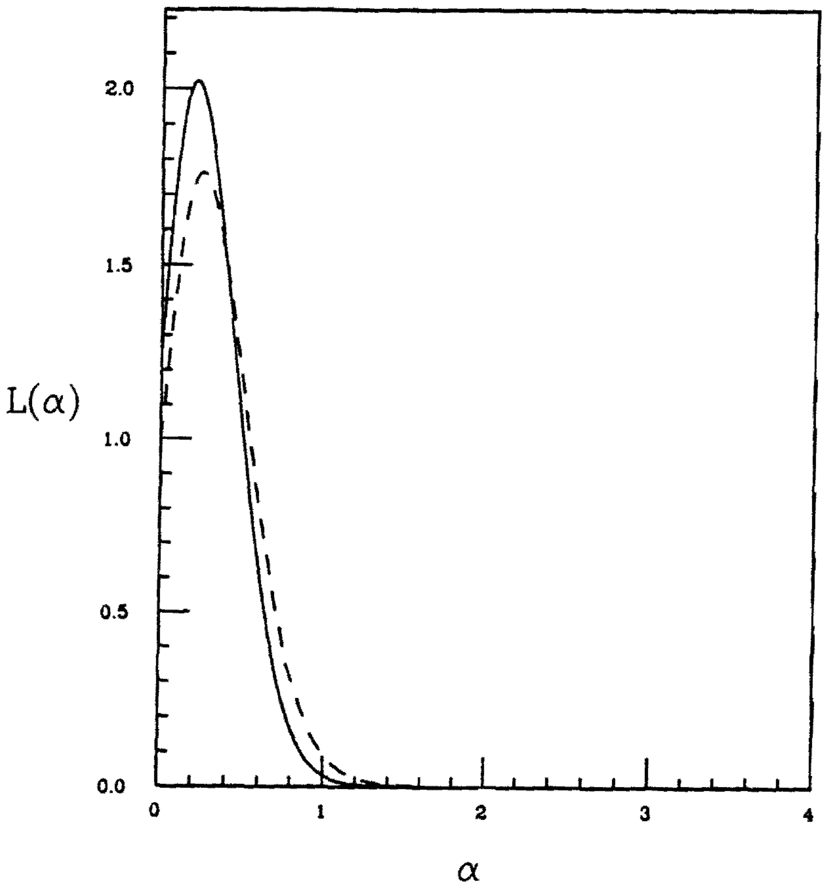

Figure 7.9: Likelihood function before (solid line) and after (dashed line) smearing, for a 60 GeV/c^2 top quark, in the muon + dijet sample.

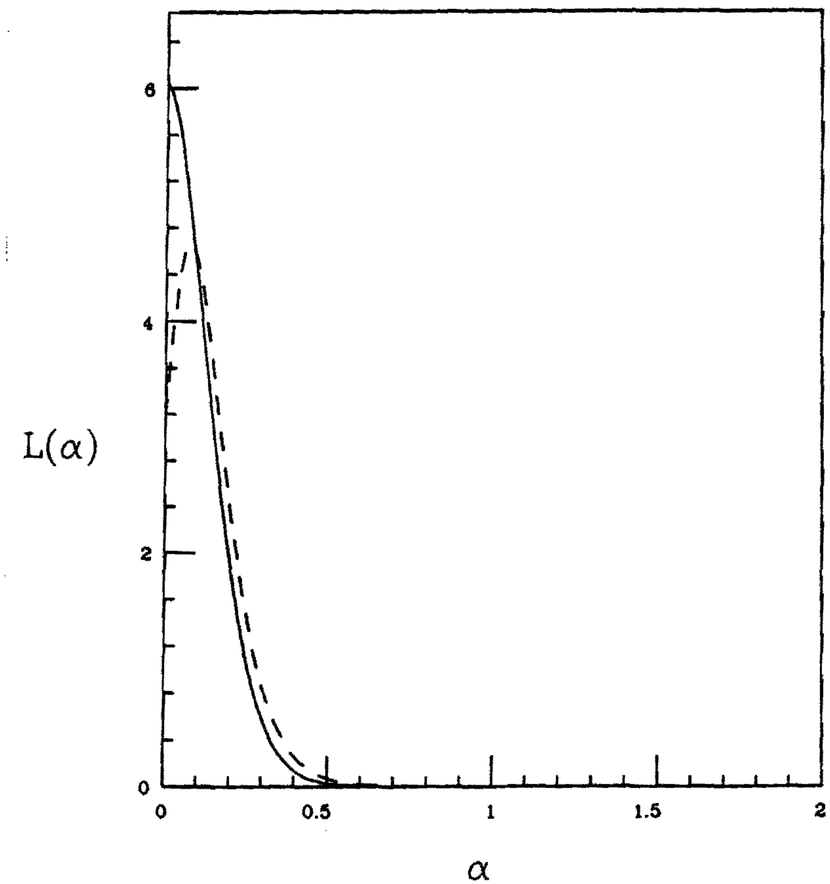

Figure 7.10: Likelihood function before (solid line) and after (dashed line) smearing, for a 60 GeV/c^2 top quark, in the electron + dijet sample.

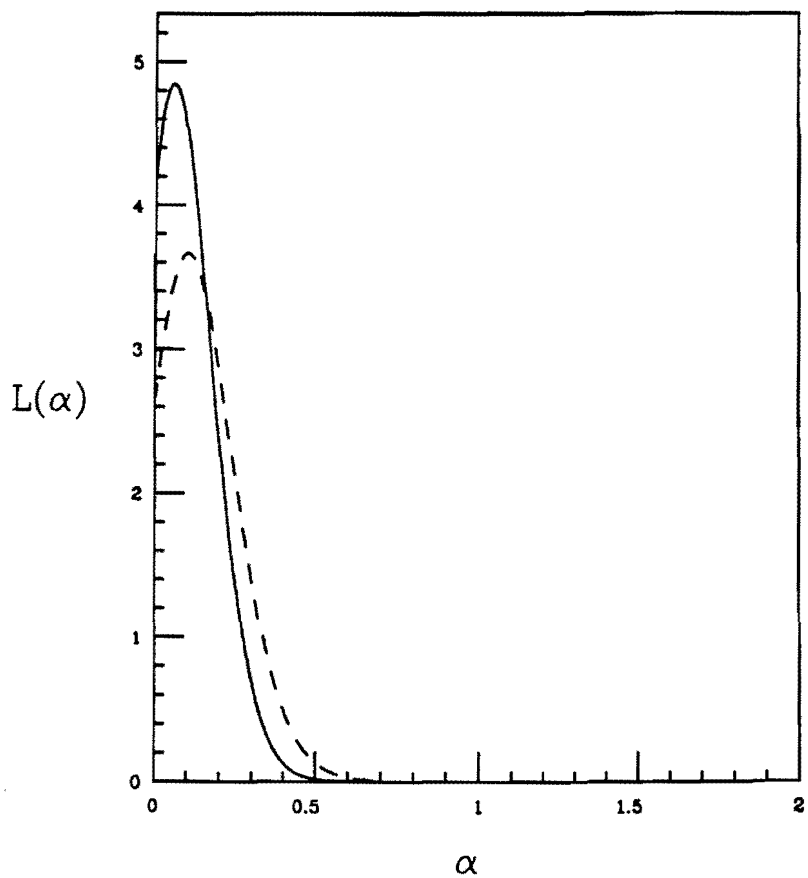

Figure 7.11: Likelihood function before (solid line) and after (dashed line) smearing, for a 60 GeV/c² top quark, in the combined muon and electron + dijet sample.

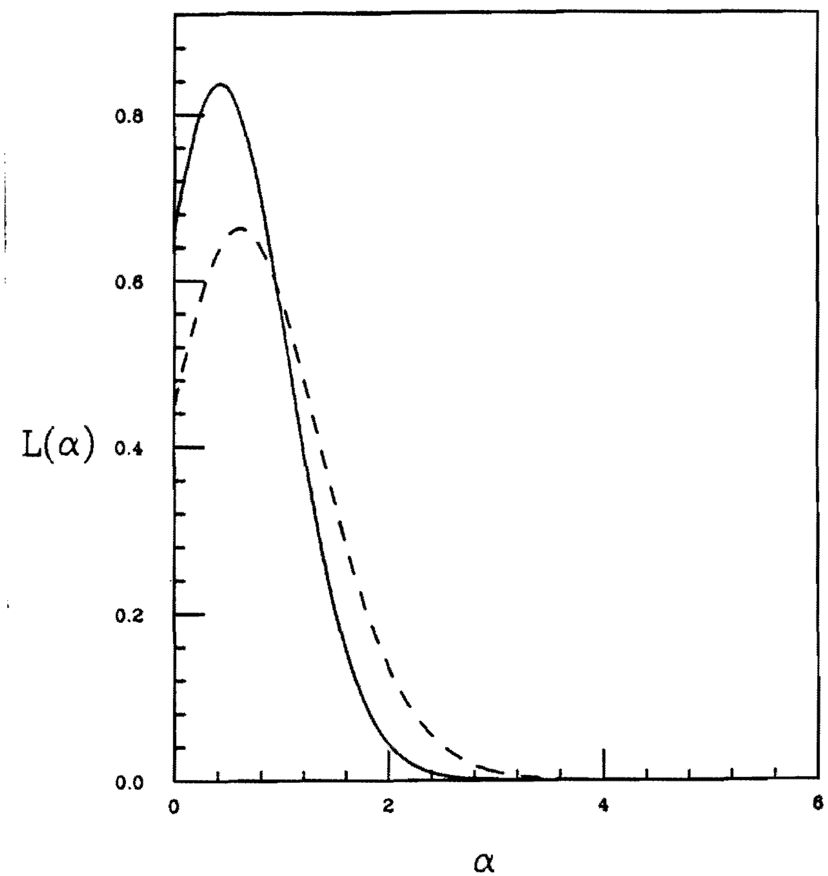

Figure 7.12: Likelihood function before (solid line) and after (dashed line) smearing, for a 80 GeV/c² top quark, in the combined muon and electron + dijet sample.

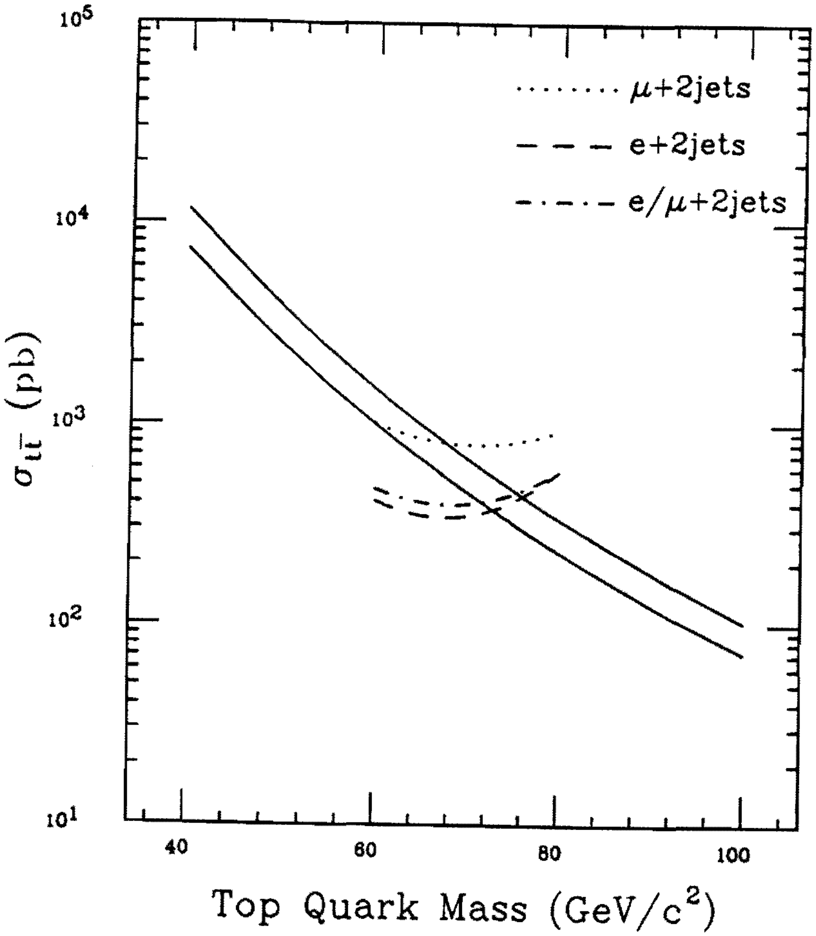

Figure 7.13: The 95% C.L. upper limit on the $t\bar{t}$ production cross section as a function of top mass is given by the dotted, dashed, and dot-dashed lines for the muon, electron, and combined samples respectively. The two solid lines show the lower and upper limits on the theoretical calculation.

Chapter 8

Conclusion

We have looked for evidence of the processes

$$
\begin{aligned}
p\bar{p} &\rightarrow t\bar{t} \rightarrow e\nu_e bq\bar{q}\bar{b} \\
p\bar{p} &\rightarrow t\bar{t} \rightarrow \mu\nu_\mu bq\bar{q}\bar{b}
\end{aligned}
$$

in the set of events collected by CDF during the 1988–1989 Tevatron collider run. Events were selected by requiring an isolated high transverse momentum muon or electron, significant missing transverse energy, and two or more jets. The resulting electron and muon samples have an integrated luminosity of 4.05 and 3.54 pb^{-1} respectively.

Distributions of several quantities describing the lepton–neutrino and dijet systems in each event were shown to be consistent with a Monte Carlo calculation for the production of a W accompanied by two jets.

Backgrounds from QCD multijet and $b\bar{b}$ production were studied with two methods, both of which are based on the expected isolation properties of leptons from top and W decay. The most conservative method estimates background fractions of $(10 \pm 3)\%$ in the final electron sample, and $(20 \pm 6)\%$ in the final muon sample.

The separation between $t\bar{t}$ and W contributions to the final event samples was based on an analysis of the lepton–neutrino transverse mass spectrum. The distribution obtained from the data was fit to a linear superposition of Monte Carlo distributions for the W+dijet and $t\bar{t}$ processes. The fit consisted in maximizing a binned likelihood function, and was separately performed for top masses of 60, 70 and 80 GeV/c^2, in the electron sample, the muon sample, and both samples combined. Fit results are consistent with the absence of top in the samples, for each of the tested top masses.

A top likelihood function was subsequently defined, smeared with systematic uncertainties, and used to extract upper limits on the fraction of the $t\bar{t}$ production cross section which is needed to fit the data. These upper limits were then compared with the lower limit on a theoretical calculation to derive a lower limit on the mass of the top quark. From the electron sample alone, one is able to exclude a top mass between 60 and 73 GeV/c^2, at the 95% confidence level. Because of higher background level, the muon sample does not allow to exclude any 95% C.L. top mass range between 60 and 80 GeV/c^2. These results are all based on the assumption that the top is produced and decays according to the Standard Model description, including in particular a top semileptonic branching ratio of 1/9.

References

[Abe88] F. Abe *et al.* (CDF collaboration), "The CDF detector: an overview", Nucl. Instr. and Meth. **A271**, 387 (1988)

[Abe89] F. Abe *et al.* (CDF collaboration), "Measurement of the mass and width of the Z^0 boson at the Fermilab Tevatron", Phys. Rev. Lett. **63**, 720 (1989)

[Abe90a] F. Abe *et al.* (CDF collaboration), "Search for new heavy quarks in electron-muon events at the Fermilab Tevatron collider", Phys. Rev. Lett. **64**, 147 (1990)

[Abe90b] F. Abe *et al.* (CDF collaboration), presented by K. Sliwa, "A new limit on the mass of the top quark", in *Proceedings of the Twenty-Fifth Rencontres de Moriond, March 1990*, edited by J. Tran Thanh Van (Editions Frontières, Gif-sur-Yvette, 1990).

[Abe91a] F. Abe *et al.* (CDF collaboration), "Top-quark search in the electron+jets channel in proton-antiproton collisions at $\sqrt{s}$ = 1.8 TeV", Phys. Rev. **D43**, 664 (1991)

[Abe91b] F. Abe *et al.* (CDF collaboration), "Measurement of the W-boson mass in 1.8-TeV $\bar{p}p$ collisions", Phys. Rev. **D43**, 2070 (1991)

[Abe91c] F. Abe *et al.* (CDF collaboration), "Measurement of $\sigma B(W \to e\nu)$ and $\sigma B(Z^0 \to e^+e^-)$ in $\bar{p}p$ collisions at $\sqrt{s} = 1800$ GeV", Phys. Rev. **D44**, 29 (1991)

[Abr72] V.A. Abramovskii, O.V. Kancheli and V.N. Gribov, "Structure of inclusive spectra and fluctuations in inelastic processes caused by multiple-pomeron exchange", in *Proceedings of the XVI International Conference on High Energy Physics, National Accelerator Laboratory, Batavia, Illinois, September 1972*, Edited by J.D. Jackson, A. Roberts, and R. Donaldson, (National Accelerator Laboratory, 1973), Vol.1, p.389

[Abr90] P. Abreu *et al.* (DELPHI collaboration), "Search for the t and b' quarks in hadronic decays of the Z^0 boson", Phys. Lett. **B242**, 536 (1990)

[Ada89] I. Adachi *et al.* (TOPAZ collaboration), "A search for a fourth-generation charge $-\frac{1}{3}$ (b') quark using inclusive muons in e^+e^- annihilations at $\sqrt{S}$ = 56.5–60.8 GeV", Phys. Lett. **B229**, 427 (1989)

[Ake90] T. Åkesson *et al.* (UA2 collaboration), "Search for top quark production at the CERN $p\bar{p}$ collider", Z. Phys. **C46**, 179 (1990)

[Akr90] M.Z. Akrawy *et al.* (OPAL collaboration), "A search for the top and b' quarks in hadronic Z^0 decays", Phys. Lett. **B236**, 364 (1990)

[Alb87] H. Albrecht *et al.* (ARGUS collaboration), "Observation of $B^0 - \overline{B}^0$ mixing", Phys. Lett. **B192**, 245 (1987)

[Ami88] D. Amidei *et al.*, "A two level Fastbus based trigger system for CDF", Nucl. Instr. and Meth. **A269**, 51 (1988)

[Apo91] G. Apollinari *et al.*, "A measurement of the $\bar{p}p$ total cross section at $\sqrt{s}$ = 1800 GeV", CDF internal note 1438 (1991)

[Asc88a] G. Ascoli *et al.*, "CDF central muon detector", Nucl. Instr. and Meth. **A268**, 33 (1988)

[Asc88b] G. Ascoli *et al.*, "CDF central muon level-1 trigger electronics", Nucl. Instr. and Meth. **A269**, 63 (1988)

[Bal88] L. Balka *et al.*, "The CDF central electromagnetic calorimeter", Nucl. Instr. and Meth. **A267**, 272 (1988)

[Bae89] H. Baer, V. Barger and R.J.N. Phillips, "Top quark detection via W+njet measurements", Phys. Lett. **B221**, 398 (1989)

[Bar88] E. Barsotti *et al.*, "Fastbus data acquisition for CDF", Nucl. Instr. and Meth. **A269**, 82 (1988)

[Bea87] A. Bean *et al.* (CLEO collaboration), "Improved upper limit on flavor-changing neutral-current decays of the b quark", Phys. Rev. **D35**, 3533 (1987)

[Bed88] F. Bedeschi *et al.*, "Design and construction of the CDF central tracking chamber", Nucl. Instr. and Meth. **A268**, 50 (1988)

[Bel84] S. Belforte and K. Goulianos, "A complete minimum bias event generator", CDF internal note 256 (1984).

[Ber87] D. Bernard *et al.* (UA4 collaboration), "The real part of the proton-antiproton elastic scattering amplitude at the centre of mass energy of 546 GeV", Phys. Lett. **B198**, 583 (1987)

[Ber88] S. Bertolucci *et al.*, "The CDF central and endwall hadron calorimeter", Nucl. Instr. and Meth. **A267**, 301 (1988)

[Boz84] M. Bozzo *et al.* (UA4 collaboration), "Measurement of the proton-antiproton total and elastic cross sections at the CERN SPS collider", Phys. Lett. **B147**, 392 (1984)

[Bra88] G. Brandenburg *et al.*, "An electromagnetic calorimeter for the small angle regions of the collider detector at Fermilab", Nucl. Instr. and Meth. **A267**, 257 (1988)

[Byo90] A. Byon-Wagner *et al.*, "Cosmic filtering of central muon events", CDF internal note 1260 (1990).

[Cih88] S. Cihangir *et al.*, "The CDF forward/backward hadron calorimeter", Nucl. Instr. and Meth. **A267**, 249 (1988)

[Col86] J.C. Collins, D.E. Soper, G. Sterman, "Heavy particle production in high-energy hadron collisions", Nucl. Phys. **B263**, 37 (1986)

[Dec90] D. Decamp *et al.* (ALEPH collaboration), "A search for new quarks and leptons from Z^0 decay at LEP", Phys. Lett. **B236**, 511 (1990)

[Die88] M. Diemoz, F. Ferroni, E. Longo, G. Martinelli, "Parton densities from deep inelastic scattering to hadronic processes at super collider energies", Z. Phys. **C39**, 21 (1988)

[Dob88] A. Dobado, M.J. Herrero, "Some implications of a top mass close to the W boson mass", Phys. Lett. **B203**, 167 (1988)

[Ell79] R.K. Ellis, H. Georgi, M. Machacek, H.D. Politzer, G.G. Ross, "Perturbation theory and the parton model in QCD", Nucl. Phys. **B152**, 285 (1979)

[Ell88] R.K. Ellis, "Heavy quark production at collider energies", in *Proceedings of the 7th Topical Workshop on Proton-Antiproton Collider Physics, Fermilab, June 1988*, edited by R. Raja, A. Tollestrup, and J. Yoh (World Scientific, 1989), p. 639.

[Ell89] R.K. Ellis, "The theory of heavy flavour production", Fermilab Preprint FERMILAB-Conf-89/168-T (1989)

[Ell91] R.K. Ellis, "Rates for top quark production", Fermilab Preprint FERMILAB-Pub-91/30-T (1991)

[Fos88] G.W. Foster *et al.*, "A fast hardware track-finder for the CDF central tracking chamber", Nucl. Instr. and Meth. **A269**, 93 (1988)

[Fox80] G.C. Fox and S. Wolfram, "A model for parton showers in QCD", Nucl. Phys. **B168**, 285 (1980)

[Fre87] J. Freeman, "CDF detector simulation", in *Proceedings of the Workshop on Detector Simulation for the SSC, Argonne, Illinois, August 1987*, Edited by L. Price (Argonne National Accelerator Laboratory Report No. ANL-HEP-CP-88-51), p. 285.

[Fro79] A.G. Frodesen, O. Skjeggestad, H. Tøfte, "Probability and statistics in particle physics", Columbia University Press, Irvington-on-Hudson, New York, 1979, 501pp.

[Fuk88] Y. Fukui *et al.*, "CDF end plug electromagnetic calorimeter using conductive plastic proportional tubes", Nucl. Instr. and Meth. **A267**, 280 (1988)

[Gan89] J. Gannon *et al.*, "Flying wires at Fermilab", in *Proceedings of the 1989 IEEE Particle Accelerator Conference, March 1989*, Edited by F. Bennet and J. Kopta, p. 68.

[Gau89] A. Gauthier, "Efficiency of the level 1 central muon trigger", CDF internal note 937.

[Gau90a] A. Gauthier *et al.*, "Efficiency of the level 2 central muon trigger", CDF internal note 1106.

[Gau90b] A. Gauthier, "Efficiency of the level 3 central muon trigger", CDF internal note 1145.

[Gil88] F.J. Gilman, R. Kauffman, "Top-quark decays when $m_t \approx M_W + m_b$", Phys. Rev. **D37**, 2676 (1988)

[Gro90] C. Grosso-Pilcher *et al.* (CDF collaboration), "CDF luminosity calibration", Preprint Fermilab-FN-550 (1990).

[Hag89] K. Hagiwara and D. Zeppenfeld, "Amplitudes for multi-parton processes involving a current at e^+e^-, $e^\pm p$, and hadron colliders", Nucl. Phys. **B313**, 560 (1989)

[Har91] R.M. Harris, "Definition of CES χ^2", CDF internal note 1329.

[Hin89a] I. Hinchliffe, PAPAGENO (private communication)

[Hin89b] I. Hinchliffe, "Applications of QCD to hadron-hadron collisions: theoretical" in *Proceedings of the seventeenth SLAC Summer Institute on Particle Physics, July 1989*, Edited by E. Brennan, SLAC-report-361, p. 165

[Jam75] F.E. James and M. Roos, "MINUIT — a system for function minimization and analysis of the parameter errors and correlations", Comp. Phys. Comm. **10**, 343 (1975)

[Kan82] G.L. Kane, M.E. Peskin, "A constraint from B decay on models with no t quark", Nucl. Phys. **B195**, 29 (1982)

[Kan90] G.L. Kane, "Top quark topics", in *Proceedings of the eighteenth SLAC Summer Institute on Particle Physics, July 1990*, Edited by J. Hawthorne, SLAC-report-378, p. 123

[Ken91] D.C. Kennedy and P. Langacker, "Precision electroweak experiments and heavy physics: An update", Phys. Rev. **D44**, 1591 (1991)

[Lan91] P. Langacker and M. Luo, "Implications of precision electroweak experiments for m_t, ρ_0, $\sin^2\theta_W$, and grand unification", Phys. Rev. **D44**, 817 (1991)

[Lep78] G.P. Lepage, "A new algorithm for adaptive multidimensional integration", J. of Comp. Physics **27**, 192 (1978)

[Lep80] G.P. Lepage, "VEGAS — An adaptive multidimensional integration program", Newman Laboratory of Nuclear Studies, Cornell University Report No. CLNS-80/447 (1980)

[Mar89a] R. Marshall, "A determination of $\sin^2\theta_W$ and the lepton and quark electroweak couplings from e^+e^- data", Z. Phys. **C43**, 607 (1989)

[Mar89b] A.D. Martin, R.G. Roberts, W.J. Stirling, "Benchmark cross sections for $p\bar{p}$ collisions at 1.8 TeV", Z. Phys. **C42**, 277 (1989)

[Mar91] A.D. Martin, R.G. Roberts, W.J. Stirling, "Precision analysis of $\Lambda_{\overline{MS}}$ and the gluon distribution and its implications for jet and top-quark cross sections", Phys. Rev. **D43**, 3648 (1991)

[Moo89] C.D. Moore *et al.*, "Single bunch intensity monitoring system using an improved wall current monitor", in *Proceedings of the 1989 IEEE Particle Accelerator Conference, March 1989*, Edited by F. Bennet and J. Kopta, p. 1513

[Nas88] P. Nason, S. Dawson, R.K. Ellis, "The total cross section for the production of heavy quarks in hadronic collisions", Nucl. Phys. **B303**, 607 (1988)

[Nas89] P. Nason, S. Dawson, R.K. Ellis, "The one particle inclusive differential cross section for heavy quark production in hadronic collisions", Nucl. Phys. **B327**, 49 (1989). Erratum, Nucl. Phys. **B335**, 260 (1990)

[Orr90] L.H. Orr, J.L. Rosner, "Comparison of top quark hadronization and decay rates", Phys. Lett. **B246**, 221 (1990)

[Orr91] L.H. Orr, "Decay versus hadronization for top quarks produced in hadron colliders", Phys. Rev. **D44**, 88 (1991)

[Pai86] F.E. Paige and S.D. Protopopescu, "ISAJET 5.20: A Monte Carlo event generator for pp and $\bar{p}p$ interactions", Brookhaven National Laboratory Report No. BNL-38034, 1986 (unpublished)

[Pet83] C. Peterson, D. Schlatter, I. Schmitt, P.M. Zerwas, "Scaling Violations in Inclusive e^+e^- Annihilation Spectra", Phys. Rev. **D27**, 105 (1983)

[Pro89a] J. Proudfoot, "Electron identification in the CDF central calorimeter", in *Proceedings of the workshop on calorimetry for the Superconducting Supercollider, University of Alabama, Tuscaloosa, Alabama, March 1989*, edited by R. Donaldson and M.G.D. Gilchriese (World Scientific, 1990), p. 1

Ros88] J.L. Rosner, "Heavy flavor theory", in *Proceedings of the 1988 Banff Summer Institute*, edited by A. Kamal and F. Khanna (World Scientific, 1989), p. 395

Ros89] J.L. Rosner, "Aspects of top-quark searches in TeV hadron collisions", Phys. Rev. **D39**, 3297 (1989) Erratum, Phys. Rev. **D40**, 1701 (1989)

Roy90] D.P. Roy, S.U. Sankar, "Upper limit on $B_d^0 - \overline{B}_d^0$ mixing as evidence for the existence of the top quark", Phys. Lett. **B243**, 296 (1990)

[Sjo85] T. Sjöstrand, "A model for initial state parton showers", Phys. Lett. **B157**, 321 (1985)

[Smi89] D.A. Smith, "Study of muons associated with jets in proton-antiproton collisions at $\sqrt{s}$ = 1.8 TeV", Ph.D. thesis, University of Illinois at Urbana-Champaign (1989)

[Sni88] F. Snider *et al.*, "The CDF vertex time projection chamber system", Nucl. Instr. and Meth. **A268**, 75 (1988)

[Vel89] M. Veltman, "The importance of radiative corrections", in *Proceedings of a NATO Advanced Research Workshop on Radiative Corrections: Results and Perspectives, July 1989*, edited by N. Dombey and F. Boudjema (Plenum Press, New York, 1990), p. 1

[Wes89] T.K. Westhusing, "Observation of $W \rightarrow \mu\nu$ decays in proton-antiproton collisions at $\sqrt{s}$ = 1.8 TeV", Ph.D. thesis, University of Illinois at Urbana-Champaign (1989)